Title
Tomographic Laser Absorption Imaging of Combustion Gases in the Mid-wave Infrared

Author
Wei, Chuyu

Publication Date
2020

Peer reviewed|Thesis/dissertation

UNIVERSITY OF CALIFORNIA

Los Angeles

Tomographic Laser Absorption Imaging of Combustion Gases in the Mid-wave Infrared

A dissertation submitted in partial satisfaction

of the requirements for the degree

Doctor of Philosophy in Mechanical Engineering

by

Chuyu Wei

2020

ABSTRACT OF THE DISSERTATION

Tomographic Laser Absorption Imaging of Combustion Gases in the Mid-wave Infrared

by

Chuyu Wei
Doctor of Philosophy in Mechanical Engineering
University of California, Los Angeles, 2020
Professor Raymond M. Spearrin, Chair

This dissertation describes advancements in mid-infrared laser absorption tomography for spatio-temporal measurements of thermochemistry in reacting flows relevant to combustion systems. Tunable laser absorption spectroscopy is combined with tomographic reconstruction techniques to resolve small diameter ($<$ 1 cm) non-uniform flow fields with steep spatial gradients, leveraging emerging mid-wave infrared photonics. Multiple novel measurement methods, hardware configurations, and image processing techniques were investigated. Initially, a mid-infrared laser absorption tomography sensing method was developed for quantitative measurement of CO and CO_2 concentrations and temperature distributions in turbulent premixed jet flames using a translation-stage-mounted optical system. This sensing approach was used to examine effects of varying fuel structure on carbon oxidation over a range of Reynolds number regimes. It was found that spatial and temporal resolution is limited in this method due to the finite laser beam size ($\sim$ 1 mm) and the slow mechanical translation of the optical system. To address these limitations, a novel laser absorption imaging (LAI) technique, that expands a single laser beam and replaces the detector with a high-speed infrared camera, was introduced to achieve enhanced spatial and temporal resolution for thermo-chemical imaging. As a demonstration of this new technique, distributions of combustion species were imaged in both axisymmetric and non-axisymmetric flow fields using linear tomography algorithms. For non-axisymetric flows, the limited view tomography

problem often results in a blurring effect and artifacts in the reconstructed flow-field. In an effort to address these issues, state-of-the-art deep learning neural networks were developed and applied to solve the limited angle inversion. Initial results suggest that deep neural networks have potential to more accurately predict flame structures with fewer projection angles than linear tomography. This work provides a foundation for a new approach to quantitative time-resolved 3D thermo-chemical imaging in high-temperature reacting flows.

The dissertation of Chuyu Wei is approved.

Ann Karagozian

Jeff D. Eldredge

Richard Wirz

Raymond M. Spearrin, Committee Chair

University of California, Los Angeles

2020

Table of Contents

List of Figures

List of Tables

List of Symbols

δ_f Lamianr flame thickness

ΔE Energy of the photon associated with a molecular transition

ν Frequency of the photon

ρ Density

τ_η Kolomogorov time scale

τ_f Flame time

φ_ν Lineshape function

Da Damköhler number

e Specific total energy

E_{lower} Lower state energy

E_{upper} Upper state energy

$f(r)$ Field variable in Abel transform

$f(x, y)$ Field variable in 2D tomography

h Plank Constant

H_{fl} Flame height

I_0 Incident light intensity

I_t Transmitted light intensity

k_ν Spectral absorption coefficient at ν

K_j Integrated spectral absorption coefficient for rovibrational transition j

Ka Karlovitz number

L Absorbing path length

L_{int} Flame integral length scale

P Total pressure

$p(\theta, t)$ Projection variable in 2D tomography at an inclination angle $\theta and axis$t

$P(x)$ Projection variable in Abel transform

$R_T(T^{rec})$ Regularization term for temperature in non-linear absorption tomography

$R_X(X^{rec})$ Regularization term for concentration in non-linear absorption tomography

Re Reynolds number

$S_j(T)$ Line-strength for rovibrational transition j

S_L Lamianr flame speed

T_{ad} Adiabatic flame temperature

X_{abs} Mole fraction of absorbing species

α_ν Absorbance at ν

γ_T Regularization parameter for temperature in non-linear absorption tomography

γ_X Regularization parameter for concentration in non-linear absorption tomography

λ Regularization parameter for Tikhonov regularization

$\overrightarrow{\mathrm{f}}$ Field data vector

$\overrightarrow{\mathrm{P}}$ Projection data vector

ϕ Equivalence ratio

$\pi(\cdot)$ Probability density function

$\pi(\mathbf{f} \mid \mathbf{P})$ Posterior pdf

$\pi(\mathbf{P} \mid \mathbf{f})$ Likelihood pdf

$\pi(\mathbf{P})$ Evidence pdf

$\pi_{pr}(\mathbf{f})$ Prior pdf

$\mathbf{A}_{ATP}$ Abel three point projection matrix

$\mathbf{A}_{OP}$ Onion peeling projection matrix

$\mathbf{D}_{ATP}$ Abel three point deconvolution matrix

$\mathbf{j}_k$ Diffusion flux of species k

$\mathbf{L}_0$ 1D discrete gradient operator

$\mathbf{L}$ 2D discrete gradient operator

$\mathbf{q}$ Heat flux

$\mathbf{u}$ Velocity vector

$\mathbf{W}$ Projection/Weight matrix in 2D tomography

$\mathbf{Y}_k$ Mass fraction of species k

Acknowledgments

First and foremost, I would like to express my sincere gratitude to my PhD adviser Prof. R. Mitchell Spearrin for his mentorship over the years. Prof. Spearrin has provided not just invaluable guidance for my research, but also ample opportunities for me to learn and grow personally. I have always been inspired by your passion for excellence and deep understanding for applied research. In so many ways, you have been an ideal adviser and it has been an honor and a pleasure to study under your mentorship. I hope I can influence junior members in like fashion as I transition into my next career steps.

I would also like to thank my committee members at UCLA: Prof. Ann Karagozian, Prof. Jeff D. Eldredge, and Prof. Richard Wirz for their feedback and support over the years and for helping me build up academic foundations for my research through the fluid mechanics and combustion coursework.

I thank Prof. Achuta Kadambi from Electrical and Computer Engineering Department at UCLA for introducing me to the field of computer vision and computational imaging and for coaching me through my ECE coursework. The skill sets I built from the coursework have been tremendously helpful in my research and I look forward to continuing to extend my work in the future.

Special gratitude to Prof. Daniel I. Pineda for stimulating a collaborative lab environment during his postdoctoral appointment at UCLA; for daily discussions and help in solving the numerous research challenges; and for suffering with me during countless late night experiments and paper deadlines. You have taught me a great deal and I wish you great success with your career at UTSA.

I am grateful to have the best labmates and fortunate to have been surrounded by so many intelligent and helping peers. I have fond memories of the day-to-day help with each other in research and coursework, our daily coffee and lunch break, and our happy-hour discussions. Living and studying in a different country is never easy but you make me feel welcome and appreciated. Know that I will treasure the fun times and excitement we've had

over the years, and look forward to many more in coming years.

Most of all, I am forever grateful to my family, for unconditionally supporting my decision to study on the other side of the planet and pursue a PhD. My mother, Jinghui Li, taught me how to be a good person, the value of persistence and encouraged me to pursue my passion. I love you from the bottom of my heart and thank you for everything.

Curriculum Vitae

2011 – 2015	B.S. in Energy Engineering, Zhejiang Unversity, Hangzhou, China.
2015 – 2016	M.S. in Mechanical Engineering, UCLA, Los Angeles, United States.
2017 – Present	Ph.D. student in Mechanical Engineering, UCLA, Los Angeles, United States.

Publications

[1] **C. Wei**, K.K. Schwarm, D.I. Pineda, R.M. Spearrin, 3D laser absorption imaging of temperature, CO, and CO2 in laminar flames using masked Tikhonov regularization. (In progress) 05/2020)

[2] D.I. Pineda, L. Paxton, N. Perakis, **C. Wei**, S. Luna, H. Kahouli, M. Ihme, F.N. Egolfopoulos, R.M. Spearrin, "Carbon oxidation in turbulent premixed jet flames: a comparative experimental and numerical study of ethylene, n-heptane, and toluene," *Combustion and Flame*. (In revision, 05/2020)

[3] **C. Wei**, K. K. Schwarm, D. I. Pineda, and R. M. Spearrin, "Deep neural network inversionfor 3D laser absorption imaging of methane in reacting flows," *Optics Letters*, vol. 45,no. 8, pp. 2447–2450, 2020.

[4] F. A. Bendana, D. D. Lee, **C. Wei**, D.I. Pineda, R. M. Spearrin, "Line mixing and broadening in the v (1→ 3) first overtone bandhead of carbon monoxide at high temperatures and high pressures," *Journal of Quantitative Spectroscopy and Radiative Transfer*, 239 (2019): 106636.

[5] K. K. Schwarm, **C. Wei**, D. I. Pineda, and R. M. Spearrin, "Time-resolved laser absorption imaging of ethane at 2 kHz in unsteady partially premixed flames," *Applied Optics*, 58(21):5656, 7 2019.

[6] **C. Wei**, D. I. Pineda, C. S. Goldenstein, and R. M. Spearrin, "Tomographic laserabsorption imaging of combustion species and temperature in the mid-wave infrared," *Optics Express*, vol. 26, p. 20944, 8 2018.

[7] **C. Wei**, D. I. Pineda, L. Paxton, F. N. Egolfopoulos, and R. M. Spearrin, "Mid-infraredlaser absorption tomography for quantitative 2D thermochemistry measurements inpremixed jet flames," *Applied Physics B*, vol. 124, p. 123, 6 2018.

[8] **C. Wei**, K.K. Schwarm, D.I. Pineda, R.M. Spearrin. 3D laser absorption imaging of combustion gases assisted by deep learning. Accepted, in OSA Optical Sensors and Sensing Congress, Vancouver, British Columbia, Jun 22–26, 2020.

[9] **C. Wei**, D.I. Pineda, R.M. Spearrin. Mid-infrared laser absorption tomography for quantitative temperature, CO, and CO2 in turbulent flames. OSA Imaging and Applied Optics Congress, Orlando, FL, Jun 25–28, 2018.

CHAPTER 1

Introduction

Laser absorption spectroscopy (LAS) provides a highly quantitative, calibration-free method of measuring gas concentration and temperature using compact low-power semiconductor lasers [1]. However, due to its line-of-sight (LOS) integration nature, LAS has mostly been applied in relatively uniform laboratory environments such as shock tubes and gas cells or to make path-averaged measurements on energy conversion devices [2]. To overcome this limitation, laser absorption tomography (LAT) has been developed to reconstruct spatially resolved species and temperature fields from LOS absorption measurements along various projections using tomographic reconstruction techniques [3]. The aim of this work is to advance the spatial-temporal capability of LAT by harnessing the latest mid-wave infrared photonics, introducing uniquely compact optical arrangements, and developing novel and robust data processing methods to enable new applications. Details about the motivations and challenges for high-speed spatially-resolved gas diagnostics are discussed below, followed by a review and comparison of various available imaging techniques. The introduction closes with an overlook of the dissertation.

1.1 Background

1.1.1 Motivation for Imaging Combustion Flows

Combustion remains the primary source of energy production in usage today and is essential to modern society. Our transportation system relies almost completely on combustion, and over 60% of the electricity of the world is generated via this energy conversion process [4, 5].

Moreover, combustion is widely used in heating, industrial processes and propulsion. This dominance is believed to continue in the future for many decades and therefore combustion remains a research field of vital importance. In order to improve energy conversion efficiency and reduce the formation of pollutants, understanding and effective control of the combustion process is essential. Most practical combustion devices involve turbulent reacting flows. Understanding interactions between flow dynamics, chemical kinetics, and heat and mass transfer in turbulent flames is of prime interest to the combustion community, both for the development of more efficient engineering devices and the development and refinement of numerical models [6]. Understanding the strong non-linear coupling of different mechanisms with overlapping timescales remains a significant scientific challenge to date. Key to understanding turbulent combustion relies on the ability to experimentally measure thermochemical flow parameters such as temperature, mixture composition, pressure, and velocity at high temporal and spatial resolution with high quantitative precision. These measurements not only provide insights into the underlying chemical and physical phenomena, but also serve as validation targets for increasing higher fidelity simulations of turbulent flames with more detailed chemistry.

1.1.2 Challenges for Imaging Combustion Flows

In addition to difficulties for scientific understanding and modeling, the convoluted nature of combustion flows also places challenges for optical imaging techniques. First and foremost, characteristic timescales of chemical reactions is in the orders of magnitudes from millisecond to microsecond [5]. Chemical kinetics are often coupled with other mechanisms such as mass transport and radiation due to overlapping timescales [7, 8]. High-speed imaging techniques are desired to untangle the intricate interactions between different mechanisms. Secondly, flames are characterized by very thin ($\sim$ 1 mm) reaction zones and steep gradients of flow properties. In order to resolve these gradients, high spatial resolution is required for imaging techniques. In addition, emission from high-temperature gases and environment can saturate the detectors and interfere with the measured signal if not handled properly.

Emission scales with increasing temperature and—for gaseous molecules—also with increasing pressure, both of which are characteristic of combustion reactions [1]. Moreover, soot formation in the combustion process results in emission from black body radiation, similar to molecular emission. Additionally, soot can cause particle scattering and window fouling. Finally, practical combustion devices often have limited optical access [3]. Ideally, imaging techniques should be deployable with limited optical access, sparse view angles and minimum modification to the combustion devices.

In summary, an ideal imaging technique for combustion flows should provide high-speed, spatially-resolved, and quantitative gas property measurements in harsh environments with minimum requirements for optical access. There are many measurement methods aimed at addressing this ideal (or a portion thereof), with various strengths and weaknesses.

1.2 Thermo-chemical Imaging Techniques

Traditional intrusive measurement techniques such as thermocouples and gas chromatography (using sampling probes) disturb the local flow field, often precluding definitive interpretation of flow-field properties. As such, several non-intrusive optical measurement techniques have been utilized to image flow-fields by exploiting emission, scattering, refraction, and absorption interactions. In this section, different optical imaging techniques will be briefly reviewed, with emphasis on their advantages and disadvantages, as well as some applications in combustion diagnostics.

1.2.1 Chemiluminescence

Chemiluminescence is electromagnetic radiation emitted by molecules when they radiatively relax to a lower energy state from an excited energy state produced via chemical reactions. Combustion diagnostics based on chemiluminescence are attractive for their simplicity and non-intrusive nature (usually only requiring a camera and spectral filter). Common targeted species are CH^*, OH^*, C_2^* and CO_2^* with chemiluminescence in the visible and ultraviolet [9].

Chemiluminescence can provide information about conditions in the reaction zone, and has been applied to measure equivalence ratio (ϕ) [10, 11], flame front locations [12], and spatial heat release rate [10]. However, quantitative interpretation of chemiluminescence signals has been based historically on heuristic arguments or empirical data and modeling with limited conditions [9]. Additionally, optical calibration must be performed on a basis that is specific to each experimental setup, posing challenges for measurements free of facility dependence.

Chemiluminescence measurements are inherently line-of-sight measurements, and tomography must be performed to obtain 3-D measurements for highly non-uniform reacting flows. As such, Computed Tomography of Chemiluminescence (CTC) has been developed to provide instantaneous 3-D information on flame geometry and excited species abundance. The technique reconstructs the 3-D chemiluminescence intensity field using Computed Tomography (CT) from multiple line-of-sight measurements of projected chemiluminescence images [13] and has been used to measure 3D chemiluminescence intensity field for both laminar and turbulent flames [14–18]. Most recently, deep-learning based algorithms with high computational efficiency have also been used for reconstructing chemiluminescene fields, showing promise for rapid data processing and real-time flame monitoring [19].

1.2.2 Laser-induced fluorescence

Laser induced fluorescence (LIF) is spontaneous emission from atoms or molecules that have been excited by laser radiation. Laser-induced fluorescence (LIF) is a two-step process: absorption of the laser photon, followed by spontaneous emission. There are two typical experimental arrangements of LIF: namely, planar laser-induced fluorescence (PLIF), and volumetric laser-induced fluorescence (VLIF). In a PLIF setup, the beam from the laser is passed through a system of lenses and/or mirrors to form a laser sheet, which is then used to excite molecules in a plane inside a flow-field [20, 21] as shown in Figure 1.1. Fluorescence from this plane is then recorded by a camera facing perpendicular to the laser sheet. In a VLIF setup, volumetric measurements can either be achieved by sweeping the laser sheet mechanically and recording fluorescence from successively excited planes [22], or by shaping

the laser beam into a volume, record the volumetric emission with multiple cameras from different view angles, and then combined with tomography algorithms to reconstruct 3D field [23].

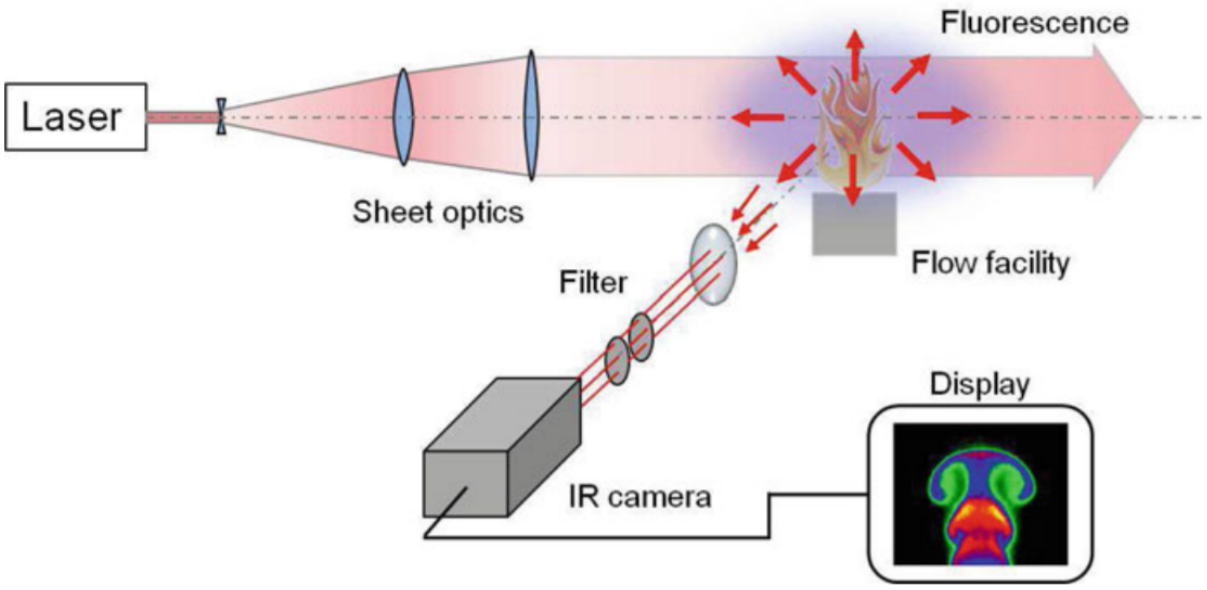

Figure 1.1: Schematic of a PLIF experiment to measure species concentration [1]

Laser-induced fluorescence can be used to measure different species including radicals or atoms (OH,C_2,CN,O,H), stable diatoms (O_2, NO, CO, I_2), and polyatomics (CO_2, CH_2O, Acetone) [1]. Laser-induced fluorescence is attractive for combustion diagnostics, providing an imaging tool with high spatial resolution to measure species-specific abundance, temperature, and various spatial scalars in flames to reveal fluid dynamics. It can also be used to approximate heat release zones (similar to chemiluminescence), usually by targeting the hydroxyl radical and formaldehyde. However, PLIF and VLIF involve greater optical complexity (than chemiluminescence) due to coupled setup and alignment of both the laser sheet/volume and cameras. LIF signals depend on optical collection efficiency, and thus require calibration for specific setups, which complicates quantitative species interpretation. Moreover, tracer molecules can potentially influence combustion and LIF signals are weak at elevated pressures due to collisional de-excitation (quenching). Despite these drawbacks, LIF

is used extensively for examining spatial scalars in flames due to its high spatial resolution.

1.2.3 Rayleigh Scattering

Rayleigh scattering refers to the elastic scattering of electromagnetic radiation which occurs when the electric fields of the radiation interact with the electric fields of gas molecules, resulting scattered light with no shift in wavelength [24]. While for a molecule to absorb light, the light must generally be at specific wavelength, Rayleigh scattering can occur at almost any wavelength.

Rayleigh scattering offers a relatively simple method to measure molecular number density and temperature of in point or planar manner with necessary optical calibration as show in Figure. However, these techniques do not provide species selectivity and reflect aggregate results from gas molecules with different scattering cross-sections. In contrast to other species-specific imaging techniques (Raman scattering and absorption-based tomography), Rayleigh scattering readily provides temperature in the whole flow field. Therefore, Rayleigh scattering has mostly been used for thermometry [25–27], and can be quantitative with an estimation of gas composition [28–30].

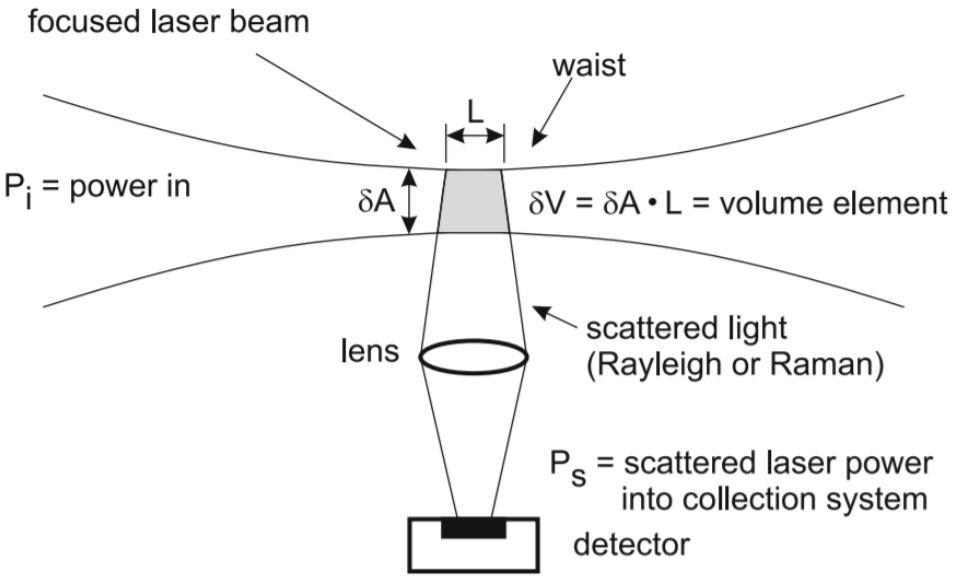

Figure 1.2: Schematic of a light scattering experiment [1].

1.2.4 Raman Scattering

While Rayleigh scattering techniques exploit the elastic scattering process, Raman scattering exploits inelastic scattering with a transfer of energy between the molecule and scattered photon. During the scattering process, if the molecule gains energy from the photon and is excited to a higher vibrational energy state, then the scattered photon loses energy and its wavelength increases, which is called Stokes Raman scattering. Alternatively, if the molecule loses energy by relaxing to a lower vibrational level, the scattered photon gains energy, resulting in a decrease in its wavelength, which is called Anti-Stokes Raman scattering. Raman scattering provides access to species without intrinsic dipole moments. Commonly targeted species include O_2, N_2, H_2 and CO_2. However, the cross-section for Raman scattering is often 3 orders of magnitude smaller than Rayleigh scattering [1], and thus requires very high power light sources.

Scattering techniques have been combined with PLIF to perform Raman-Rayleigh-LIF measurements to charaterize flames [25, 31]. Raman-Rayleigh measurement yields absolute data at a reference point, which anchors the scale of PLIF images. The combined results provide simultaneous quantitative 2D measurements of temperature and species in turbulent flames. However, the multi-technique setup can be quite complicated, expensive, and requires considerable optical access.

1.2.5 Laser Absorption Tomography

Laser absorption spectroscopy (LAS) exploits resonance with discrete energy modes of gas molecules to ascertain thermochemical properties of flow fields from light absorption. Laser absorption tomography (LAT) is an imaging technique that involves reconstructing 2D or 3D distributions of gas properties from multiple line-of-sight laser absorption measurements. By probing ro-vibrational transitions in the infrared, LAT provides access to many species present in combustion reactions ranging from hydrocarbon fuels (CH_4, C_2H_6), intermediates (CO, CH_2O) to combustion products (CO_2, H_2O), though with the exception of molecules

without intrinsic dipole moments. Exploiting laser absorption, LAT offers a highly quantitative, species-specific and calibration free optical imaging tool for combustion diagnosis, especially with recent advances in mid-infrared laser absorption diagnostics [2] (to be discussed in Chapter 3). Infrared LAS also benefits from the ability to utilize compact, low-power light sources due to the strong absorption interaction (relative to other spectroscopies).

Path-integrated laser absorption spectroscopy measurements can be modeled using Fredholm integral equation of the first kind. This is in the same mathematical form as X-ray measurements in medical imaging, and therefore established computed tomography (CT) can be applied to reconstruct spectral absorption and infer thermodynamic properties such as species concentration and temperature. A typical LAT experimental setup often involves translating a single LOS or flame mechanically [32, 33] or multiple lasers and detectors to cover the region of interest [34, 35]. As a result, the temporal and spatial resolution is often limited with LAT. This is the primary weakness of LAT relative to other laser imaging methods, and motivates the research described in this dissertation. As a summary, different imaging techniques discussed above are compared in Table 1.1.

1.3 Overview of the dissertation

This dissertation presents developments and applications of laser absorption imaging systems over the course of seven chapters. Following the introduction, Chapter 2 reviews the theory and applications of laser absorption tomography and Chapter 3 reviews recent advancements in mid-infrared laser absorption diagnostics. The dissertation continues with experimental developments of multi-dimensional laser absorption systems combined with different tomographic reconstruction techniques. Chapter 4 demonstrates a mid-infrared LAT strategy for quantitative 2D measurement of CO and CO_2 concentrations and temperature distributions in turbulent premixed jet flames. Chapter 5 then reports the application of the mid-infrared LAT techniques to study the fuel effects on carbon oxidation in these turbulent premixed jet flames. Chapter 6 then proposes a novel laser absorption imaging (LAI) technique that expands a single laser beam and replaces the detector with a high-speed infrared camera

to achieve enhanced spatial and temporal resolution. The first half of chapter 6 presents the application of LAI on axisymmertric flows using a single projection angle. Tomographic imaging of non-axisymmetric flows is more challenging—multiple projection angles are required toestimate the flow-field scalars, and the inversion problem is underdetermined and ill-posed. The second half of Chapter 6 reports a rotation-stage-based multi-angle LAI system for quantitative 3D measurement of CO and CO_2 concentrations and temperature distributions in laminar flames. Classical Tikhonov-regularized linear tomography is applied to solve the limited-angle tomography problem. However, limited view angles often result in a blurring effect and artifacts in the reconstructed flow-field, complicating applications to flames—which have very thin ($\sim$1 mm) reaction zones. Chapter 7 discusses the author's current work on implementing deep learning neural network to solve the inverse problem and reduce blurring and artifacts. Finally, the dissertation closes with an outlook for future work.

Table 1.1: Comparison of Thermo-chemical Imaging Techniques

Method	Chemi-luminescence	Laser Induced Fluorescence	Rayleigh Scattering	Raman Scattering	Schlieren Imaging	Laser Absorption Tomography
Interaction Type	Emission	Absorption →Emission	Elastic Scattering	Inelastic Scattering	Refraction	Absorption
Cross-section	N/A	$10^{\neg 24}$ cm^2/molec	$10^{\neg 27}$ cm^2/molec	$10^{\neg 30}$ cm^2/molec	N/A	$10^{\neg 20}$ cm^2/molec
Measured Properties	Species	Species/ temperature/ pressure	Temperature	Species/ temperature/ pressure	Refractive index/ density	Species/ temperature/ pressure
Commonly Targeted Species	OH^*, CH^*, $C_2{}^*$, CN^*, NH^*	OH, CH, CH_2O, NO, C_3H_6O	Indiscriminate	O_2, N_2, H_2	Indiscriminate	CH_4, C_2H_6, CO, CO_2, H_2O
Measurement dimension	Line-of-sight(LOS)/ Tomographic measurement	Planar/ Volumetric measurement	Point/Planar measurement	Point/Line measurement	LOS/ Tomographic measurement	LOS/ Tomographic measurement
Advantages	Easy setup	High spatial resolution	Measurements in entire flow field	Access to species without intrinsic dipole moment	High spatial resolution/ Flow field structure	Highly quantitative/ access to many species
Limitations in temperature and species space	Hard to be quantitative	Hard to be quantitative for native species	No species selectivity	Limited spatial resolution/ complicated setup	No species selectivity/ not quantitative in temperature	No access to species without intrinsic dipole moment/ typically low spatial resolution

CHAPTER 2

Background on Laser Absorption Tomography

2.1 Introduction

Tomography is a science that reconstructs an unknown spatial distribution of a quantity of interest (the inverse problem) from a set of projection measurements (the forward problem). In a laser absorption tomography measurement, we're concerned with the attenuation of light that depends on an unknown distribution of gas absorption coefficients. The forward problem is governed by the well-known Beer-Lambert law through a nonuniform absorbing medium as a function the ratio of incident light, I_0, and the transmitted light, I_t [1] by neglecting thermal emission at the measured frequency ν [cm^{-1}]:

$$\alpha_\nu = -\ln\left(\frac{I_t}{I_0}\right)_\nu = \int_0^L k_\nu dl = \int_0^L S_j(T) P X_{\mathrm{abs}} \varphi_\nu dl \tag{2.1}$$

Spectral absorbance α_ν thus depends on total pressure P [atm], line-strength S_j [cm^{-2}/atm] for rovibrational transition j, mole fraction of absorbing species X_{abs}, lineshape function φ_ν [cm], and aggregate path length L [cm]. One can effectively eliminate the measurement dependence on line shape φ_ν by integrating over the wavenumber domain for each line j [1]:

$$A_{j,proj} = \int_{-\infty}^{\infty} \alpha_\nu d\nu = \int_0^L K_j dl = \int_0^L S_j(T) P X_{\mathrm{abs}} dl \tag{2.2}$$

where $K_j(r)$ [cm^{-2}] is integrated spectral absorption coefficient that directly relates to the thermodynamic properties of the gas flow.

The inverse problem in LAT is aimed to estimate the spatial distribution of the absorbance coefficient k_ν or the integrated spectral absorption coefficient K_j and eventually

determine spatially resolved gas properties such temperature and species mole fraction. However, the inverse problem is an ill-posed problem, meaning that the inversion is either underdetermined, in which case an inifinite number of solutions may exist that match the projection measurements; or unstable against small changes in the measurement data, such that small amount of measurement noise can be amplified and distort the reconstruction results [3]. This chapter gives an overview of the different 1D and 2D tomographic algorithms used in LAT and their applications in combustion diagnostics.

2.2 1D Laser Absorption Tomography

Axially-symmetric disctributions are frequently encountered in combustion applications. In this case, flow variables are only a function of the radius from the center r and the projections along any arbitrary view angle are equivalent; thus given the name 1D tomography. Under this assumption, a projection measurement from a single orientation is adequate to reconstruct the flow field and thus greatly simplifies the experimental setup and required optical access.

2.2.1 Abel Transform: Projection and Deconvolution

The geometry of the axisymmetric flame deconvolution problem is shown in Figure 2.1. The projected absorbance area measurement is described by the well-known Abel integral equation as a line-of-sight integration over the flame with radius R at a given distance from the flame center y:

$$P(x) = 2\int_x^R \frac{f(r)r}{\sqrt{r^2 - x^2}}dr \tag{2.3}$$

where x is the abscissa coordinate of projected data and r is the radial coordinate of the flow field. In the context of a LAT measurement, for example in Equation 2.2, $P(y)$ is the measured projected absorbance area $A_{j,proj}(r)$ and $f(r)$ is the radial distribution of the integrated spectral absorption coefficient $K_j(r)$.

An analytical solution for Equation 2.3 exists, and it is known as it is known as the Abel

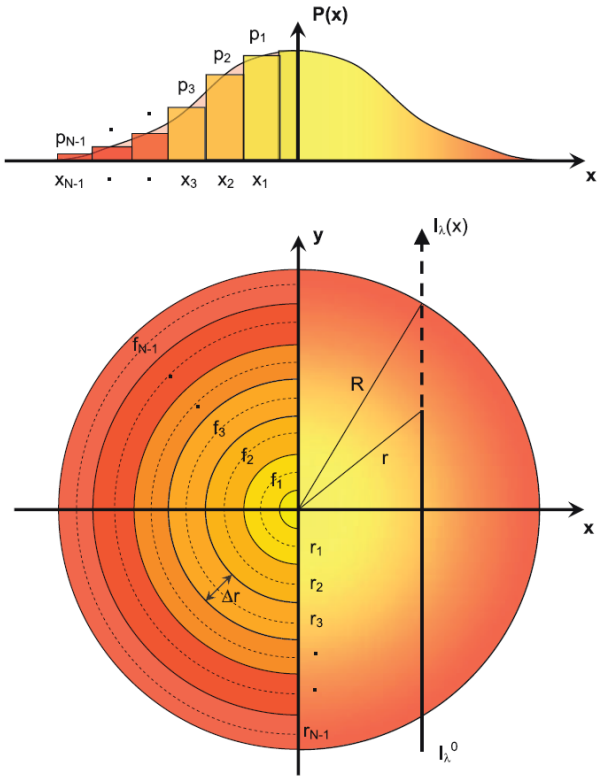

Figure 2.1: Axisymmetric flame deconvolution geometry [36].

inversion:

$$P(x) = -\frac{1}{\pi}\int_x^R \frac{P'(x)}{\sqrt{x^2 - r^2}}dx \tag{2.4}$$

where $P'(x)$ is the derivative of the projected data. However, direct implementation of the analytical form of Abel inversion requires an analytical expression for the derivative of the projected data $P'(x)$, which is usually unknown in practical applications. Instead, a numerical implementation using finite difference approximations with discretized projection values as shown in Figure 2.1 is more commonly used in practical applications.

Modern numerical algorithms for Abel inversions to reconstruct spatial fields $f(r)$ include the onion-peeling (OP) algorithm and the Abel two/three-point transform; these algorithms have been thoroughly reviewed and compared in the work by Dasch [37]. For the OP algorithm, the flow field in divided into N annular elements, with a width of $\Delta r = R/(N - 0.5)$, and $f(r)$ is assumed to be constant over each annular element as shown in Figure 2.1. Car-

rying out the integral equation 2.3 over each annulus results in a matrix equation:

$$\mathbf{A_{OP}}\vec{f} = \vec{P} \tag{2.5}$$

where $\vec{f} = [f_0, f_1, ...f_{N-1}]^T$ and $\vec{P} = [P_0, P_1, ...P_{N-1}]^T$ contain the radial field variables evaluated at the center of the annular elements and discrete projected data, respectively, and $\mathbf{A_{OP}}$ is the onion-peeling projection matrix that contains geometric terms given in [37]. Unlike OP, the Abel three-point (ATP) transform fits the projection $P(x)$ with a quadratic function using 2 neighboring points, and then approximate the derivative of the projected data $P'(x)$ over each annular element. Writing the analytical Abel inversion equation over every annular element results in another matrix equation:

$$\vec{f} = \mathbf{D_{ATP}}\vec{P} \tag{2.6}$$

where $\mathbf{D_{ATP}} = \mathbf{A_{ATP}^{-1}}$ is the discrete representation of the Abel inversion [37]. For 1D flame measurements, the ATP transform is preferred due to its easy implementation, high computational efficiency and robustness against noise among the three methods [3, 37]. Unfortunately, these numerical methods do not address the ill-posed nature of Abel integral equation and in practical applications, noises and perturbations in projection measurements are inevitable, which can be amplified and cause large errors during the inversion process. A common solution is to pretreat the projection measurements and smooth the data before the deconvolution step. However, this limits the spatial resolution and is subject to users' choices of the smoothing window. Alternatively, Tikhonov regularized Abel inversion is proposed in attempt to address the ill-posed nature of Abel integral equation [38] and will be discussed in the next section.

2.2.2 Tikhonov Regularization

Tikhonov regularization is an efficient technique to mitigate the ill-posedness of the matrix equation. In this method, the original matrix equation is augmented with an extra set of equations that promotes smoothness of the solution:

$$\lambda\mathbf{L_0}\vec{f} = 0 \tag{2.7}$$

where λ is the regularization parameter that controls the level of regularization and $\mathbf{L_0}$ is a discrete gradient operator that characterizes the smoothness of the solution:

$$\mathbf{L_0} = \begin{bmatrix} 1 & -1 & 0 & \dots & 0 \\ 0 & 1 & -1 & \dots & 0 \\ & & \dots & \dots & \\ 0 & 0 & \dots & \dots & -1 \\ 0 & 0 & 0 & \dots & 1 \end{bmatrix} \tag{2.8}$$

Combining Eq. 2.6 and Eq. 2.7, the radial distribution $f(r)$ can be found from a least-squares solution:

$$\vec{f_\lambda} = \arg\min \left|\left| \begin{bmatrix} \mathbf{A} \\ \lambda \mathbf{L_0} \end{bmatrix} \vec{f} - \begin{bmatrix} \vec{P} \\ 0 \end{bmatrix} \right|\right| \tag{2.9}$$

where the projection matrix $\mathbf{A}$ can be either $\mathbf{A_{OP}}$ or $\mathbf{A_{ATP}}$. The regularization parameter λ characterizes the relative importance of the accuracy and smoothness of the solution. A proper choice of the regularization parameter λ is essential for good reconstruction results. In this work, we follow the "L-curve" criterion [36] to determine a proper regularization parameter λ in a systematic manner. In this criterion, the norm of the smoothness term $||\lambda \mathbf{L_0} \vec{f}||$ are plotted versus the norm of the residual term $||\mathbf{A}\tilde{\mathbf{f}} - \tilde{\mathbf{P}}||$ for different values of λ and this usually results in a L-shape curve as shown in Figure 2.2. A small λ results in a solution that explains the measurement data (including noises) very well but may be highly oscillatory due to noise amplification (upper left part of the curve). A large λ promotes a smooth solution that may not explain the measurement data very well (lower right part of the curve). Therefore, an ideal value of λ lies on the corner of the L-curve. Tikhonov regularization Abel inversion has been broadly applied in LAT experiments to retrieve flow thermodynamic properties in axisymmetric flows [32, 33, 38**?** –44].

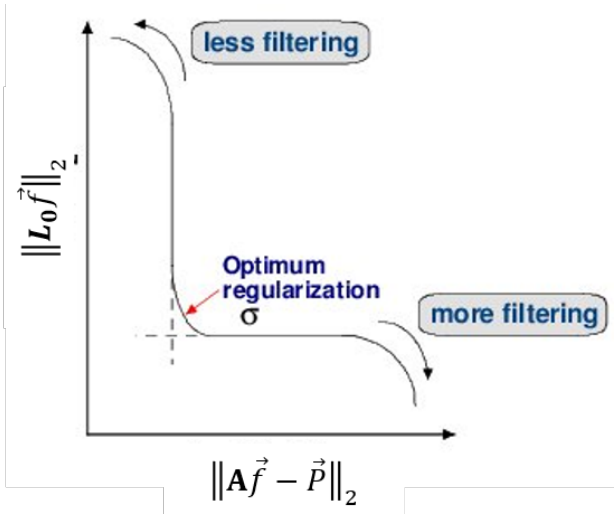

Figure 2.2: Schematic for L-curve method: the corner of the curve corresponds to optimum regularization. Figure adopted from [45].

2.3 2D Laser Absorption Tomography

In most practical applications, however, flow fields cannot be simplified with axially-symmetrical assumptions, and two independent spatial variables are needed to describe the flow fields, hence the term 2D tomography. In 2D tomography, the inversion problem is more challenging, as the number of unknowns increase geometrically and measurements with many view angles are needed to resolve the flow fields. In addition to sensitivity to measurement noises as in 1D tomography, 2D tomography problems in combustion applications often result in an underdetermined system due to limited optical access. Different tomographic reconstruction techniques in LAT have been reviewed in great detail in the review by Cai et al. [3] and are briefly explained below.

2.3.1 Analytical Technique: Filtered Back Projection

The forward problem in 2D tomography of a field variable $f(x, y)$ is described by the Radon transform, defined as:

$$p(\theta, t) = \int_l f(x, y) dl \tag{2.10}$$

where l is the integration path, $p(\theta, t)$ is the line-of-sight measurement at an inclination angle of θ with respect to the x-axis and t is the axis of the projection data with the center aligned with the origin of $f(x, y)$ as shown in Figure 2.3. The Filtered Back Projection (FBP) is a classical tomographic reconstruction method based on the analytical solution to the Radon transform and is broadly used in medical imaging for X-ray computed tomography [46]. The FBP can be derived from the Fourier slice theorem, which states that the 1D Fourier transform of a projection $p(\theta, t)$ is equal to the 2D Fourier transform of $f(x, y)$, $F(u, v)$, evaluated at angle θ as shown in Figure 2.3. To perform the inversion, then, we can acquire projections at many different angles over $(0, \pi)$ to fill in the $F(u, v)$ space and then do an inverse 2D Fourier transform to reconstruct the field $f(x, y)$. Cai et al. provided one single equation that capture the entire operation [3]:

$$f(x, y) = \underbrace{\underbrace{\int_0^{\pi} \int_{-\infty}^{\infty} \underbrace{\int_{-\infty}^{\infty} p(\theta, t) e^{-2\pi i \cdot \omega t} dt}_{\text{Fourier transform of a projection}} |\omega| e^{2\pi i \cdot \omega t} d\omega \, d\theta}_{\text{Inverse Fourier transform}}}_{\text{Backprojection}} \tag{2.11}$$

where $|\omega|$ is a ramp filter used to deblur the reconstructed image. The FBP algorithm is non-iterative and very computationally efficient. However, it only works well when a large number of projection measurements are available to adequately sample the sinogram space and therefore has been mostly applied in the environments with adequate optical access where projections can be measured at arbitrary view angles [47–51].

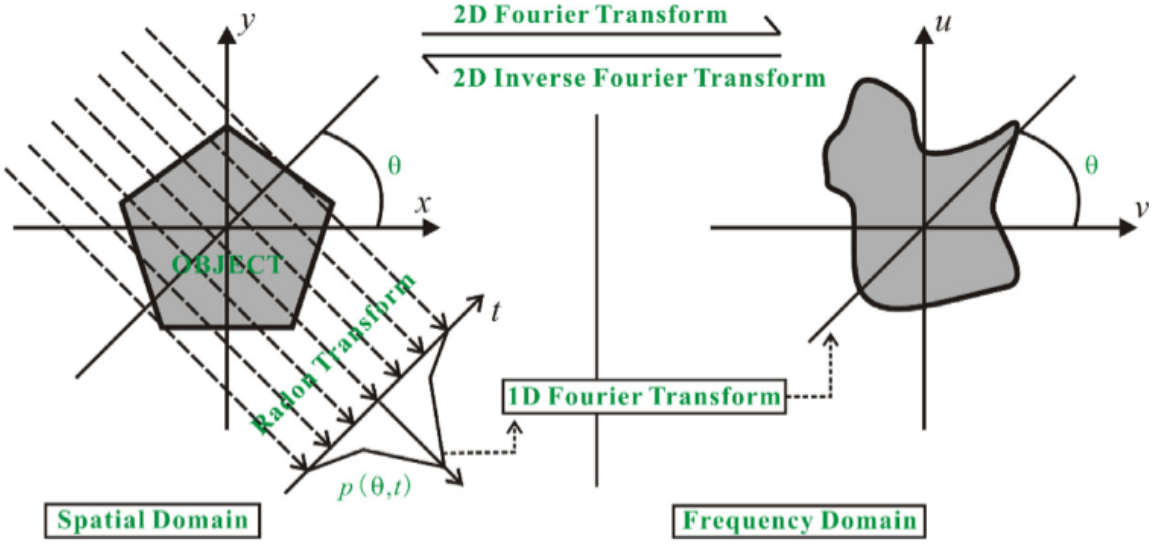

Figure 2.3: Illustration of the Fourier slice theorem and the filtered back-projection algorithm [3].

2.3.2 Algebraic Reconstruction Techniques

In contrast to classical tomography algorithms that use analytical solutions, in Algebraic Reconstruction Techniques (ART), the flow field is discretized into finite pixels as shown in Figure 2.4 and the forward problem is formulated as a matrix-vector multiplication, which is then solved iteratively. In Figure 2.4, the absorption length of the ith LOS (the red line) passing through the jth pixel is labeled as W_{ij} and the projection data of the ith LOS is labeled as P_i. Writing Equation 2.11 for all the LOS yields a system of linear equations:

$$\mathbf{W}\vec{f} = \vec{P} \tag{2.12}$$

where $\vec{f}$ and $\vec{P}$ represent the projection data for all LOS and the field variable $f(x, y)$ evaluated at each pixel, respectively, both organized in vector forms. The matrix $\mathbf{W}$ is called the 'weight matrix' with elements W_{ij} weighting the contribution of the jth pixel f_j to the projection measurement P_i.

The ART algortihm solves the matrix equation 2.12 iteratively with the following basic form:

$$\vec{f}^{(k+1)} = \vec{f}^{(k)} + \beta \frac{P_i - \vec{w}_i^T \cdot \vec{f}^{(k)}}{\vec{w}_i^T \cdot \vec{w}_i} \vec{w}_i \tag{2.13}$$

where k is the current iteration, β is a relaxation parameter, P_i is the ith projection, and $\vec{w}_i$ is the ith row of $\mathbf{W}$, arranged as a column vector. In each iteration, the difference between the guessed value and the measured projection is calculated and used to update the pixels along the LOS until a convergence criterion is met. However, the ART algorithm suffers from semi-convergence [52]. ART approaches the true solution in early iterations but diverges away as the iteration steps increase due to high-frequency contributions from noise. Therefore, it's difficult to determine a proper stopping criterion in practice. In addition, since only pixels that transect the LOS will be updated, ART is usually used in LAT measurements with relatively small number of pixels (typically 100–1000) and comparable number of projection measurements [53–57]. Several variations of ART have also been developed, including the simultaneous iterative reconstruction technique (SIRT) and the multiplicative ART (MART) algorithms, each one with its own advantages in different applications. A comparison of these algorithm in LAT can be found in [58].

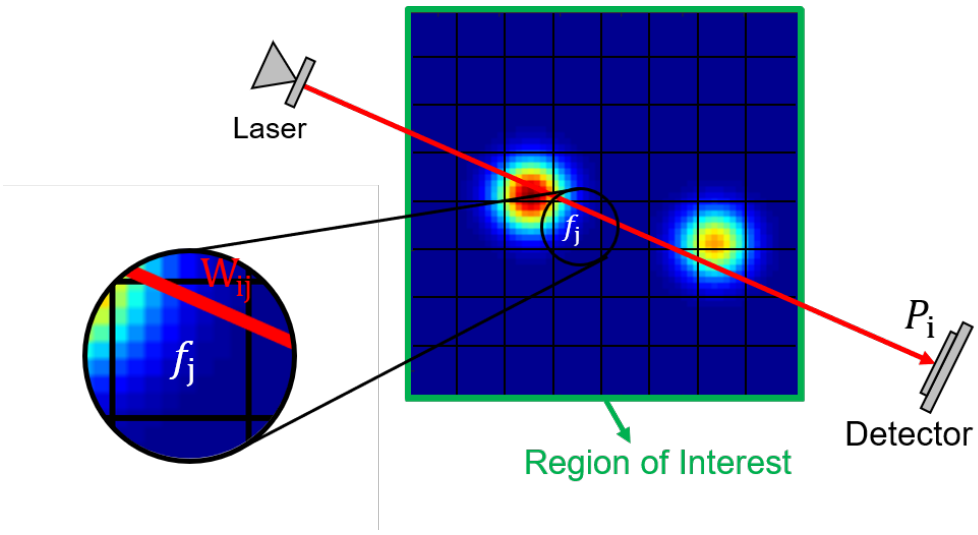

Figure 2.4: Discrete formulation of the 2D LAT problem.

2.3.3 Limited Angle Tomography and Regularization

LAT measurements often result in an ill-posed linear matrix equation. The problem is ill-posed in two aspects for two distinct reasons: Firstly, for fully-determined or overdetermined systems—where the number of measurements is equal to or greater than the number of unknowns—the ill-posed nature is dictated by the noise amplification as discussed in 1D tomography previously. Secondly, for underdetermined systems—where the number of measurements is less than the number of unknowns—the problem is ill-posed predominately because an infinite number of solutions may exist. 2D LAT measurements typically result in an underdetermined system because a large number of grid points are needed to resolve complicated flow fields where fewer projection measurements can be made due to limited optical access and/or high experiment cost. This is referred as the *limited-angle tomography problem*. As such, regularization methods that incorporate additional information are often used to achieve better solutions.

2.3.3.1 Tikhonov Regularization

As mentioned before, Tikhonov regularization has been widely used in 1D tomography to dampen the instability of the inversion process [38]. For 2D limited-angle tomography, Tikhonov regularization also serves as *a priori* information that the solution should be smooth and non-negative in addition to dampening the noise amplification. Similarly to 1D tomography, the underdetermined linear equation system 2.12 is augmented by an additional set of equations $\lambda \mathbf{L}\vec{f} = 0$, where λ is the regularization parameter and $\mathbf{L}$ is the 2D version of discrete Laplacian matrix that is used to enforce the smoothness condition:

$$L_{i,j} = \begin{cases} 1 & i = j \\ -1/n_i & i \text{ neighbors } j \\ 0 & \text{otherwise} \end{cases} \tag{2.14}$$

where n_i is the number of neighboring pixels around the ith pixel. The flow field then can be reconstructed by solving the following optimization program:

$$\vec{f}_\lambda = \arg\min \left\| \begin{bmatrix} \mathbf{A} \\ \lambda \mathbf{L} \end{bmatrix} \vec{f} - \begin{bmatrix} \vec{P} \\ 0 \end{bmatrix} \right\| \tag{2.15}$$

Again, the regularization parameter λ is essential for good reconstruction results. Similarly to 1D tomography, λ can be determined by the L-curve method. Alternatively, Daun et al. [59] proposed a criterion based on the singular values of the augmented matrix system. In this criterion, the regularization parameter λ is chosen to yield a value that pads the small singular values but does not overwhelm the large nontrivial singular values. Tikhonov regularization has been successfully used in LAT to reconstruct 2D temperature and species profiles in reacting flows, both based on simulation studies [59–61] and experimental studies [35, 62]. However, limited angle tomography with Tikhonov regularization often results in a blurring effect and artifacts in the reconstructed flow-field [59, 62]. This motivates different regularization methods, especially through Bayesian formulations, and will be discussed in the next section.

2.3.3.2 Regularization via Bayesian Formulation

As shown for Tikhonov regularization in the previous section, incorporating prior information helps address the ill-posed nature of the limited angle tomography problem to produce unique and stable solutions. Recently, an alternative approach based on a Bayesian framework has been demonstrated to more robustly incorporate various prior information in the inversion process. In this framework, all quantities are treated as random variables with an associated probability density function (PDF). These quantities are related through Bayes' equation [61]:

$$\pi(\mathbf{f}|\mathbf{P}) = \frac{\pi(\mathbf{P}|\mathbf{f})\pi_{\mathrm{pr}}(\mathbf{f})}{\pi(\mathbf{P})} \propto \pi(\mathbf{P}|\mathbf{f})\pi_{\mathrm{pr}}(\mathbf{f}) \tag{2.16}$$

where the likelihood $\pi(\mathbf{P}|\mathbf{f})$ is the PDF for observing the measurement $\mathbf{P}$ given some candidate solution $\mathbf{f}$; the prior $\pi_{pr}(\mathbf{f})$ is the likelihood for candidate solutions $\mathbf{f}$ accounting all

knowledge about the flow field, independent of the measurement data; the evidence $\pi(\mathbf{P})$ is a constant scalar that normalizes the numerator to conserve total probability; and the posterior $\pi(\mathbf{f}|\mathbf{P})$ is the pdf of $\mathbf{f}$ subject to the measurement data in $\mathbf{P}$. This can then be solved via maximum *a posteriori* (MAP) estimation:

$$\mathbf{f}^{\mathrm{MAP}} = \mathrm{argmax}\{\pi(\mathbf{f}|\mathbf{P})\} \tag{2.17}$$

By customizing Equation 2.16, one can easily incorporate different prior information in addition to smoothness and non-negativity as in Tikhonov regularization. This method has shown promise in improving reconstruction quality, reducing artifacts, and helping design beam arrangements in the tomography experiments [35, 61, 63]. More detailed discussions on the theory and applications of the Bayesian framework inversion are can be found in [64].

2.3.4 Non-linear Absorption Tomography

The aforementioned tomographic reconstruction techniques are based on a linear set of equations, and thus are classified as linear tomography. Alternatively, the forward problem can be recast as a set of non-linear equations with the temperature and the mole fraction fields as objective functions to solve:

$$p(L_j, \lambda_i) = \int_l \sum_k S(\lambda_k, T(l)) \cdot X(l) \cdot \phi\left(\lambda_k - \lambda_i\right) \cdot P \cdot dl \tag{2.18}$$

where $p(L_j, \lambda_i)$ is the projection at location L_j and wavelength λ_i; l is the integration path; $S(\lambda_k, T(l))$ is the temperature-dependent linestrength for a transition λ_i; X is the mole fraction; P is the pressure; and ϕ is the lineshape function. The flow field is discretized in a similar manner as in linear tomography shown in Figure 2.5 and Equation 2.18 can discretized accordingly. The temperature and the mole fraction field can then be reconstructed spontaneously by minimizing the following cost function:

$$F\left(T^{rec}, X^{rec}\right) = \sum_{j=1}^{J} \sum_{i=1}^{I} \frac{\left[p_m\left(L_j, \lambda_i\right) - p_c\left(L_j, \lambda_i\right)\right]^2}{p_m\left(L_j, \lambda_i\right)^2} + \gamma_T \cdot R_T\left(T^{rec}\right) + \gamma_X \cdot R_X\left(X^{rec}\right) \tag{2.19}$$

where $p_m(L_j, \lambda_i)$ is the measured projection data; $p_c(L_j, \lambda_i)$ is the calculated projection based

on the reconstructed temperature and mole fraction profiles (T^{rec}, X^{rec}); I is the number of measured spectral transitions; J is the number of discrete pixels to solve; $\gamma_T R_T\left(T^{rec}\right)$ and $\gamma_X R_X\left(X^{rec}\right)$ are regularization terms for temperature and concentration, respectively. More details of the mathematical formulation can be found in [65, 66].

In this approach, additional information is provided by measuring more spectral transitions instead of more projection angles, and therefore the approach is also known as *hyperspectral tomography*. Hyperspectral tomography has been successfully applied to spontaneously retrieve 2D temperature and species concentration in different applications, including in the canonical Hencken burner [67], in swirl flames [68], at the exhaust plane of an aero-propulsion engine [34], and in a semiconductor process chamber [69]. Hyperspectral tomography has also been used to retrieve 1D temperature and species concentration in the cononical McKenna burner [70]. However, for the non-linear tomography problem, the cost function F is usually non-convex, meaning that local minimums exist and the solution might not converge to the global minimum. Therefore, heuristic techniques such as genetic algorithms and simulated annealing are employed to identify the global minimum. These algorithms can be difficult to implement, since their performance depends on problem-specific heuristics, and they are often time-consuming to compute [3, 35].

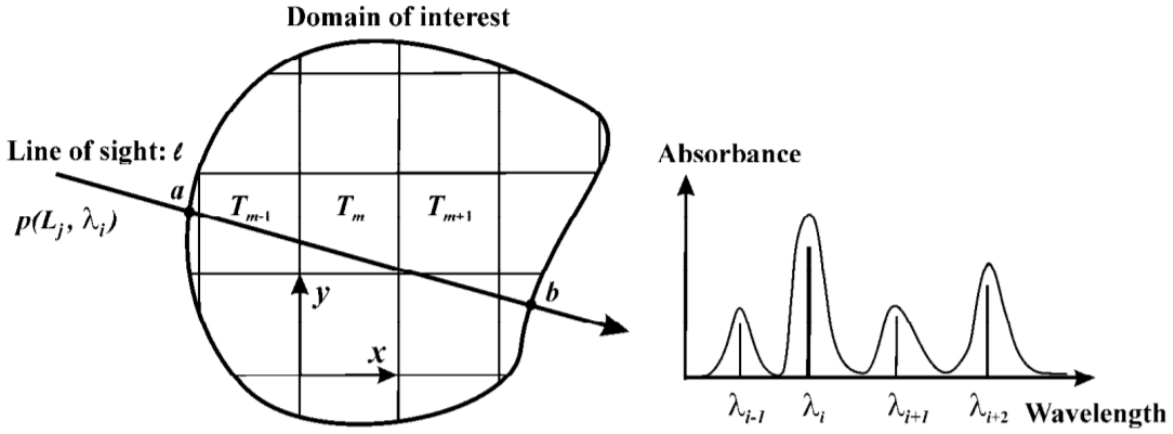

Figure 2.5: The mathematical formulation of the non-linear tomography problem [67].

2.3.5 Deep Learning Inversion

Most recently, deep learning methods are widely applied to image reconstruction and have achieved impressive results in various image reconstruction tasks, especillay in medical imaging, including low-dose denoising, sparse-view reconstruction, limited angle tomography and artifact reduction. An excellent review can be found in the special issue of IEEE Transaction on Medical Imaging [71]. Instead of solving the inverse problem directly through analytical methods, the deep learning methods recast the image reconstruction task into a data-driven problem. In this approach, a large library of known ground truth results are used as training dataset and deep neural networks are used to build connection between the projections and reconstruction results. By learning the intricate features and representations from the large amount of tomography data, high-fidelity reconstruction results can be achieved by the deep neural networks. Recently, predictive models utilizing deep neural networks have been applied for combustion flow imaging. However, these efforts have been focused on simulated flows [72] and emission measurements of real flows [19, 73, 74]. In this dissertation, we present the first 3D laser absorption imaging of methane in a flame, evaluated both by simulation and experiment (detailed in Chapter 7).

CHAPTER 3

Advances in Mid-infrared Laser Absorption Spectroscopy

3.1 Introduction

Laser absorption spectroscopy (LAS) plays an important role in combustion diagnostics due to its quantitative, species-specific, calibration-free, and non-intrusive nature. LAS has been widely used to diagnose and characterize different combustion systems, either through path-averaged measurements or through LAT algorithms to image the flow fields. Historically, these measurements have mostly been perfromed in the near-infrared (760–2500 nm) where robust and affordable hardware are available due to the development of telecommunication industry in the 1990s [2]. Recently, advancements in mid-infrared photonics, especially in mid-infrared tunable, room-temperature semi-conductor lasers, have provided convenient access to nearly the entire IR spectrum (0.8–16 μm), enabling unique sensing capabilities and species-detectability.

In this chapter, the fundamentals of LAS will be discussed with an emphasis on the mid-infrared spectrum of the combustion gases; specifically the fundamental vibrational bands of hydrocarbon intermediates and carbon oxides are in this domain. Recent advancements in mid-infrared hardware are then discussed, followed by a brief review on applications enabled by these technologies. A more detailed review on this topic can be found in [2].

3.2 Mid-infrared Spectrum of Combustion Gases

LAS exploits resonance with discrete energy modes of gas molecules to ascertain thermo-chemical properties of flow fields from light absorption [1]. Molecules with dipole moments will interact and absorb photons with energy equal to the spacing between two discrete energy states. The wavelengths at which molecules absorb are related to the energy spacing by the Planck's Law:

$$\Delta E = E_{\text{upper}} - E_{\text{lower}} = h\nu \tag{3.1}$$

Here ΔE is the energy of the photon associated with a molecular transition between two quantum states, while ν is the frequency of the photon, and h is Planck's constant. In the infrared, this corresponds to the spacing between two ro-vibrational states; many combustion gases absorb in this wavelength range as shown in Figure 3.1, with the intensity of various IR absorption transitions for a few combustion species at 1500 K. It should be noted that the fundamental vibrational bands at mid-IR wavelengths (2.5–12 μm) are orders of magnitude stronger than the overtone and combination bands in the near-IR (0.75–2.5 μm), and provide much greater species sensitivity at short optical path-lengths, making them suitable for analyzing small-diameter flows in practical combustion applications.

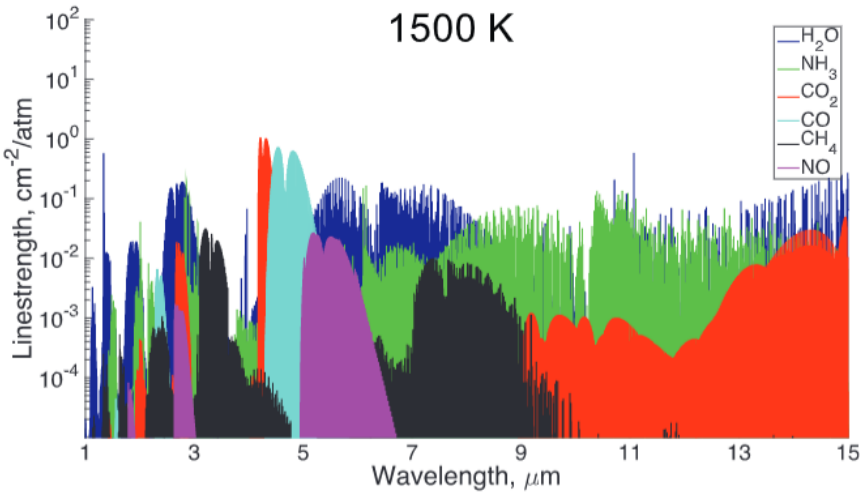

Figure 3.1: Linestrengths of several molecular species of interest to combustion systems [2]

3.3 Mid-infrared hardware

Many advances in diagnostic techniques often arise from advancements in photonics (e.g., light sourses and detectors). The current work is no exception. In this section, emerging mid-IR hardware leveraged in the current work will be briefly discussed.

3.3.1 Lasers

First and perhaps most importantly, recent technical progress and commercial maturity in room-temperature wavelength-tunable mid-infrared semi-conductor lasers (e.g., interband- and quantum-cascade lasers) provide light sources for researchers to easily access the fundamental vibrational frequencies in the mid-infrared. Quantum cascade lasers (QCLs) are semiconductor lasers that emit in the mid- to far-infrared ($\approx$ 3.5–100 μm) wavelength range with similar tuning capability and usability to room-temperature diode lasers. A QCL consists of a periodic series of thin layers of varying material composition forming a superlattice, which introduces a varying electric potential across the length of the device. Because the position of the energy levels in the system is primarily determined by the layer thicknesses and not the material, it is possible to tune the emission wavelength of QCLs over a wide range in the same material system. The first demonstration of the quantum cascade laser occurred at Bell Laboratories in 1994. Fabry-Perot (FP) quantum cascade lasers were first commercialized in 1998, Distributed feedback (DFB) devices were first commercialized in 2004, and broadly-tunable external cavity quantum cascade lasers first commercialized in 2006. QCLs are now available for a wide range of wavelengths from multiple vendors (e.g., Alpes, Adtech, Daylight Solutions, Hamamatsu, Pranalytica) [2].

Interband cascade lasers (ICLs) use a layered heterogeneous band-structure to achieve cascading of photon emission similar to QCLs. However, ICLs generate photons with interband transitions, rather than the inter-subband transitions used in QCLs. The use of interband transitions allows laser action in ICLs to be achieved at lower electrical input powers than is possible with QCLs. The basic concept of an ICL was proposed by Rui Q.

Yang in 1994 [75]. ICLs lasing in continuous wave (CW) mode at room temperature were first demonstrated in 2008 at 3.75 μm [76]. Subsequent advancements in tuning response and efficiency have enabled commercially available, compact, narrowband DFB ICL lasers that fill a gap (3–4 μm) in the mid-wave infrared between conventional room-temperature diodes and quantum-cascade lasers. This region is especially important to combustion due to the very strong C−H stretch vibrational mode common to all hydrocarbons near 3.4 μm [2].

3.3.2 Infrared Detectors and Cameras

Indium-antimonide (InSb) and mercury-cadmium-telluride (HgCdTe or MCT) are the most common semiconductor materials used for mid-infrared detectors. These detectors are available in both photoconductive and photovoltaic operation modes. In the former, the electrical resistance is influenced by the incident photons and, in the latter, current is generated by the photoelectric effect. For these mid-IR materials, photovoltaic operation is typically preferred due to its lower dark current. InSb photovoltaic detectors are sensitive from ∼1 to 5.5 μm and must operate at cryogenic temperatures (∼80 K); they are typically packaged with a dewar for liquid-nitrogen cooling. MCT detectors (photovoltaic or photoconductive), on the other hand, can be sufficiently cooled thermo-electrically providing for a more portable and less cumbersome package that can be mounted at any orientation, which is useful for engine sensing applications. The amount of cadmium in the MCT alloy can be chosen to tune the sensitive wavelength region within a broad range of (∼2–15 μm).

Recent developments in the infrared detector technology have also made possible the development of high performance infrared cameras for use in a wide variety of thermal imaging applications. These infrared cameras are now available with spectral sensitivity in the shortwave, mid-wave and long-wave spectral bands or alternatively in two bands, covering the whole infrared wavelength range of (∼1.5–12 μm). In addition, a variety of camera resolutions are available as a result of mid-size and large-size detector arrays and various pixel sizes. For example, Telops provides high-speed infrared cameras with 320 × 256 pixel resolution and 640 × 512 pixel resolution. Also, camera features now include high

frame rate imaging (up to 100 kHz), adjustable exposure time and event triggering enabling the capture of temporal thermal events.

3.4 Summary

Recent advances in mid-infrared optical equipment have provided several new capabilities for LAS sensing in combustion environments. Access to the fundamental vibrational bands in the mid-infrared not only allows for new species-detectability but also more sensitive detection at a shorter pathlengths compared to that in the near-infrared region. However, these developments have rarely been leveraged in the development of LAT systems. In this dissertation, emerging mid-infrared optical equipment is leveraged to design a novel tomographic imaging system. Specifically, Chapter 4 and 5 demonstrates a translation-stage-mounted laser-spectrometer systems that takes advantages of the compact and portable mid-infrared lasers and detectors. Chapters 6 and 7 present a novel laser absorption imaging system that utilize high-speed infrared camera to achieve enhanced spatial and temporal resolution.

CHAPTER 4

Mid-IR Laser Absorption Tomography of CO, CO_2 in Turbulent Premixed Jet Flames

The contents of this chapter have been published in the journal ***Applied Physics B: Lasers & Optics*** *under the full title 'Mid-infrared laser absorption tomography for quantitative 2D thermochemistry measurements in premixed jet flames' [32].*

4.1 Introduction

Most practical combustion devices involve turbulent reacting flows. Understanding interactions between chemistry and fluid dynamics in turbulent flames is of prime interest to the combustion community, both for the development of more efficient engineering devices and the development and refinement of numerical models [6]. As computational power increases and higher-fidelity simulations of turbulent flames with more detailed chemistry become possible, it is necessary to provide measurements to inform and anchor these models [77]. Specifically, quantitative measurements of the thermochemical structure (i.e. spatially-resolved species and temperature) are needed to elucidate the coupled mechanisms.

Traditional intrusive measurement techniques such as thermocouples and gas chromatography (using sampling probes) disturb the local flow field, often precluding definitive interpretation. As such, several non-intrusive spectroscopic measurement techniques have been utilized to study turbulent flames by exploiting emission, absorption, and scattering interactions. For turbulent jet flames, which are the focus of this work, Rayleigh scattering has been a common approach for thermometry [25–27], and can be quantitative with an estimation of

gas composition [28–30]. Raman scattering methods have also been used for time-resolved point measurements of species in such flames [78–80]; however, this approach does not readily lend towards characterizing the structure of a flame unless many point measurements are made [81, 82], which can be difficult to perform if the burner is immobile and the lasers are large and cumbersome, which is often the case with high-powered light sources required in scattering spectroscopies. Laser induced fluorescence (LIF) [79, 83–85] and chemiluminescence [84, 86, 87] have also been used extensively for temperature and species-specific imaging. However, these methods do not easily yield quantitative species measurements, even with calibrations [1].

Although typically weak in spatial resolution capability (due to line-of-sight integration), laser absorption spectroscopy (LAS) provides a highly quantitative, calibration-free method of measuring major combustion species and temperature in harsh environments using compact low-power semiconductor lasers [2]. Room-temperature interband cascade lasers (ICLs) and quantum cascade lasers (QCLs) enable convenient access to the strong mid-infrared (mid-IR) absorption bands of CO and CO_2 centered near 4.7 and 4.3 μm, respectively, as shown in Fig. 4.1. The fundamental vibrational bands at these mid-IR wavelengths are orders of magnitude stronger than those in the near-IR, and provide much greater species sensitivity at short optical path-lengths, making them suitable for analyzing small-diameter flows in practical combustion applications. By carefully selecting the wavelength, it is possible to measure multiple absorption transitions of a single molecule with one laser, enabling simultaneous calibration-free thermometry and species concentration measurements [89].

The compactness and mobility of modern ICLs and QCLs readily enables spatially resolved measurements in flames, which can be combined with tomographic reconstruction techniques [37, 38] to characterize non-uniform flows [40, 67, 90–94]. In this paper, we present a stage-mounted multi-laser absorption system for quantitative measurement of species concentrations and temperature distributions in turbulent premixed jet flames.

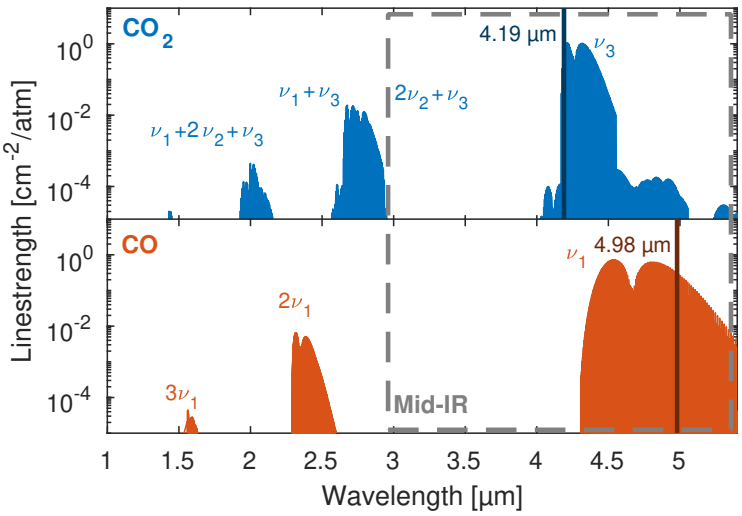

Figure 4.1: Absorption linestrengths for CO_2 (top) and CO (bottom) from 1 to 5 μm computed from the HITRAN database [88]; $T = 1500$ K. Fundamental vibrational bands ν_i as well as combinations of these bands are labeled for each species. Accessible regions in mid-infrared wavelengths due to the recent availability of mid-infrared ICLs and QCLs are marked with a gray dashed box. Wavelengths specifically used in this study are marked with darker lines.

4.1.1 Theory of laser absorption spectroscopy

Laser absorption spectroscopy (LAS) exploits resonance with discrete energy modes of gas molecules to ascertain thermochemical properties of flow fields from light absorption [1]. We briefly review the fundamentals of LAS here in the context of the experiment to provide reader assistance with the measurements that follow.

The Beer-Lambert law in Eq. 4.1 gives the spectral absorbance α_ν in a gas medium axially symmetric about radius r [cm] for a specific frequency ν [cm^{-1}] as a function the ratio of incident light, I_0, and the transmitted light, I_t [1]:

$$\alpha_\nu = -\ln\left(\frac{I_t}{I_0}\right)_\nu = \int_0^{L(r)} PS_j(T(r))X_{\text{abs}}(r)\varphi_\nu dl \tag{4.1}$$

α_ν thus depends on total pressure P [atm], line-strength S_j [cm^{-2}/atm] for rovibrational transition j, mole fraction of absorbing species X_{abs}, lineshape function φ_ν [cm], and aggregate path length $L(r)$ [cm]. For an integrated line-of-sight (LOS) absorption measurement through a non-uniform medium (such as a flame) that is axially symmetric in r, the projected integrated absorbance area $A_{j,proj}(r)$ [cm^{-1}] is expressed in Eq. 6.1,

$$\begin{aligned} A_{j,proj}(r) &= \int_{-\infty}^{\infty} \alpha_\nu d\nu = \int_0^{L(r)} K_j(r) dl \\ &= P\int_0^{L(r)} S_j(T(r))X_{\text{abs}}(r) dl \end{aligned} \tag{4.2}$$

where P is assumed constant throughout the medium. In this work, we attained $A_{j,proj}(r)$ by fitting a Voigt function to the measured α_ν for each line j, effectively negating the measurement dependence on line shape φ_ν [1]. To determine a radial profile of the integrated spectral absorption coefficient, $K_j(r)$ [cm^{-2}], from radially resolved projected area measurements $A_{j,proj}(r)$, we use tomographic reconstruction methods discussed in greater detail in Section 6.2.2.3. For multiple transitions j scanned, multiple $K_j(r)$ can be determined, and the ratio of two absorption coefficients reduces to a ratio of $S_j(r)$, which is a function of $T(r)$ only, as shown in Eq. 5.3.

$$R(r) = \frac{K_A(r)}{K_B(r)} = \frac{S_A(T(r))}{S_B(T(r))} = f(T(r)) \tag{4.3}$$

Since $S_j(T(r))$ is a line-specific spectroscopic property, it is possible to infer the gas temperature $T(r)$ with the simultaneous measure of two lines at any location r [89]. After temperature has been determined, $S_j(T(r))$ can be evaluated, and the mole fraction of the absorbing species $X_{abs}(r)$ can be obtained using Eq. 6.2 when the total pressure P is known. More detail on these calculations as well as their uncertainties can be found in Appendix A.

$$K_j(r) = PS_j(T(r))X_{\text{abs}}(r) \tag{4.4}$$

4.2 Method

We employ a scanned-wavelength direct-absorption technique with a tunable quantum cascade laser and an inter-band cascade laser to spectrally resolve transitions near the fundamental bands of CO and CO_2 near 4.9 μm and 4.2 μm, respectively. Using mechanical translation stages and tomographic reconstruction techniques, we provide radial profiles of CO and CO_2 mole fraction as well as gas temperature for two different turbulent flow conditions in a piloted premixed jet flame burner.

4.2.1 Wavelength selection

For this and other combustion studies, specific wavelengths within each vibrational band of both CO_2 and CO were selected based on the isolation, strength, and temperature sensitivity of the rovibrational lines, in addition to laser availability. We probe the P(0,31) and P(1,26) lines of the fundamental band of CO, around 2008.53 cm^{-1} and 2006.78 cm^{-1}, respectively, to infer CO vibrational temperature and CO mole fraction. For CO_2, we probe the R(0,58) line at 2384.189 cm^{-1}, as well as the doublet line pair R(1,105) and R(1,106) at 2384.327 cm^{-1} and 2384.331 cm^{-1}, respectively to measure CO_2 mole fraction and vibrational temperature. Relevant spectroscopic parameters of the selected lines are shown in Tables 4.1 and 4.2, where linestrength and lower-state energy values for CO and CO_2 are taken from the HITEMP 2010 database [88]. Further details on line selection within these domains are described in previous

Table 4.1: Spectroscopic parameters, targeted CO_2 transitions

Line (v'', J'')	Wavelength [nm]	Freq. [cm^{-1}]	E'' [cm^{-1}]	S (296 K) [cm^{-2}/atm]
R(0,58)	4,194.30	2384.189	1,333	7.78×10^{-1}
R(1,105)	4,194.06	2384.327	4,998	2.51×10^{-8}
R(1,106)	4,194.05	2384.331	5,087	1.65×10^{-8}

Table 4.2: Spectroscopic parameters, targeted CO transitions

Line (v'', J'')	Wavelength [nm]	Freq. [cm^{-1}]	E'' [cm^{-1}]	S (296 K) [cm^{-2}/atm]
P(1,26)	4,983	2006.78	3,478	5.20×10^{-6}
P(0,31)	4,979	2008.53	1,901	6.62×10^{-3}

studies [89, 95].

4.2.2 Laser absorption tomography system

As noted, the medium in which we attain the measurements is non-uniform, though it is assumed to be axially-symmetric over a short time interval [86]. In this subsection, we describe the system used to mechanically obtain spatial resolution for the LAS measurements. Figure 4.2 shows the optical configuration around the piloted premixed jet flame burner at the University of Southern California, as well as the directions of radial and vertical translation.

A stage-mounted two-laser system was developed to measure species profiles of CO and CO_2, respectively, as well as temperature in the radial and vertical directions to characterize the time-averaged thermochemical structure of the flame. A distributed-feedback (DFB) quantum cascade laser (QCL) with ≈ 50 mW output power was utilized as the single-mode light source to resolve the selected CO lines and infer thermochemical properties of CO. An interband cascade laser (ICL) with ≈ 5 mW output power is similarly used for probing the

CO_2 lines. The laser beams were aligned concentrically using flat mirrors and beam splitters as shown in Fig. 4.2. Focusing mirrors (f= 200 mm) 400 mm apart were deployed on optical rails attached to the stage to focus the concentric beams to approximately 0.5 mm in diameter across the central jet. After reflection back towards the detectors, we used another beam splitter in conjunction with bandpass spectral filters (4210 nm for CO_2, 5000 nm for CO) and focusing lenses to separate the different wavelengths onto independent detectors. The lasers, mirrors, lenses, and detectors were all mounted on a ∼16 cm × 16 cm optical breadboard on an automatic radial (horizontal) translation stage, which itself was mounted on a manual vertical translation stage. The horizontal translation stage was controlled by a stepper motor with a controllable linear translation resolution of 1.6 μm per motor step in the r direction, as indicated in Fig. 4.2. The hand-cranked vertical translation stage had a linear translation resolution of 1.27 mm in the x direction per lead screw revolution. Signals from the stepper motor encoder were recorded alongside the the signals from the photovoltaic detectors. Additionally, the stepper motor was operated with a stepping frequency that was a sub-multiple (500 Hz) of the laser scan rate so that the r location of the laser beams could be easily tracked.

4.2.3 Piloted premixed jet flame burner

A discussion of the operating characteristics of the University of Southern California burner is presented here for ease of reader understanding in the sections that follow. The current work utilized a modified Piloted Premixed Jet flame Burner (PPJB) design [26] as described in greater detail in previous studies [86, 87]. The burner consists of a central jet tube of inner diameter D = 5.84 mm surrounded by a pilot and outer coflow (D_{coflow} = 400 mm) in order to stabilize the high velocity central jet. A schematic of the configuration with the laser absorption system is shown in Fig. 4.2. The pilot flame anchors the central jet to the burner exit in order to prevent blowoff from the high shear present. The pilot flame is a premixed C_2H_4/air flame stabilized beneath the jet flame with an equivalence ratio of ϕ=0.8 and an unburnt exit velocity of 0.75 m/s.

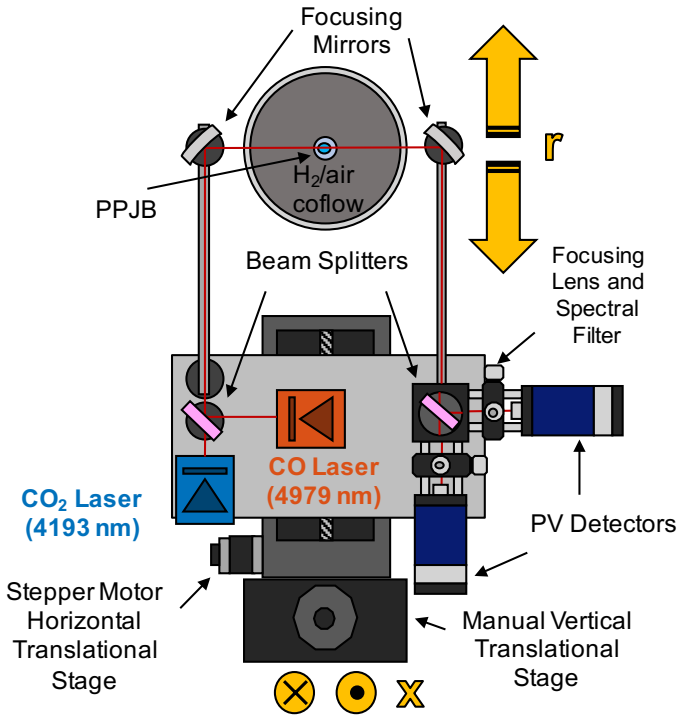

Figure 4.2: Top-down schematic of the PPJB with optomechanical translation stage system. The central jet is surrounded by a coflow H_2/air flame. The lasers, optics, and detectors are mounted to the same translational stages and move together while the burner remains stationary.

The coflow surrounds the pilot and jet flow, using hot products to thermally insulate the jet. A pure H_2/air flame at ϕ=0.51 was used to provide a surrounding temperature of $T_{\text{coflow}} = 1500$ K. This coflow flame composition was chosen to provide hot products without carbon atoms present so as to provide zero concentration boundary conditions for the CO and CO_2 mole fraction reconstruction efforts. Experiments were performed at two jet Reynolds numbers, $Re_{\text{jet}} \equiv u_{\text{jet}} D/\nu_{\text{visc}} = 25{,}000$ and 50,000, where U_{jet} is the bulk flow velocity and ν_{visc} is the kinematic viscosity at the burner exit. The coflow velocity does not change across the Reynolds number conditions. The mixture composition of the central jet is C_2H_4/air at ϕ=0.55 and an unburned mixture temperature of 298 K. As mentioned, over a modest time interval ($\sim 10^2$ ms), the turbulent jet can generally be approximated as axially symmetric and steady [86].

4.2.4 Experimental procedure

To determine the center of the jet ($r = 0$) for initial alignment, the laser beams were adjusted in the r direction across the central jet tube using the automatic horizontal stage. Locations where the detected light intensity decreased to ∼20% of the unblocked intensity due to the obstruction of the jet tube were noted, and the location of the jet center was then determined by radial symmetry. Both the CO and CO_2 lasers were scanned at a frequency of 1 kHz, and were recorded at a sample rate of 2 MHz, as shown in Fig. 4.3. For the QCL, the targeted CO transitions could not be accessed with a single laser sweep at a given laser operating temperature; therefore, the CO lines were measured by sequential horizontal scans at different laser operating temperatures, at each height x above the jet exit. The CO laser operating conditions were changed and stabilized in ∼30 s intervals between the two horizontal scans. Since the experiment under investigation is quasi-steady [86], this was considered an acceptable method to capture both CO transitions. The stepper motor encoder signals from the automatic horizontal translation stage were also recorded at the same frequency. The horizontal translation speed was 0.8 mm/s, resulting in two laser scans per 1.6 μm step. To measure the baseline signal I_0, background measurements were

taken with the lasers during an automatic horizontal translation while the H_2/air co-flow of the burner was on, but without any hydrocarbon fuels flowing, for every r position at the minimum and maximum x locations for the flame. These background measurements with the hot coflow gases account for incident effects from environmental thermal emission and water absorption, as well as CO_2 in the ambient air. No significant differences in absorption were observed using either x location background measurement. As the burner was operating, finely resolved horizontal scans in the r direction were made every 20 mm in height above the burner exit. The system was translated as far as $r = 32$ mm to ensure zero concentration boundary conditions for later reconstruction efforts, as detailed in Section 6.2.2.3. Once a translation was completed for a given r-x combination, the horizontal stage was returned to the $r = 0$ location and the vertical translation stage was adjusted in the x direction to a new height above the jet exit. This process was repeated for several axial locations x along the flame. For the case in which Re = 25,000, fewer x locations were scanned since the flame was shorter. This simultaneous translation and data acquisition method was chosen to maximize spatial data collection of the mean flow properties during the available test time.

4.3 Data Analysis

This section presents the methods we employed to interpret the measurements obtained in the experiment into axial and radial profiles of temperature and species measurements. For the results shown here, 105 direct-absorption scans (Fig. 4.3) associated with a horizontal translation interval were averaged prior to the calculation of projected absorbance area $A_{j,proj}(r)$ via Eqs. 4.1 and 6.1. This procedure is done for each spatial interval throughout the horizontal scan and allows for statistical analysis of the signals in the interval. We determine the 95% confidence interval of all of these signals, and use this information to process the uncertainty in the rest of our results. The uncertainty analysis is presented in greater detail in Appendix A.

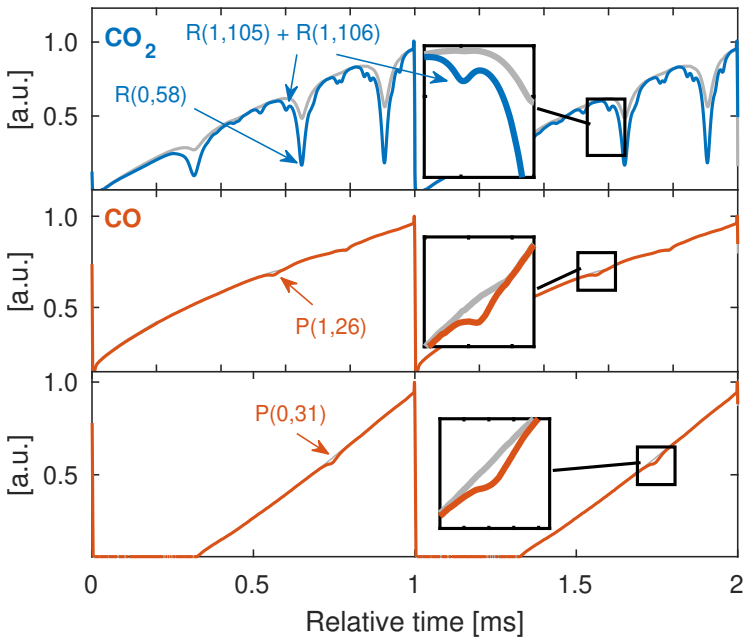

Figure 4.3: Example direct-absorption scans for selected CO_2 and CO lines (I_t) with specific transitions labeled. Gray lines indicate background signals (I_0) with the C_2H_4/air jet flame and pilot turned off but with the hot co-flow H_2/air on.

4.3.1 Spectral line fitting

The measured absorbance spectra α_ν are least-squares fit for the target spectral lines in Tables 4.1 and 4.2 using the Voigt line shape function [1] to obtain projected absorbance areas $A_{j,proj}(r)$, as shown in Figs. 4.4 and 4.5 for CO_2 and CO, respectively. $A_{j,proj}(r)$ and collisional width ν_c were free parameters for the fitting process, and Doppler width ν_D was assumed corresponding to the coflow temperature of 1500 K. It was noted that when arbitrarily assuming the temperature (from 500 K to 1500 K) for the Doppler width, there was no discernible difference for the integrated area results, which are used for tomographic reconstruction.

Due to the large difference in linestrength between the targeted CO_2 spectral lines, the regular two-line fitting procedure is not robust enough for reliably simultaneously fitting the R(0,58) line and the R(1,105) + R(1,106) doublet line without significantly biasing the fitting of the R(1,105) + R(1,106) doublet line. For this reason, we adopted a sequential fitting

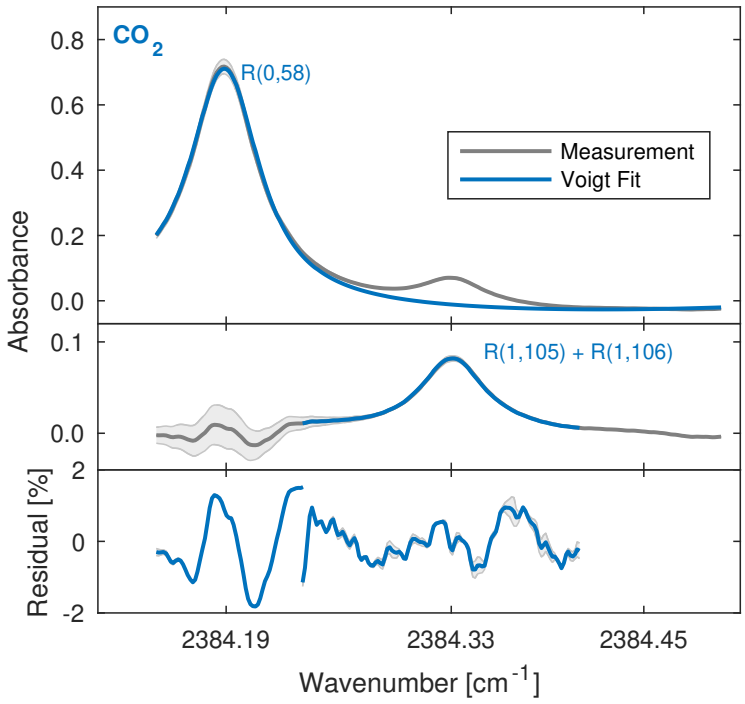

Figure 4.4: Measured carbon dioxide absorption averaged from 105 laser scans (1 kHz) shown as absorbance versus wavenumber for the R(0,58) line and the R(1,105) + R(1,106) doublet line. 95% confidence interval of measured absorbance shown in gray. *Top:* Voigt fit of solely the R(0,58) line. *Middle:* Voigt fit of the R(1,105) + R(1,106) doublet calculated from the difference between the measured data and the R(0,58) fit. *Bottom:* Residuals from each of the above Voigt fits. Variation in residuals from fitting within the bound of experimental uncertainty are shown in gray.

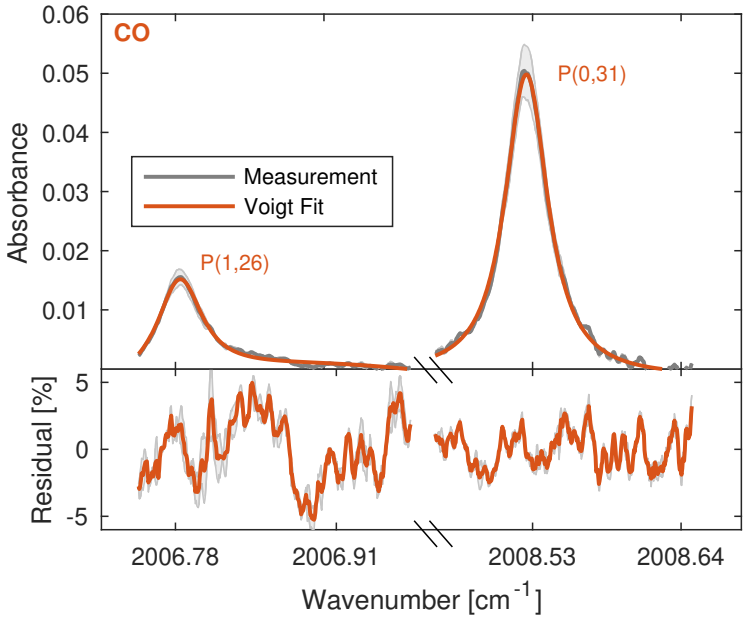

Figure 4.5: *Top:* Measured carbon monoxide absorption averaged from 105 laser scans (1 kHz) shown as absorbance versus wavenumber for the P(1,26) and the P(0,31) lines. 95% confidence interval of measured absorbance shown in gray. *Bottom:* Residuals from Voigt fit. Variation in residuals from fitting within the bound of experimental uncertainty are shown in gray.

routine in which the R(0,58) line was fit first for a specified data range (top of Fig. 4.4) after confirming that this range did not bias the $A_{j,proj}(r)$ results compared to successful simultaneous fits with the R(1,105) + R(1,106) doublet line. This Voigt fit for the R(0,58) line was then subtracted from the original measured spectral absorbance α_ν to generate a residual measurement of only the R(1,105) + R(1,106) doublet line, (middle of Fig. 4.4). This residual spectral absorbance was then fit to extract $A_{j,proj}(r)$ from the R(1,105) + R(1,106) doublet line. The final fractional residual (residual /maximum absorbance) resulting from the Voigt fits of each line was typically less than 2% for CO_2 lines (bottom of Fig. 4.4) and less than 5% for CO lines (Fig. 4.5), confirming the general appropriateness of the Voigt line shape model for this application.

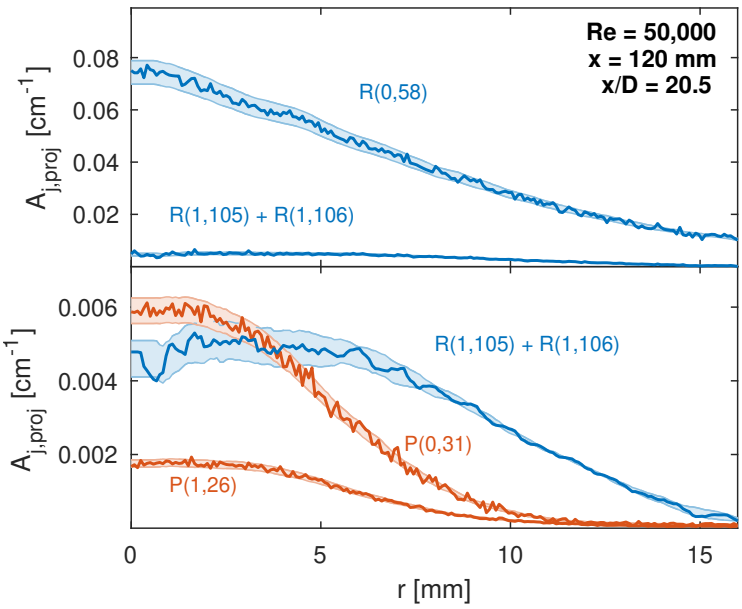

Figure 4.6: Projected integrated absorbance area, $A_{j,proj}$ for the targeted lines in radial translation space.

4.3.2 Filtering

Subsequent to fitting the absorbance measurements, radial profiles of projected absorbance area, $A_{j,proj}(r)$, are obtained for each height x above the jet exit. Figure 4.6 shows example plots of $A_{j,proj}(r)$ as a function of distance from the flame center r at $x = 120$ mm. Since both the fitting residuals (bottom of Figs. 4.4 and 4.5) and the absorbance uncertainties (Appendix A) are much less than the observed spatial variations in $A_{j,proj}(r)$, the oscillations in measured $A_{j,proj}(r)$ are interpreted as primarily flow field variations due to the turbulence rather than measurement noise. Here, we applied a Savitzky-Golay filter [96] which smooths $A_{j,proj}(r)$ with a 1st degree polynomial inside a smoothing window size of 15 points. These smoothing parameters correspond to an effective spatial resolution of 0.55 mm, similar to the diameter of the laser beam. The smoothed $A_{j,proj}(r)$ profiles, intended to represent mean values, are then used as inputs for tomographic reconstruction, detailed in the following section.

4.3.3 Tomographic reconstruction

Here, we briefly describe our approach to obtaining radial profiles of species and temperature from our path-integrated measurements. Assuming the flame is axisymmetric and steady, one-dimensional tomographic reconstruction can be applied. The projected absorbance area measurement is described by the well-known Abel transform as a line-of-sight integration over the flame with radius R at a given distance from the flame center y:

$$P(y) = 2\int_{y}^{R} \frac{f(r)r}{\sqrt{r^2 - y^2}} dr \tag{4.5}$$

where $P(y)$ is the measured projected absorbance area $A_{j,proj}(r)$ and $f(r)$ is the radial distribution of the integrated spectral absorption coefficient $K_j(r)$.

In practice, Abel inversion is implemented numerically [38]. The flame region is divided into equally spaced annular rings and the radial absorption coefficient distribution $f(r)$ is approximated by a quadratic function near radius r using the Abel 3-point (ATP) method [37]. Writing Eq. 6.1 at each radius r gives rise to a system of linear equations represented by

$$\mathbf{A_{ATP}}\vec{f} = \vec{P} \tag{4.6}$$

where $\vec{f} = [f_0, f_1, ...f_{N-1}]^T$ and $\vec{P} = [P_0, P_1, ...P_{N-1}]^T$ contain the radial absorption coefficient values and projected absorbance area values, respectively.

In this work, the measured projected absorbance areas are deconvoluted using Tikhonov regularized Abel inversion [38] to address the inherent ill-conditioned nature of the projection matrix $\mathbf{A_{ATP}}$. In this method, an additional set of equations are imposed on the solution:

$$\lambda \mathbf{L_0}\vec{f} = 0 \tag{4.7}$$

where λ is the regularization parameter that controls the level of regularization and $\mathbf{L_0}$ is a

discrete gradient operator that characterizes the smoothness of the solution:

$$\mathbf{L_0} = \begin{bmatrix} 1 & -1 & 0 & \dots & 0 \\ 0 & 1 & -1 & \dots & 0 \\ & & \dots & \dots & \\ 0 & 0 & \dots & \dots & -1 \\ 0 & 0 & 0 & \dots & 1 \end{bmatrix} \tag{4.8}$$

The regularization parameter λ characterizes the relative importance of the accuracy and smoothness of the solution. A suitable regularization parameter is determined from the L-curve method [97] to be $\lambda \approx 1$ based on the work of Daun et al. [38] and is used for all reconstructions. Combining Eq. 4.6 and Eq. 4.7, the radial distribution $f(r)$ can be found from a least-squares solution:

$$\vec{f_\lambda} = \arg\min \left|\left| \begin{bmatrix} \vec{A_{ATP}} \\ \lambda \vec{L_0} \end{bmatrix} \vec{f} - \begin{bmatrix} \vec{P} \\ 0 \end{bmatrix} \right|\right| \tag{4.9}$$

Using the procedure discussed above, projected absorbance areas $A_{j,proj}(r)$ for measured spectral lines are Abel-inverted using Tikhonov regularization to reconstruct radially-resolved integrated spectral absorption coefficients $K_j(r)$. Examples of these reconstructions are shown in Fig. 4.7. From these reconstructed absorption coefficients, temperature is calculated from the ratio of two lines at each radial position, and mole fraction is then calculated from one absorption coefficient of each species [1].

4.4 Results

Some example results from the jet flame experiments are plotted in the figures that follow. We first present radially-resolved mole fraction measurements at two different heights (x) above the jet exit for both turbulent flow conditions. Then, we present the temperature measurements for the same planes and flow conditions. Finally, we present some composite two-dimensional images comprising the mole fraction and temperature measurements for sections of both flames. For the results shown, we use the convention of plotting distances

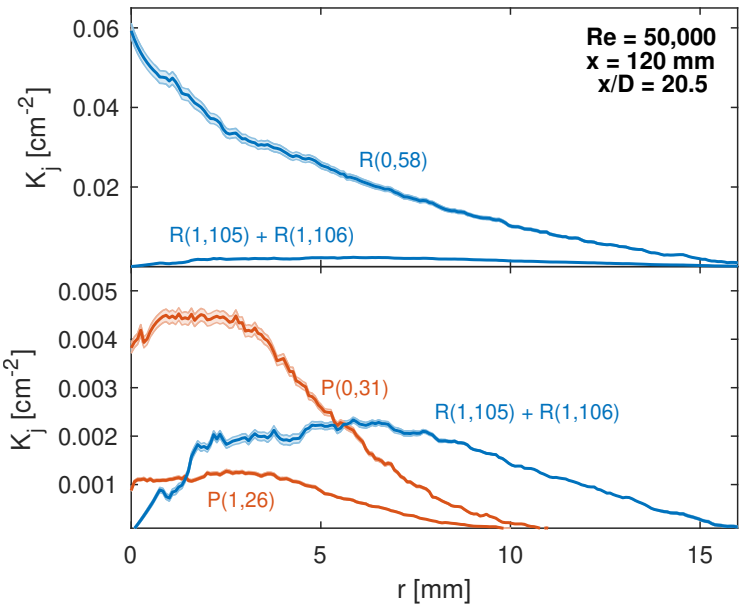

Figure 4.7: Abel-inverted absorption coefficient, $K_j(r)$ for the same lines as in Fig. 4.6 in radial translation space.

in terms of jet diameter D; radial distance is plotted as r/D and axial distance is plotted as x/D.

4.4.1 Mole fraction results

The radial profiles of mole fractions for CO_2 and CO are shown for two different heights above the jet exit for the two different turbulent flow conditions in Fig. 4.8. For the lower plane of 40 mm ($x/D = 6.85$) in the Re = 50,000 case, the absorbance in the R(1,105) + R(1,106) doublet line—which is typically only observed above ~1000 K due to the high lower-state energy—was too weak to independently determine the temperature of the local CO_2 molecules. In this case, the CO temperature (and associated uncertainty in temperature) was assumed to calculate mole fraction for both species.

At the lower height of 40 mm ($x/D = 6.85$), CO and CO_2 are concentrated at a radial distance corresponding to the diameter of the jet D for both turbulent flow conditions. At the higher plane of 120 mm ($x/D = 20.5$), both the CO and the CO_2 diffuse in both the

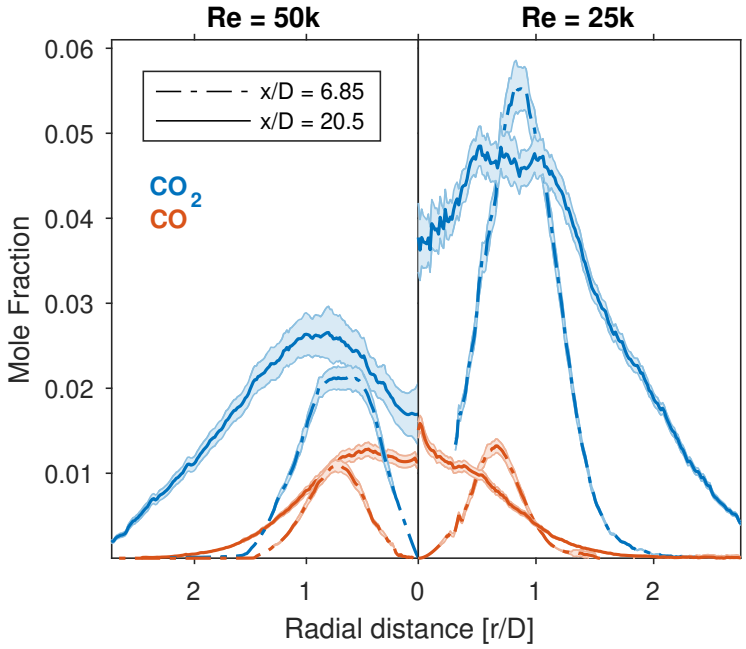

Figure 4.8: Radial profiles of CO_2 and CO mole fraction calculated from Abel-inverted absorption coefficients for Re = 50,000 (left) and 25,000 (right). Dashed-dotted lines indicate $x = 40$ mm ($x/D = 6.85$), solid lines indicate $x = 120$ mm ($x/D = 20.5$). Shaded regions indicate uncertainty.

positive and negative radial directions. However, while the overall mole fractions of CO are similar at the chosen heights, the CO_2 mole fractions are much higher for the case in which the Reynolds number is 25,000 than for the case in which it is 50,000. This could either indicate greater entrainment of the outer co-flow, or more likely less complete oxidation of the fuel associated with the higher jet velocity (at higher Re) and finite rate kinetics. The temperature results that follow—along with the two dimensional images—support the latter. For both species, typical mole fraction uncertainty is ±6%.

4.4.2 Temperature results

The radial profiles of temperatures for CO_2 and CO are shown for the same distinct heights above the jet exit for the two different turbulent flow conditions in Figs. 4.9 and 4.10. As previously mentioned, for the lower plane of 40 mm (x/D = 6.85) in the Re = 50,000 case, the absorbance in the R(1,105) + R(1,106) doublet line was too weak to independently determine the temperature of the local CO_2 molecules and so this is not shown. Additionally, the regions in which the concentrations of CO_2 and/or CO were too low to reliably determine temperature are also not plotted.

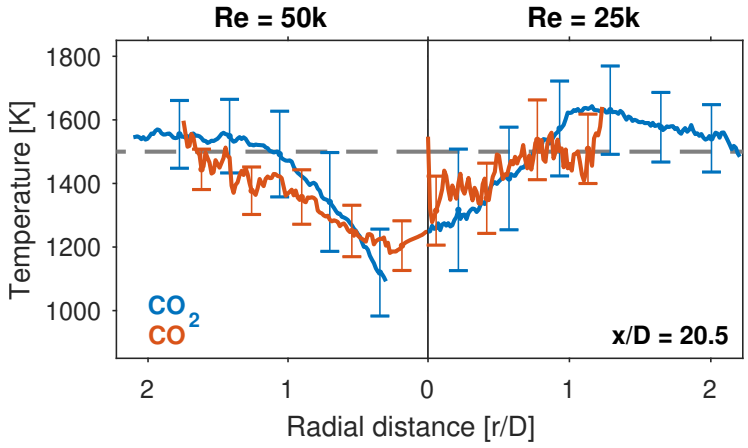

Figure 4.9: Radial profiles of CO_2 and CO temperature calculated from Abel-inverted absorption coefficients for Re = 50,000 (left) and 25,000 (right) at x = 120 mm. Gray dashed lines indicate H_2/air co-flow temperature of 1500 K.

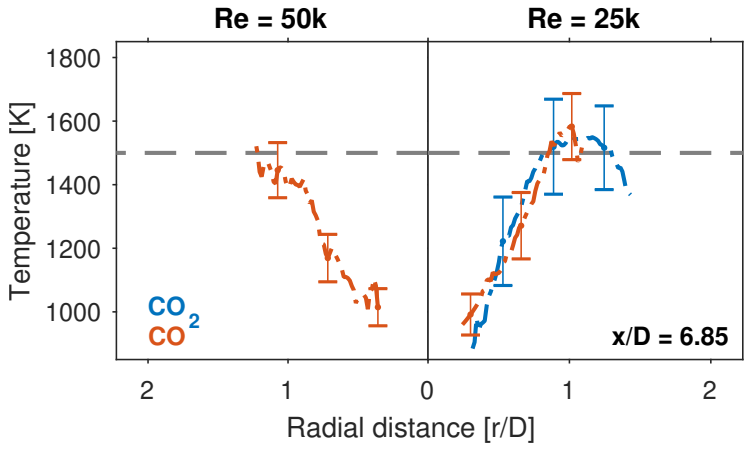

Figure 4.10: Radial profiles of CO_2 and CO temperature calculated from Abel-inverted absorption coefficients for Re = 50,000 (left) and 25,000 (right) at $x = 40$ mm. Gray dashed lines indicate H_2/air co-flow temperature of 1500 K.

The temperature results from regions in which both CO_2 and CO are present in the flow show good agreement within experimental uncertainty. At the higher plane of $x = 120$ mm ($x/D = 20.5$) shown in Fig. 4.9, the species in the core flow have a high enough temperature and concentration for reliable temperature measurements. The radial temperatures appear generally lower for the Re = 50,000 case than they are for the Re = 25,000 case. For the lower plane of $x = 40$ mm ($x/D = 6.85$) shown in Fig. 4.10, the difference is less clear due to the absence of high-temperature CO_2 in the Re = 50,000 case. However, this is consistent with a lesser degree of oxidation for this plane in the Re = 50,000 case. In all cases, the temperature of the molecules approaches that of the H_2/air co-flow (1500 K) as r/D increases. For the profiles shown here, typical CO temperature uncertainty is approximately ±80 K, while the uncertainty for CO_2 temperature is higher around ±130 K. Appendix A provides greater detail on uncertainty analysis.

4.4.3 Two dimensional thermochemistry

In this section, we assemble the results for all planes into two-dimensional images of mole fraction and temperature for CO and CO_2 in Figs. 4.11 through 4.14 to reveal more about

the thermochemical structure of these flames than is possible with one-dimensional radial profiles.

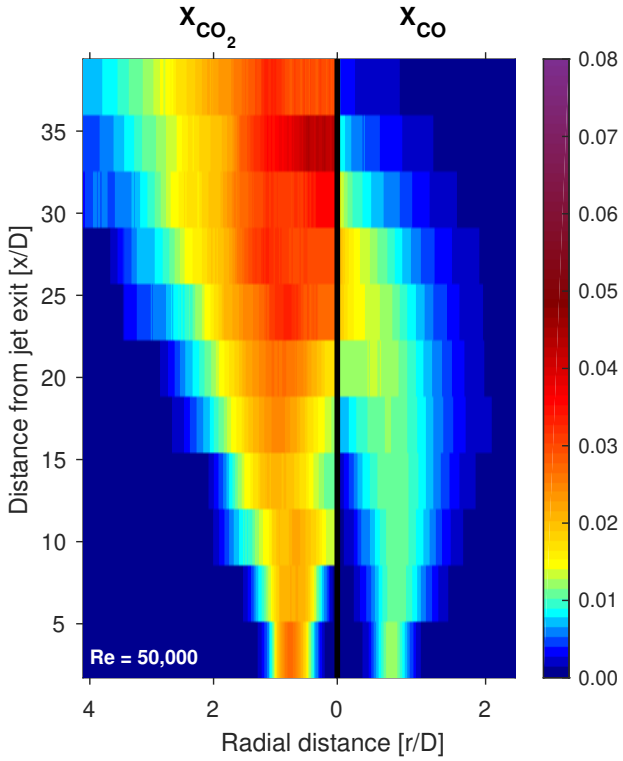

Figure 4.11: Reconstructed two-dimensional mole fraction profile for species CO_2 (left) and CO (right) as a function of r/D and x/D on a C_2H_4/air jet flame. Re = 50,000.

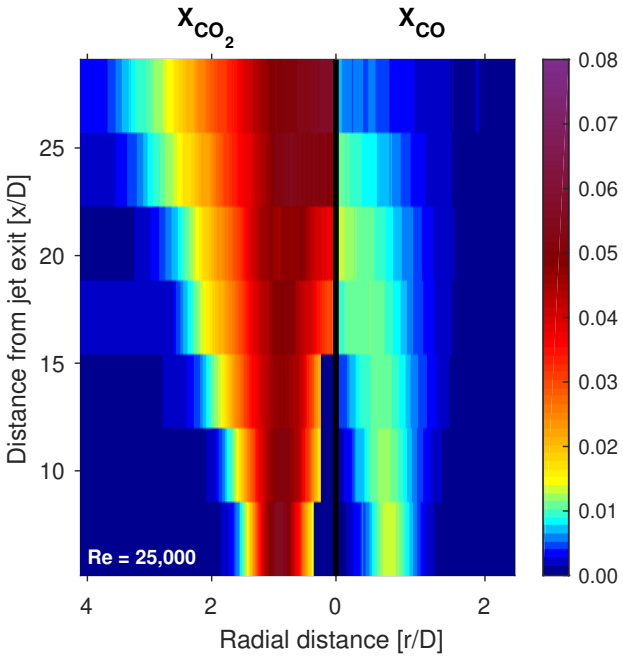

Figure 4.12: Reconstructed mole fraction profile for species CO_2 (left) and CO (right) on a C_2H_4/air jet flame. Re = 25,000.

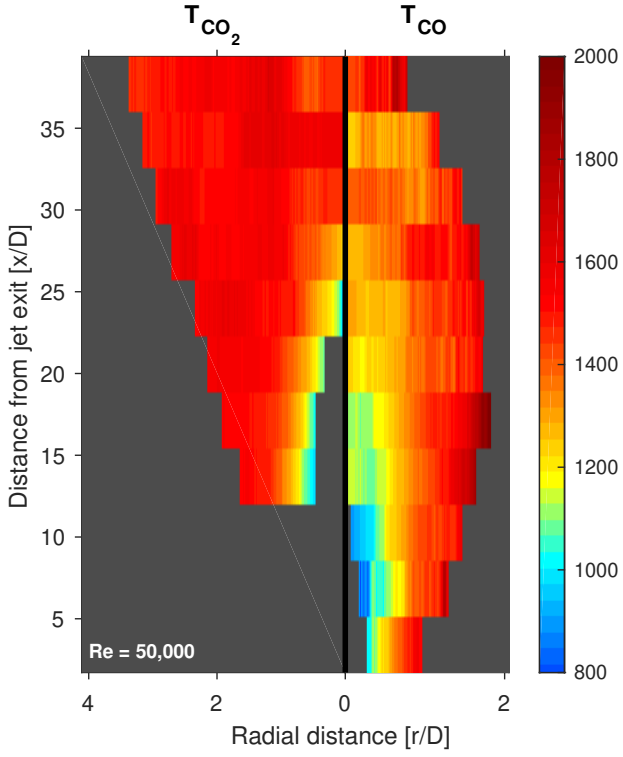

Figure 4.13: Reconstructed two-dimensional temperature (in Kelvin) profile for CO_2 (left) and CO (right) as a function of r/D and x/D on a C_2H_4/air jet flame. Re = 50,000.

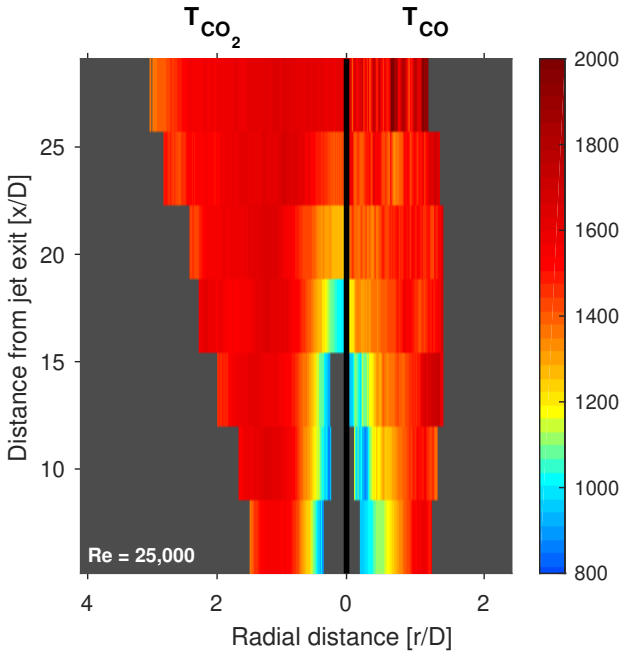

Figure 4.14: Reconstructed temperature profile (Kelvin) for CO_2 (left) and CO (right) on a C_2H_4/air jet flame. Re = 25,000.

In Figs. 4.11 and 4.12, the mole fractions of CO_2 and CO are shown back-to-back. Both figures are plotted with the same mole fraction color scale and so are directly comparable with one another. Similarly, in Figs. 4.13 and 4.14, the temperatures of CO_2 and CO are plotted with the same temperature color scale. In all cases the bounds of the plots are such as to maximize the view of thermochemical CO_2 and CO gradients. We again note that for the lowest three x/D planes shown in the temperature reconstruction in Fig. 4.12, the mole fraction of CO_2 is not measurable in the core flow due to weak absorbance in the R(1,105) + R(1,106) doublet pair in these regions. We also note again that we do not plot temperature in regions where the absorbance of one or more of the targeted spectral lines of a species is too weak (app. SNR < 5) to reliably determine temperature. Additionally, we only plot a subset of the x/D planes for the Re = 25,000 case, and so these plots have fewer vertical planes.

For the mole fraction images in Figs. 4.11 and 4.12, a hollow region in the core of the flame is apparent in both cases in the lower planes (particularly for CO), suggesting that fuel/air

mixture in this region has yet to oxidize to either CO and CO_2. In the Re = 50,000 case, CO concentrations are higher in the upper planes of the flame in the core region, indicating poorer oxidation of the fuel at the tip of the flame than in the Re = 25,000 case. Both CO_2 and CO increase near the center of the jet as x/D increases, though only in the Re = 50,000 case does the CO substantially increase away from the center of the flame, as shown in Fig. 4.11. The overall mole fractions of CO are larger in the Re = 50,000 case in Fig. 4.11 than in the Re = 25,000 case in Fig. 4.12, while the opposite is true for the mole fractions of CO_2. In the Re = 50,000 case, there is higher shear present than in the Re = 25,000 case due to a higher velocity and momentum ratio, resulting in greater entrainment rates with the coflow. This could increase the size of the mixing layer, causing a larger turbulent mass diffusivity as the jet velocity increases and transporting the CO away from the central axis of the flame.

In the temperature images in Figs. 4.13 and 4.14, the temperature is seen to generally be lower near the core of the flame as expected, though exact core temperatures cannot be reliably determined at the lower x/D planes. The temperatures in the Re = 25,000 case are generally higher for given r/D near the core of the flow than they are in the Re = 50,000 case. Along with the CO and CO_2 mole fraction results, this corresponds to more complete oxidation in these regions for the Re = 25,000 case and possibly less entrainment as well.

4.5 Conclusions

Our results demonstrate that mid-infrared laser absorption tomography, probing the fundamental vibrational bands of CO and CO_2, can obtain quantitative, spatially-resolved thermochemical data in small-diameter (sub-cm) turbulent flames. These measurements can be made calibration-free and without knowledge of balance gas composition. Species profiles are fully resolved radially and, with CO and CO_2 in combination, spatially quantify in two dimensions an important terminal reaction in hydrocarbon fuel combustion. Although temperature measurements are only reported for certain regions of the flame (i.e. partially resolved), future analysis may provide expanded measurements since additional lines besides

the R(0,58) and R(1,105) + R(1,106) doublet were accessible with the same laser, as shown in Fig. 4.3.

Both the measurements of mole fraction and temperature as presented in Figs. 4.11 through 4.14 show sensitivity to chemical kinetic progress and turbulent flow conditions (Reynolds number). Accordingly, the sensing strategy presented in this paper may be used to help develop and/or constrain turbulent combustion fluid dynamic models with detailed chemical mechanisms. To the authors' knowledge, these are the first quantitative 2D species measurements of CO and CO_2 in the canonical piloted premixed jet burner.

CHAPTER 5

Application of Mid-IR Laser Absorption Tomography: Examining Fuel Effects on Carbon Oxidation in Turbulent Premixed Jet Flames

The contents of this chapter have been submitted to the journal ***Combustion and Flame*** *under the full title ' Carbon oxidation in turbulent premixed jet flames: a comparative experimental and numerical study of ethylene, n-heptane, and toluene'.*

5.1 Introduction

Turbulent combustion has been the focus of extensive research efforts over the last several decades, with particular attention devoted to the investigation of hydrogen and light hydrocarbon fuels such as methane [98, 99]. Although these studies provide valuable knowledge about highly turbulent flames in the thin and broken reaction zone regimes, relatively few investigations assessed the importance of finite-rate chemistry in the context of fuel specific effects, particularly those caused by the variety of functional groups encountered in practical fuels. Considering that many energy conversion devices rely on turbulent combustion of liquid fuels comprising numerous high molecular weight components, the investigation of fuel effects is of particular importance.

Unlike lighter fuels, heavy hydrocarbons are susceptible to thermal decomposition within the preheat zone of a flame [100–102]. In particular, at high-turbulence intensities, small-scale eddies penetrate the preheat zone and modify its thermal structure [98, 103, 104]. Therefore, for heavy liquid fuels, the local flame structure could exhibit substantially dif-

ferent extinction and propagation behaviors compared to small-hydrocarbon fuels which are resistant to decomposition [105]. These phenomena especially depend on the mixture of smaller molecular fragments created from heavy fuel pyrolysis, which are eventually transported to the reaction zone [106]. Additionally, the diffusivities of heavy fuels and the products of their decomposition are substantially different than those of lighter fuels. Experimental investigations provide evidence that preferential diffusion effects—which could be enhanced for heavy-hydrocarbon fuels—affect the local flame structure and its overall response to hydrodynamics [105, 107, 108].

Recent developments in canonical burner designs, namely, the Hi-Pilot configuration developed by Driscoll and coworkers [109] and the Piloted Premixed Jet Burner (PPJB) developed by Dunn et al. [26, 84], have allowed the study of premixed jet flames in high Reynolds (Re) and Karlovitz (Ka) regimes of turbulence. Investigations with a similar PPJB at USC [86, 87, 110], shown in Fig. 5.1, have examined highly turbulent lean and near-stoichiometric premixed jet flames to explore fuel effects within the thin and broken reaction zones. Carbone et al. [87] captured time-averaged and instantaneous CH* chemiluminescence as well as the behavior of the mean and fluctuating velocity components for a wide range of C_1–C_8 jet flames at Re of 12,500 and 25,000. The authors observed qualitative and quantitative deviation between flames of methane and other liquid fuels, and explored the potential of scaling parameters such as the laminar flame speed (S_L) and the adiabatic flame temperature (T_{ad}) to scale the flame observables. Only S_L showed reasonable success in scaling the flame heights derived from CH* chemiluminescence. Paxton et al. [111] used the PPJB with an ignited coflow to study the effects of heat loss on flames in the broken reaction zones regime. Although the flame heights were shown to scale reasonably well with S_L, the differences between various fuels were not entirely suppressed in the broken reaction zones regime, where heat loss has been found to significantly affect the jet reactivity. These differences become more prominent at higher Re and less pronounced for stronger burning flames.

Evidently, accurate and sufficiently resolved experimental measurements of thermochem-

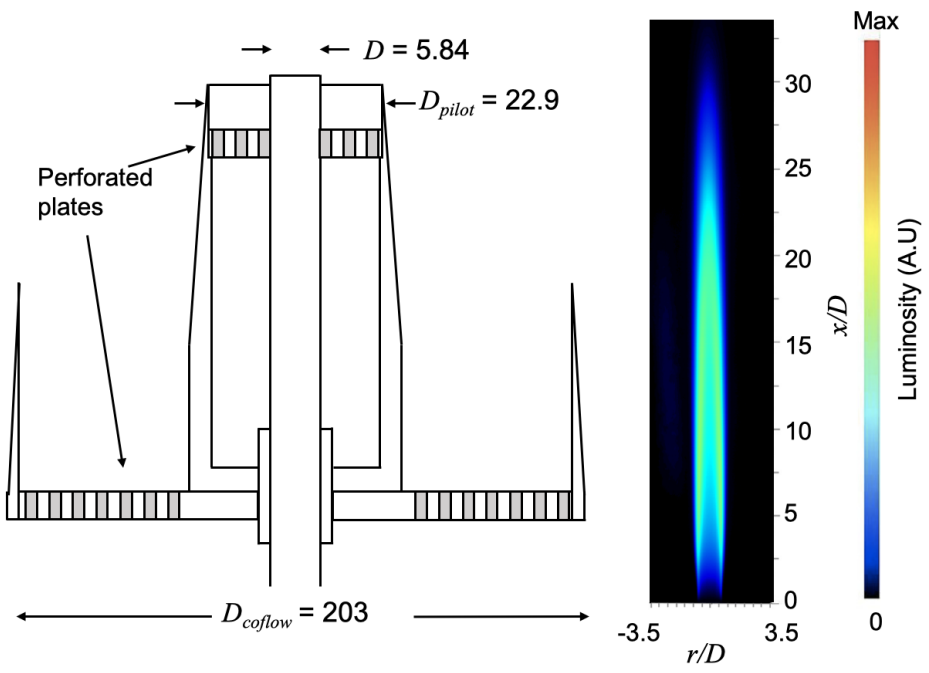

Figure 5.1: Cross-section of the piloted premixed jet burner (PPJB) used for this study along with a chemiluminesence image of a representative flame depicting the radial and axial axes. All measurements are in mm [86].

ical properties in reacting flows help distinguish physical behaviors of different fuels allowing for comparison with high-fidelity models, particularly for high Re and Ka number flames in the thin and broken reaction zones regimes. As such, several non-intrusive optically-based measurement techniques have been utilized to study turbulent flames. These include Rayleigh scattering [26–28, 112], Raman scattering [26, 78, 113], laser-induced fluorescence (LIF) [84, 85] and chemiluminescence [86, 87]. With the exception of Raman scattering, these spectroscopic methods are generally not well-suited for quantitative species detection without extensive calibration. Moreover, relatively weak Raman interactions pose practical difficulties due to the size and power of the required light sources. In contrast, laser absorption spectroscopy (LAS) provides for a calibration-free quantitative method to discern gas properties using compact low-power light sources [2]. Though traditionally limited in non-uniform flows due to the line-of-sight nature of the technique, the integration of tomographic methods has expanded applicability [3]. Recently, laser absorption tomogra-

phy (LAT) was demonstrated to provide two-dimensional temperature and mole fraction measurements of CO and CO_2 in turbulent premixed jet flames using mid-infrared semiconductor lasers [32]. This method—employed in the present work—is suitable for small diameter (∼1 cm) axially-symmetric reacting flows and utilizes tomographic reconstruction techniques [37, 38] to extract time-averaged radial thermochemical profiles from spatially-resolved line-of-sight absorption measurements.

In this study, the thermochemical structure of turbulent jet flames of ethylene, *n*-heptane, and toluene, was experimentally and computationally examined using a piloted premixed jet flame burner. This canonical experimental configuration is widely used for turbulent combustion model validation [84, 86, 113–116]; this represents an opportunity for comparing quantitative LAT measurements with numerical models, specifically large-eddy simulations (LES). The measurements in this study provide spatially-resolved profiles of CO, CO_2, and temperature, targeting regions of carbon oxidation. These carbon oxides are chosen for their roles as critical combustion intermediates and products and their relevance in determining a boundary of heat release associated with the kinetically slow oxidation of CO to CO_2. The novel experimental dataset is accompanied by a series of large-eddy simulations using finite-rate chemistry models to examine the predictive accuracy of current models in capturing fuel effects in these flames.

The remainder of the manuscript has the following structure: The burner configuration, operating conditions, experimental techniques and simulations methods are presented in Sec. 5.2. The results and comparisons between experiments and simulations are discussed in Sec. 5.3. The manuscript concludes with a summary of the major findings.

5.2 Experimental Setup and Methods

5.2.1 Piloted premixed jet burner (PPJB)

For this study, a modified PPJB burner [26] was utilized; the design, dimensions, and fuel delivery system of the burner are described in detail in previous studies [86, 87, 111]. The

burner consists of a central jet tube with a diameter of $D = 5.84$ mm and a pilot and outer co-flow to stabilize the high-velocity central jet. A schematic of the burner configuration is shown in Fig. 5.1 along with a flame image depicting the axial (x) and radial (r) direction. Experiments were performed at a single jet Reynolds number, $Re_{\text{jet}} \equiv U_{\text{jet}} D/\nu = 50{,}000$, where U_{jet} is the bulk flow velocity and ν is the kinematic viscosity at the burner exit. The jet flames were ethylene (C_2H_4)-air, n-heptane (n-C_7H_{16})-air, and toluene ($C_6H_5CH_3$)-air mixtures at lean fuel-air molar equivalence ratios corresponding to $S_L = 20$ cm/s. All flows had an unburned mixture temperature of 298 K.

The pilot flame is a premixed C_2H_4-air flame with a temperature of 1780 K. The coflow surrounds the pilot and jet flames and is used to thermally insulate the jet. The coflow used a premixed hydrogen-air flame at a global equivalence ratio of $\phi = 0.51$ to provide a temperature of $T_{\text{coflow}} = 1500$ K. This co-flow mixture is used to provide boundary conditions largely free of carbon atoms to minimize interference for the LAT technique probing the central jet flame [32]. The coflow and pilot flows had an unburnt velocity of 0.75 m/s. The flame is assumed axisymmetric over the time interval (500 ms) in which LAT measurements (Described in Section 5.2.2) are taken, averaged, and reported in this study.

Table 5.1 provides a summary of the conditions investigated. S_{L} as well as the lamianr flame thickness (δ_f), the flame time (τ_f), and adiabatic flame temperature (T_{ad}) were calculated in PREMIX [117]. The flame height (H_{fl}) was calculated using time-averaged line-of-sight CH* chemiluminescence data. H_{fl} is defined as the position along the centerline of the jet at which the CH* intensity drops to 25% of its maximum value [87]. The turbulent Reynolds number $Re_{\text{t}} \equiv u' L_{\text{int}}/\nu$ where u' is the turbulent intensity measured previously from PIV data [111]. The integral length scale (L_{int}) was calculated at the radial location where u'_{x} reaches its maximum value in the shear layer using the two-point correlations described by Carbone et al [87] such that L_{int}=5.6 $\pm$0.4mm [26]. It should be noted that u' does not depend on ϕ while L_{int} shows a minor dependence on ϕ and fuel type [86, 87]. The Karlovitz number (Ka) is defined as $Ka \equiv \frac{\tau_f}{\tau_\eta}$, where τ_η is the Kolomogorov time scale determined as in previous studies [86, 87]. As characterized by the high u' and Ka, these

Table 5.1: Estimated key turbulence characteristics for the performed experiments. All values were calculated based on the kinematic viscosity of the unburned mixture, but the turbulent properties of the flow L_{int} and u' were measured in the shear layer at x/D=15.

Fuel	ϕ	u_{jet} (m/s)	Re_{jet}	S_{L} (cm/s)	$\frac{u'}{S_{\text{L}}}$	$\frac{L_{\text{int}}}{\delta_f}$	Ka	$Da = \frac{\tau_t}{\tau_f}$	Re_{t}	T_{ad} (K)	H_{fl} (mm)
C_2H_4	0.55	133	50000	20	80	9.41	639	0.117	5483	1706	196
n-C_7H_{16}	0.65	133	50000	20	80	9.81	636	0.118	5483	1804	216
$C_6H_5CH_3$	0.70	133	50000	20	80	9.46	662	0.112	5483	1931	230

flames are expected to fall in the thin reaction zone/regime with broadened preheat layer regime.

5.2.2 Laser absorption tomography

Laser absorption tomography is a spatially-resolved diagnostic technique based on inversion of species-specific absorption projected along a multitude of optical lines-of-sight. LAT is thoroughly detailed in the literature and prior work [3, 32, 39, 40, 42, 118], but we provide a brief overview here for context and nomenclature. For a non-uniform gas medium axially-symmetric in r [cm], the Beer-Lambert law integrated over wavenumber ν [cm^{-1}]—or the projected absorbance area $A_{j,proj}(r)$ [cm^{-1}]—can be expressed for each line-of-sight and related to thermodynamic gas properties as [39]:

$$A_{j,\text{proj}}(r) = \int_{-\infty}^{\infty} -\ln\left(\frac{I_t}{I_0}\right)_{\nu} d\nu = \int_{-\infty}^{\infty} \alpha_\nu d\nu = \int_{0}^{L(r)} K_j(r) dl \tag{5.1}$$

where α_ν is the spectral absorbance, I_0 is incident intensity, and I_t is transmitted intensity. $L(r)$ [cm] is the aggregate path length at radial position r. Integrating specific transitions in the spectral domain eliminates dependence on line-shape and composition. The thermo-chemical properties of interest are embedded in the radially-resolved absorption coefficient $K_j(r)$ [cm^{-2}] [32],

$$K_j(r) = PS_j(T(r))X_{\text{abs}}(r) \tag{5.2}$$

where the total pressure P [atm] is assumed constant (1 atm), $S_j(T(r))$ [cm^{-2}/atm] is the linestrength of transition j at temperature $T(r)$ [K], and $X_{\text{abs}}(r)$ is the mole fraction of the absorbing species. To obtain the radial distribution of $K_j(r)$ [cm^{-2}], a Tikhonov-regularized Abel inversion scheme [32, 37, 38] is implemented on $A_{j,\text{proj}}(r)$ measurements with regularization parameters determined by the L-curve method [119]. For multiple spectral transitions j, multiple $K_j(r)$ can be determined, and the ratio of two absorption coefficients reduces to a ratio of $S_j(r)$, which is a function of $T(r)$ only, as shown in Eq. 5.3.

$$R(r) = \frac{K_A(r)}{K_B(r)} = \frac{S_A(T(r))}{S_B(T(r))} = f(T(r)) \tag{5.3}$$

$S_j(T)$ can be calculated using information readily available in spectral databases (See A), so gas temperature $T(r)$ can be determined with the simultaneous measure of two transitions at any location r [32, 39]. Once temperature is known, mole fraction $X_{\text{abs}}(r)$ can be directly calculated from measured $K_j(r)$ of either transition through Eq. 5.2. In this study, we implement this strategy at multiple measurement planes of a turbulent jet flame to construct two-dimensional images of temperature and gas composition [32].

A scanned-wavelength direct-absorption method was employed with a tunable quantum cascade laser (QCL) and a tunable interband cascade laser (ICL) to spectrally resolve select ro-vibrational transitions in the fundamental vibrational bands of CO and CO_2 near 4.9 and 4.2 μm, respectively. The compact lasers and detectors were mounted to a 150×150 mm^2 optical breadboard fixed to a dual horizontal and vertical translation stage as shown in Fig. 5.2, to characterize the time-averaged thermochemical structure of the flames. The concentric laser beams were focused to beam diameters of ∼0.5 mm. During the measurement, the optomechanical assembly translates horizontally via an automatic translation stage, and the encoder signals of its stepper motor are used to resolve the spatial location of the measurements in time. A manual vertical stage translates the entire assembly to repeat the measurements at different heights downstream of the jet exit. Overall, the spatial resolution in the radial direction was 0.5 mm and the resolution in the vertical direction was 20 mm. Since the thermochemical gradients in the flames are much lower in the vertical direction than the in the radial direction, a sparse vertical resolution was deemed acceptable for the

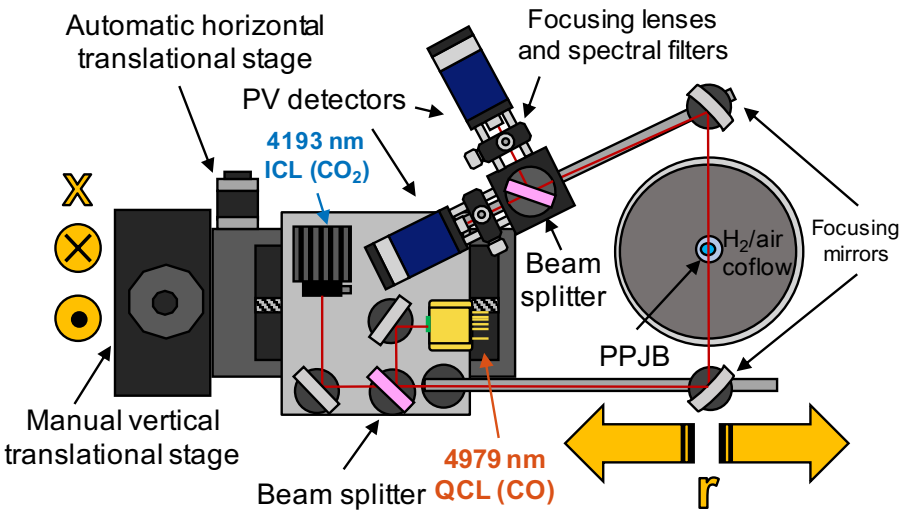

Figure 5.2: Top-down schematic of PPJB facility with optomechanical translation stage system. The central jet is surrounded by a co-flow H_2/air flame. The lasers, optics, and detectors are mounted and move together while the burner remains stationary.

purposes of this comparative study.

It is important to note that two ro-vibrational transitions must be sufficiently resolved for any given species to determine gas temperature and subsequently mole fraction. For each species, two ro-vibrational transitions $B(v'', J'')$, are targeted, where B indicates the branch (R, P, or Q), while v'' and J'' indicate the lower-state vibration and rotation quantum numbers, respectively [1]. We target the P(0,31) and P(1,26) lines of CO and the R(0,58) line and R(1,105+106) doublet line of CO_2 [32]. Although the reconstructions of $K_j(r)$ are valid within their uncertainties for all r, regions of the flow with very low absorption coefficient (signal-to-noise ratio < 5) are less reliable for quantitative interpretation and are not plotted. For the targeted wavelengths in this study, this typically corresponds to regions of the flow that are either much below ~1000 K or with a mole fraction less than $\sim 5 \cdot 10^{-4}$. Further details regarding the measurement uncertainty are available in A, while more information about the wavelength selection and temperature sensitivity is available in previous work [32].

5.2.3 Large-Eddy Simulations

The measurements are complimented by large-eddy simulations. For this, a finite-rate combustion model using reduced chemical models is utilized for the simulation of all three fuels. The turbulent reacting flow field is described as solution to Favre-filtered conservation equations for mass, momentum, total energy, and species, taking the following form:

$$\partial_t \overline{\rho} + \nabla \cdot (\overline{\rho}\widetilde{\boldsymbol{u}}) = 0\,, \tag{5.4a}$$

$$\partial_t (\overline{\rho}\widetilde{\boldsymbol{u}}) + \nabla \cdot (\overline{\rho}\widetilde{\boldsymbol{u}}\widetilde{\boldsymbol{u}}) = -\nabla \overline{p} + \nabla \cdot \overline{\boldsymbol{\tau}}_{v+t}\,, \tag{5.4b}$$

$$\partial_t (\overline{\rho}\widetilde{e}) + \nabla \cdot (\overline{\rho}\widetilde{\boldsymbol{u}}\widetilde{e}) = -\nabla \cdot (\widetilde{\boldsymbol{u}}\overline{p}) + \nabla \cdot (\overline{\boldsymbol{\tau}}_v \cdot \widetilde{\boldsymbol{u}}) - \nabla \cdot \overline{\boldsymbol{q}}_{v+t}\,, \tag{5.4c}$$

$$\partial_t (\overline{\rho}\widetilde{Y_k}) + \nabla \cdot (\overline{\rho}\widetilde{\boldsymbol{u}}\widetilde{Y_k}) = -\nabla \cdot \overline{\boldsymbol{j}}_{k,\,v+t} + \overline{\dot{\omega}}_k\,, \tag{5.4d}$$

where ρ is the density, $\boldsymbol{u}$ is the velocity vector, p is the pressure, e is the specific total energy, $\boldsymbol{\tau}$ is the stress tensor, $\boldsymbol{q}$ is the heat flux, and Y_k, $\boldsymbol{j}_k$, and $\dot{\omega}_k$ are the mass fraction, diffusion flux, and chemical source term for species k, and the species equations are solved for $k = 1, \ldots, N_S - 1$ where N_S is the number of species. Subscripts v and t denote viscous and turbulent quantities, respectively.

For the subgrid-scale turbulence-chemistry interaction, the dynamic thickened-flame model [120] is employed, and the Vreman model [121] is used to represent the turbulent subgrid stresses. A sensitivity study was performed and a maximal thickening factor of 3 was found to be adequate for the current choice of mesh resolution. The source term of CO is used as a sensor—the maximum net production rate of CO in a free flame simulation corresponding to each fuel is used as the activation threshold.

The equations for mass, momentum, energy, and species are discretized using a finite-volume formulation with a sensor-based hybrid scheme for the convective flux [122, 123]. In this hybrid method, a high-order central scheme is combined with a second-order essentially non-oscillatory scheme. A second-order Strang-splitting scheme [124] is applied to separate the convection, diffusion, and reaction operators. A strong stability preserving 3rd-order Runge-Kutta (SSP-RK3) scheme [125] is used for time integration of non-stiff operators. The reaction chemistry is integrated using a semi-implicit Rosenbrock-Krylov scheme [126],

which is 4th-order accurate in time and has linear cost with respect to the number of species.

All chemical kinetic mechanisms employed in these simulations are DRG reduced [127] and validated against calculations [128] of 1D laminar flames with S_L, temperature profiles, and major species profiles as reduction targets. For C_2H_4, a DRG reduced model based on USC Mech II [129] was used. For both n-C_7H_{16} and $C_6H_5CH_3$, reduced-order models are based on JetSurF 2.0 [130]. Due to solution stiffness, the n-C_7H_{16} and $C_6H_5CH_3$ models were modified by removing several of the smallest timescale reactions.

The size of the three-dimensional computational domain is 0.35 m $\times$ 0.26 m $\times$ 2π in the axial, radial, and azimuthal directions, respectively. The grid uses 401 non-uniformly distributed points in axial direction, concentrated in the vicinity of the injection plane to ensure sufficient resolution of the turbulent scales. The radial direction is discretized with 125 points, clustered in the shear layers between the different streams, whereas 160 points are used for the circumferential resolution. At the inlet of the jet stream, a turbulent velocity profile is applied, with turbulent fluctuations prescribed to match the experimentally measured velocity field. For the co-flow and pilot streams, the velocity corresponding to the burnt products along with the adiabatic chemical equilibrium temperature and composition is prescribed.

The LES computations provide spatially-resolved instantaneous thermochemical properties (temperature, mole fractions, reaction rates) for the different flames under investigation. Representative instantaneous flow-fields for CO and CO_2 obtained from these simulations for the three different fuels are shown in Fig. 5.3. Fuel-specific effects are immediately notable from the instantaneous images; regions of the flows exhibit local CO and CO_2 mole fraction levels which are highest for the (C_2H_4)-air flame, next-highest for the (n-C_7H_{16})-air flame, and lowest for the ($C_6H_5CH_3$)-air flame. For adequate comparison with the experimental laser absorption tomography measurements—which represent time- and azimuthally-averaged thermochemistry—the simulations are run for five convective flow-through times and statistical flow-field results are obtained by averaging both in time and about the azimuthal direction.

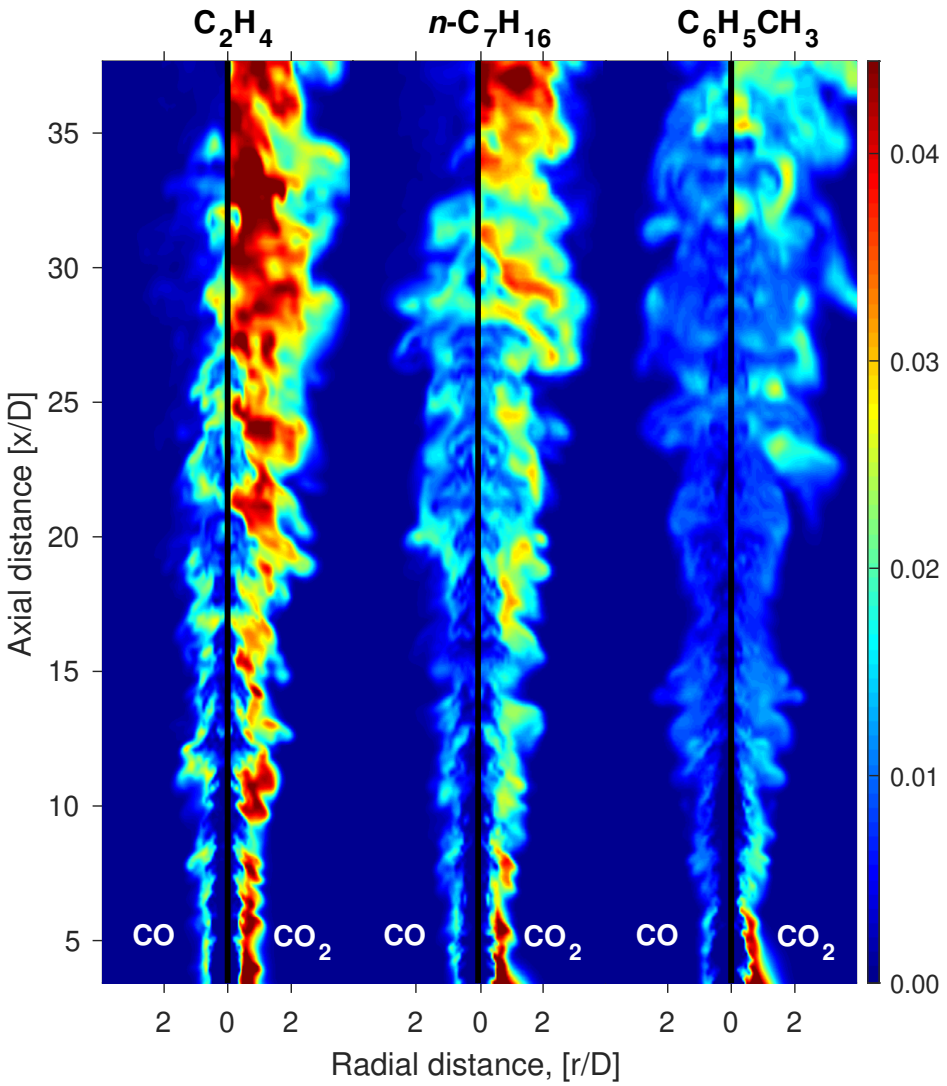

Figure 5.3: Instantaneous (non-time-averaged) LES predictions of CO and CO_2 mole fraction for the flame conditions shown in Table 5.1.

5.3 Results and Discussion

5.3.1 Comparative two-dimensional thermochemistry

Experimental and numerical results from all planes are assembled into two-dimensional images of mole fraction for CO and CO_2 in Figs. 5.4 and 5.5 to distinguish and compare the thermochemical structure amongst the different fuels.

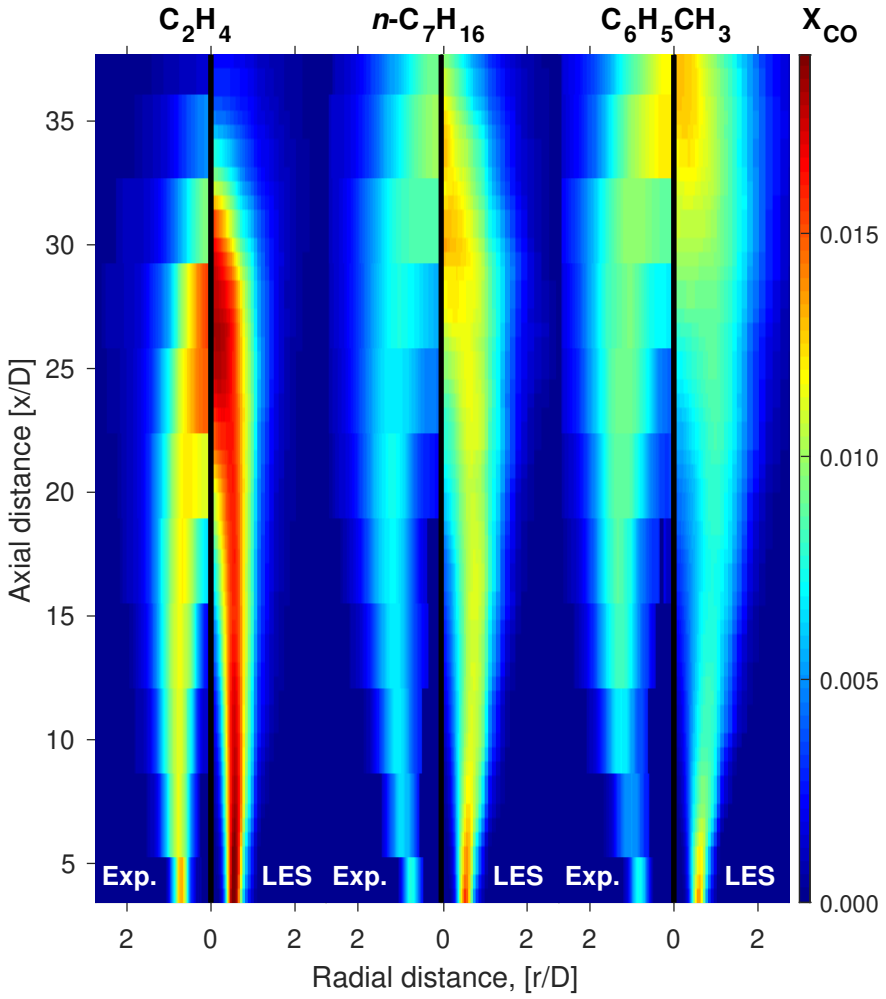

Figure 5.4: Two-dimensional CO mole fraction for each fuel from both experimental results (left sides) and LES predictions (right sides).

For the CO mole fraction images shown in Fig. 5.4, a hollow region in the core of the jet flame is apparent for all fuels studied, and this region is longer for the (n-C_7H_{16})-air and

($C_6H_5CH_3$)-air jet flames. This indicates that n-C_7H_{16} and $C_6H_5CH_3$ in their corresponding flames take longer to initiate carbon oxidation. These hollow regions appear larger in the measurements than in the LES predictions, especially in the (n-C_7H_{16})-air flame. The measured and LES-predicted peak locations of CO are in good agreement throughout the flames, although less CO is observed in the experiments than predicted for the (C_2H_4)-air and (n-C_7H_{16})-air flames.

More information is gleaned from looking at the CO_2 mole fraction image in Fig. 5.5. We note that for the lowest vertical planes, the mole fraction of CO_2 is not experimentally

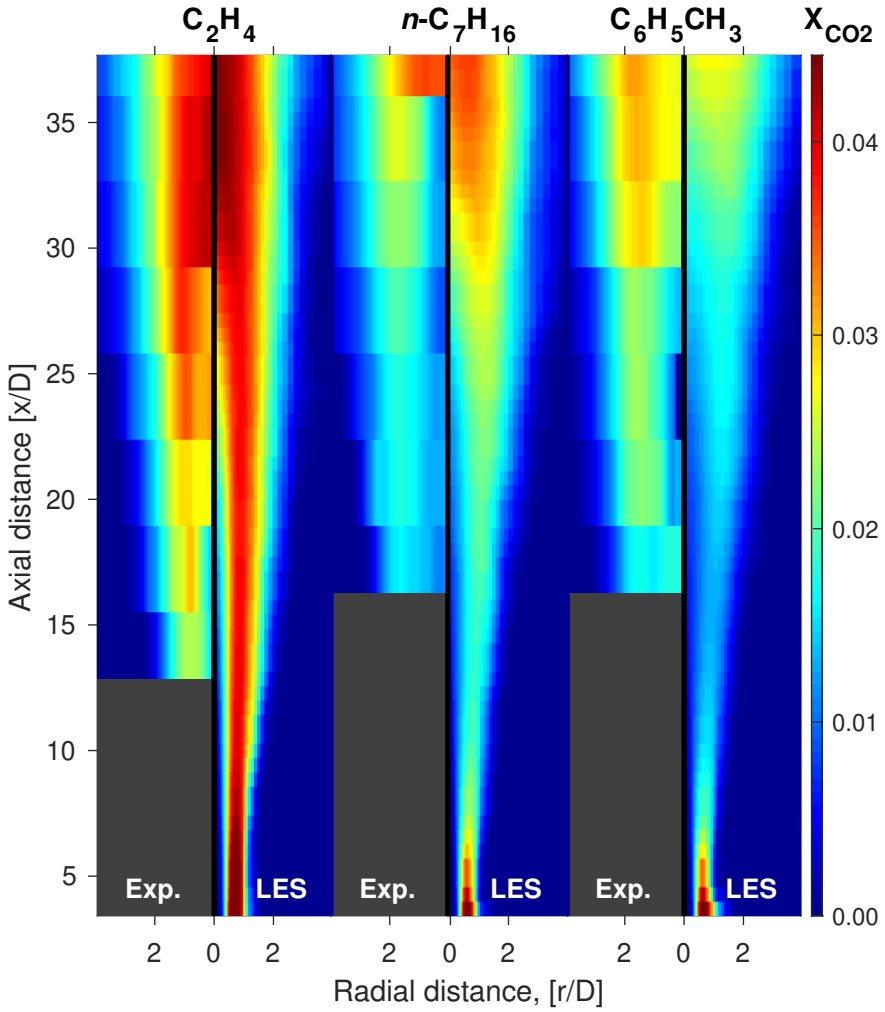

Figure 5.5: Two-dimensional CO_2 mole fraction for each fuel from both experimental results (left sides) and LES predictions (right sides).

resolvable in the flow due to weak absorbance in the R(1,105+106) doublet pair in these regions. CO_2 forms most appreciably near the core regions of the flames at locations of x/D beyond which the mole fraction of CO has begun to decrease in the axial direction, consistent with continued carbon oxidation in the flame. The trends in experimental CO_2 mole fraction profiles amongst the fuels are well-captured by the LES predictions, with both (n-C_7H_{16})-air and ($C_6H_5CH_3$)-air flames forming CO_2 most appreciably at larger x/D than the (C_2H_4)-air flame. For the (n-C_7H_{16})-air flame, experimentally measured CO_2 mole fraction is observed to increase in the core of the flame suddenly in the highest x/D plane measured, resembling the corresponding CO_2 image from the instantaneous LES predictions shown in Fig. 5.3, while the averaged LES predictions show a more gradual increase. Conversely, in the ($C_6H_5CH_3$)-air flame, the concentration of CO_2 in the core of the flame is generally underpredicted.

Although all tested fuels in their respective equivalence ratios have the same S_u, the thermochemical structures of the flames are distinguished from one another readily, highlighting the effects of fuel chemistry in turbulent jet flames. As with the instantaneous LES predictions shown in Fig. 5.3, the measurements and averaged LES predictions of the (C_2H_4)-air flame show the highest concentrations of both CO and CO_2, although the ordering is less immediately apparent with regards to the (n-C_7H_{16})-air flame and ($C_6H_5CH_3$)-air flame. The alkene C_2H_4 provides a shorter flame than the normal alkane n-C_7H_{16} and the aromatic $C_6H_5CH_3$, which have wider flame brushes and a wider and taller core region without CO or CO_2, indicating slower overall oxidation and increased diffusion of fuel or fuel fragments in the flame.

5.3.2 Single plane analysis

To better characterize the agreements and disagreements between the LES predictions and experimental measurements while considering experimental uncertainties, radial profiles obtained for specific x/D planes above the burner are examined in more detail. Details regarding the calculation of measurement uncertainties can be found in A. Representative radial profiles of mole fractions for CO and CO_2 are shown for two different heights above the

jet exit for the ethylene-air jet flame in Fig. 5.6. For the lower plane shown of 100 mm

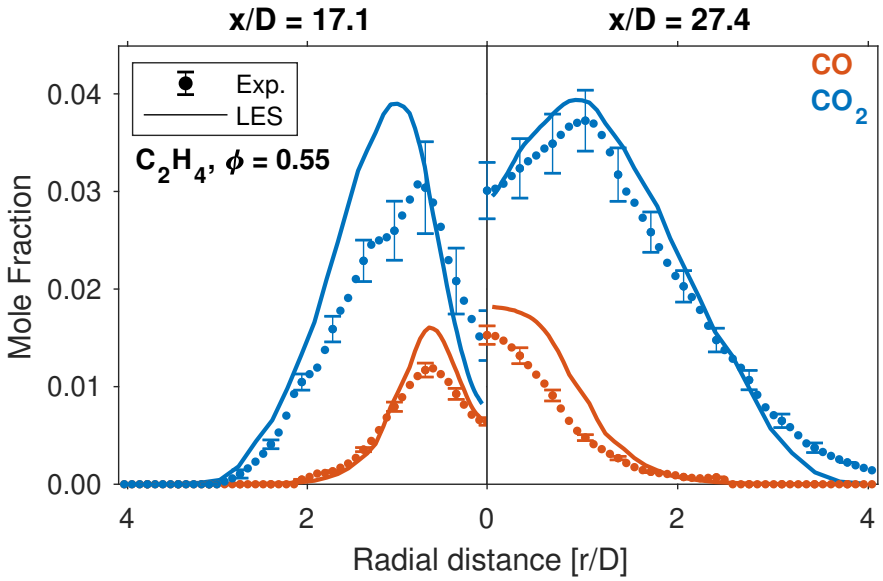

Figure 5.6: Radial profiles of CO and CO_2 mole fraction obtained from LAT measurements alongside predicted results from simulations.

($x/D = 17.1$), CO and CO_2 are concentrated at a radial distance within two jet diameters, with CO concentrated closer to D. Notably, there is a lower concentration of both CO and CO_2 in the core of the flame. For the higher plane measured at 160 mm ($x/D = 27.4$), CO and CO_2 are more concentrated at the core of the flow, with peak CO mole fraction occurring at the centerline. CO_2 is formed toward larger r/D. For both planes, there is much more CO_2 than CO, indicating relatively fast oxidation of CO to CO_2 as it is formed. The averaged LES prediction captures the spatial extent of both species, despite nominally over-predicting peak concentrations in the lower plane.

Representative radial profiles of temperatures determined from both CO and CO_2 laser absorption tomography measurements are similarly shown for the same planes of the same (C_2H_4)-air jet flame in Fig. 5.7. The LAT temperature results from regions in which both CO and CO_2 are present in the flow generally show good agreement within experimental uncertainty, although regions of the flow with low species concentration have greater uncertainty due to lower spectral absorbance [32]. At the lower plane of 100 mm ($x/D = 17.1$), the

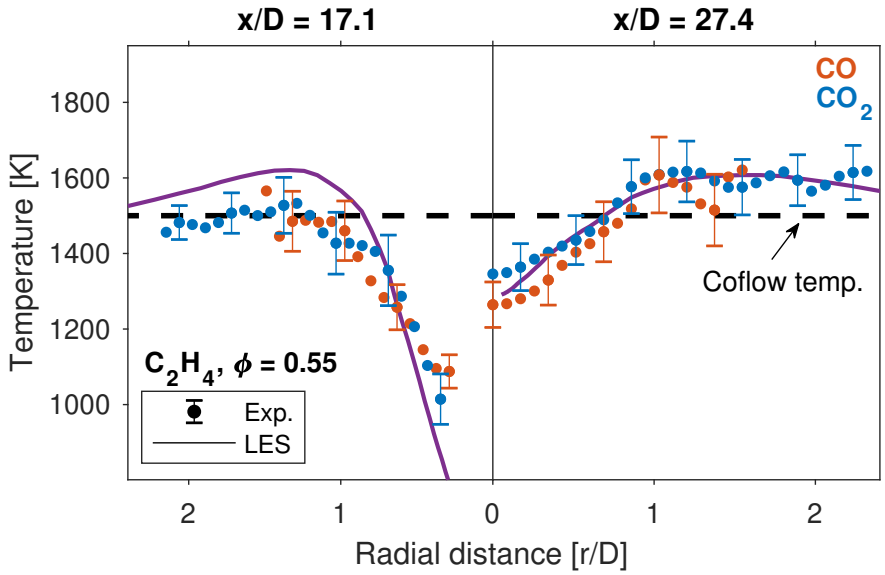

Figure 5.7: Temperature profiles obtained from CO and CO_2 LAT measurements and corresponding simulation predictions. The co-flow temperature is indicated with a dashed black line.

temperature increases toward the co-flow temperature of 1500 K. The core of the flow has a much lower temperature, just above 1000 K. At the higher plane of 160 mm ($x/D = 27.4$), the measured temperature peaks near approximately the jet diameter ($r/D \approx 1$), although the average LES predicted temperature is nominally higher. The core of the flow has a higher temperature ($T \approx 1300$ K) than in the lower plane, which is still lower than the coflow temperature of 1500 K. The averaged LES model accurately predicts the radial temperature distribution within experimental uncertainty for both planes, although in the lower plane ($x/D = 17.1$) the simulation nominally over-predicts the gas temperature. The averaged simulation results are consistent with the mole fraction results shown in Fig. 5.6, which shows an overprediction of oxidation rate closer to the jet exit.

Additional representative radial profiles of CO and CO_2 mole fractions are shown for the n-heptane-air jet flame in Fig. 5.8. For the lower plane of 100 mm ($x/D = 17.1$), CO and CO_2 are concentrated largely within two jet diameters, as with the (C_2H_4)-air jet flame. In contrast, the overall concentrations (measured and predicted) of both species are much lower than in the (C_2H_4)-air jet flame for $x/D = 17.1$. The radial extent of both species

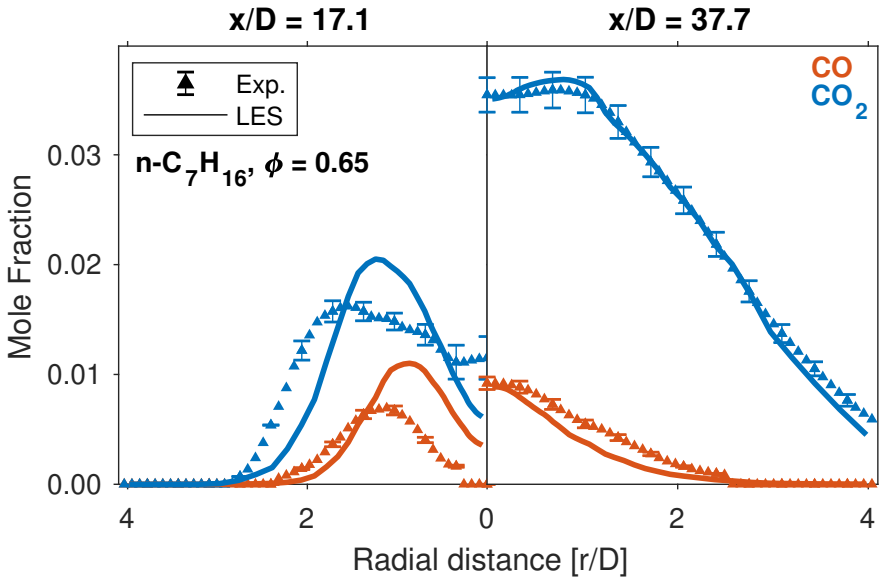

Figure 5.8: Radial profiles of CO and CO_2 mole fraction obtained from LAT measurements alongside predicted results from simulations.

is larger than predicted by the LES modeling, and the peak values are over-predicted. For the higher plane shown of 220 mm ($x/D = 37.7$), the averaged LES predictions are in much better agreement with experimental observations; the peak concentrations of CO and CO_2 agree within experimental uncertainty, though a slight underprediction of CO concentration is noted at larger r/D.

Representative radial profiles of CO and CO_2 mole fractions are shown for the toluene-air jet flame in Fig. 5.9. The toluene-air jet flame is generally observed to have a wider flame brush than the other flames, indicated by the larger radial spread of both CO and CO_2. For the lower plane of 120 mm ($x/D = 20.5$) shown, CO and CO_2 mole fractions are lower in the core of the flame, and peak near approximately the jet diameter ($r/D \approx 1$). Experimental uncertainty for CO_2 mole fraction is larger in this core region, owing to significant variation in both CO_2 absorption coefficients $K_{R(0,58)}$ and $K_{R(1,105+106)}$ in the core of the flow at the lower planes for this jet flame. The averaged LES predictions for CO generally agree within experimental uncertainty in both planes shown, while CO_2 is underpredicted. For the higher plane of 160 mm ($x/D = 27.4$), the distribution of CO and CO_2 increases slightly to larger

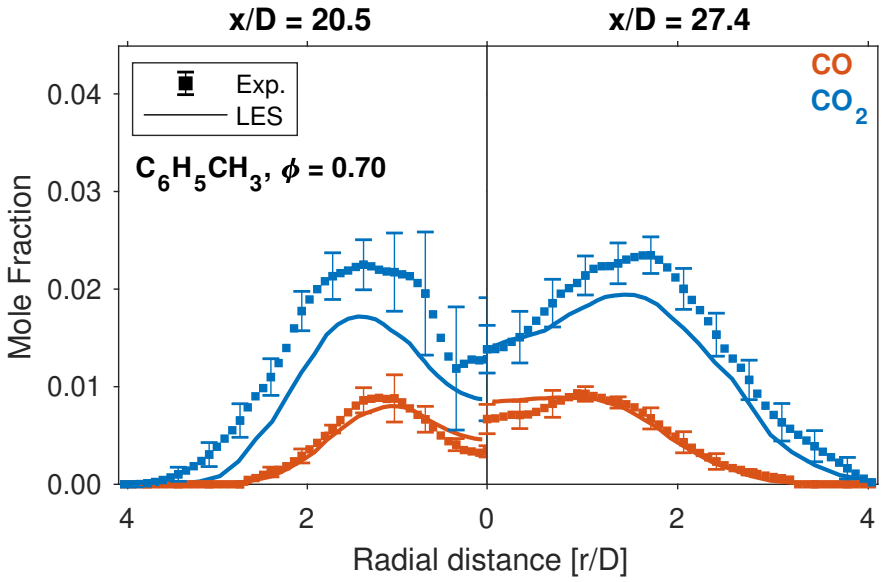

Figure 5.9: Radial profiles of CO and CO_2 mole fraction obtained from LAT measurements alongside predicted results from simulations.

r/D, and the experimental uncertainties are smaller relative to those in the lower plane. Despite nominally underpredicting the CO_2 mole fraction, the averaged LES predictions capture the shapes of the profiles well.

Notable fuel-specific trends predicted by LES are observed in the experimental measurements. The top of Fig. 5.10 shows experimental and computational radial profiles of CO and CO_2 mole fraction at a significantly downstream location ($x/D = 34.2$). The averaged LES predictions of peak CO mole fraction are all nominally in agreement with the experimental measurements, with the exception of those of the (n-C_7H_{16})-air flame. With that exception, the fuel ordering in peak CO and CO_2 concentration and behavior with increasing radial direction amongst the fuels are in agreement. The (C_2H_4)-air flame has the highest peak levels of CO of the fuels, and the steeper gradients in concentration indicate a thinner reaction zone with more rapid oxidation than the other fuel-air mixtures in these conditions, which is observed in Figs. 5.4 and 5.5. The bottom of Fig. 5.10 shows a similar plot for CO_2 mole fraction. For CO_2 mole fraction, the averaged LES predictions and experimental measurements are in better agreement for both the (C_2H_4)-air and ($C_6H_5CH_3$)-air flames,

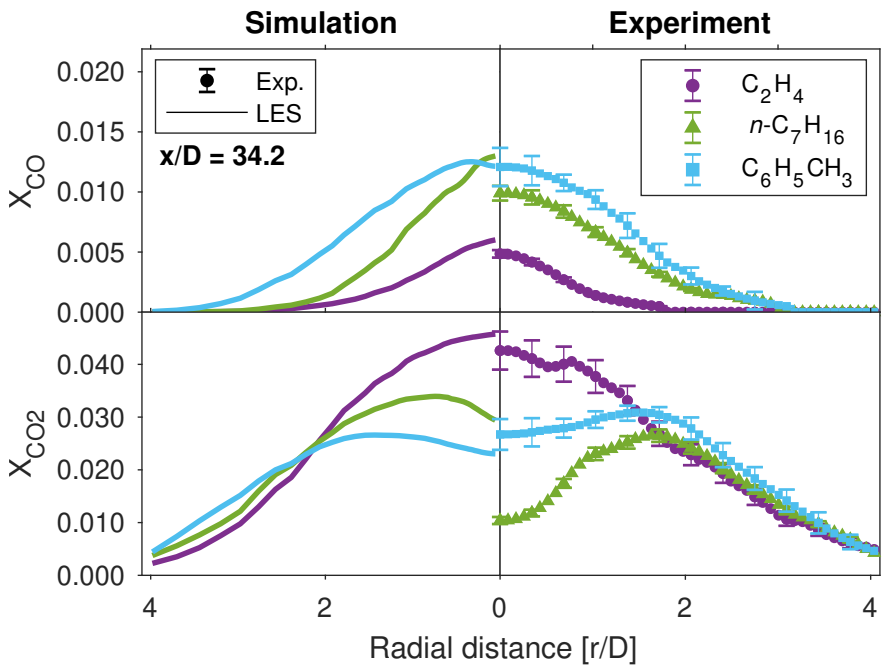

Figure 5.10: Comparative computational (left) and experimental (right) radial profiles of CO and CO_2 mole fractions at $x/D = 34.2$.

both nominally and qualitatively. However, the results show more disagreement for the flame fueled by the alkane n-C_7H_{16}. Specifically, the reaction zone of the (n-C_7H_{16})-air flame is concentrated near $r/D = 2$ rather than closer to the centerline. Both results suggest that the n-C_7H_{16} in the flame is oxidizing at a lower rate than predicted by the averaged simulations, providing for a taller flame.

5.3.3 Thermochemical state-space analysis

An analysis of the thermochemical state-space representation of the experimental and numerical results is conducted by examining correlations between X_{CO}, X_{CO_2} and temperature. Figure 5.11 compares instantaneous and averaged scatter data from the LES calculations of the three different flames with measurements. These scatter data are extracted along three axial planes for $x/D = \{15, 25, 35\}$. In general, it can be seen that major differences are confined to the upstream region of the flames that are represented by strong turbulence/-

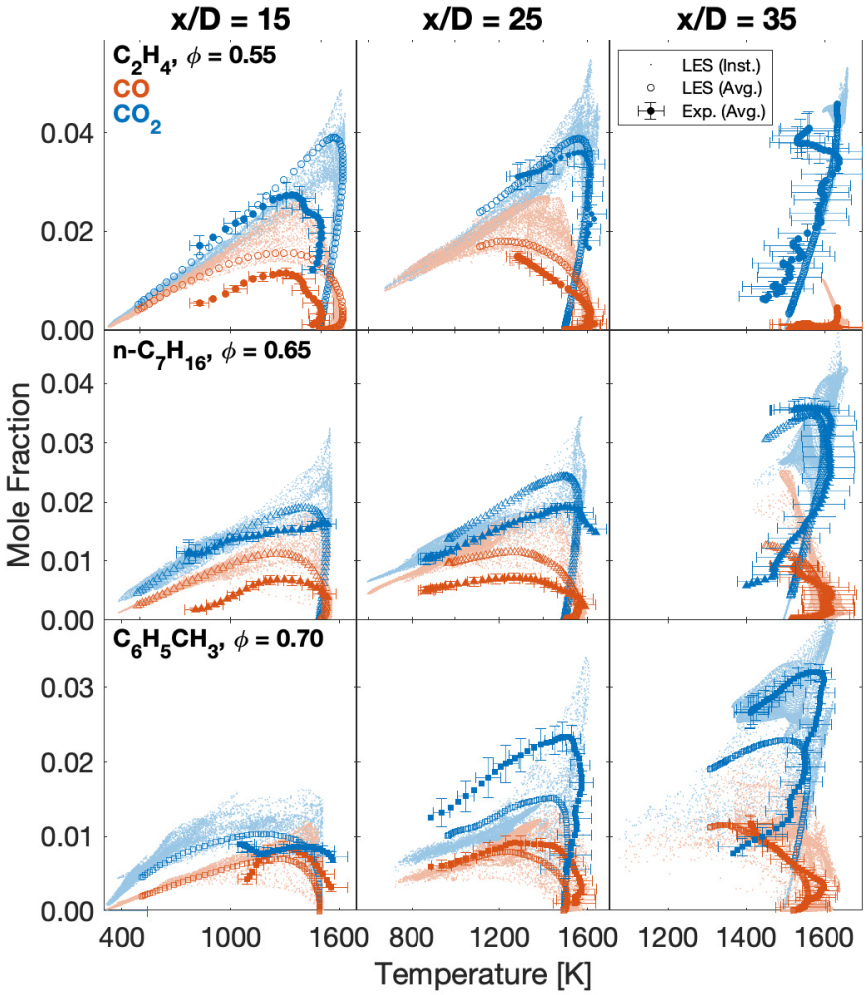

Figure 5.11: Comparison of $X_{\mathrm{CO}} - T$ and $X_{\mathrm{CO_2}} - T$ correlation data at different axial locations for flames fueled by C_2H_4 (top row), n-C_7H_{16} (middle row), and $C_6H_5CH_3$ (bottom row). Light-colored points indicate instantaneous LES data, open markers indicate time- and azimuthally-averaged LES data, and filled markers with error bars indicate experimental data. Some data points have been omitted for reader clarity.

chemistry coupling. The agreement between simulations and experiments improves with increasing downstream distance as the flame approaches thermochemical equilibrium. This is evident by the narrowing of the temperature scattering and the consumption of CO. Generally, X_{CO} is overpredicted at lower values of T, and is in agreement within uncertainty at higher values of T. While averaged CO-mole fraction profiles are overpredicted for (C_2H_4)-air and ($C_6H_5CH_3$)-air flames, the opposite trend is observed for the normal alkane fuel. The CO_2 peak value increases for the large hydrocarbon fuels, showing the highest CO_2-emissions as a consequence of the overall stoichiometry. Interestingly, the experimental CO_2 measurements in the ($C_6H_5CH_3$)-air flame are in better agreement with the instantaneous LES scatter data than with the averaged LES data at larger x/D. While predictions of $\mathrm{CO} - T$ scatter for the (C_2H_4)-air and ($C_6H_5CH_3$)-air flames are in good agreement with experimental data throughout the flame, the CO-formation is consistently overpredicted for the (n-C_7H_{16})-air flame on the fuel-rich side, which we primarily attribute to discrepancies in the turbulent mixing. Further measurements of the hydrodynamic flow-field are necessary to confirm this. The largest disagreements in thermochemical state-space exhibited by the fuel (n-C_7H_{16}) may also be partially attributed to a deficiency of the chemical model at low temperatures. The present results are consistent with quantitative species time-histories (CH_2O, OH, CO_2, H_2O) measured in previous shock tube oxidation experiments [131], which demonstrated that the oxidation rates of n-C_7H_{16} during low-temperature staged ignition are overpredicted by state-of-the-art chemical models.

5.4 Conclusions

In this study, quantitative spatially-resolved profiles of carbon monoxide, carbon dioxide, and temperature were obtained via mid-infrared laser absorption tomography in turbulent premixed jet flames of different fuels (ethylene, n-heptane, and toluene). The chosen fuels encompass a diverse sample of molecular structures encountered in practical energy conversion devices: alkenes, normal alkanes, and aromatics. The novel dataset of 2D thermochemical measurements—which defines a heat release boundary associated with the kinetically-slow

CO to CO_2 conversion—was directly compared with results of turbulent combustion simulations using LES methods. Fuel-specific effects are noted in both the multi-dimensional measurements and the modeling results; specifically, wider and taller flame brushes for the heavier molecular weight fuels are observed, indicating larger overall reaction zones for these flames despite normalization by flame speed. The LES predictions for all flames show generally good quantitative agreement with measurements, with larger discrepancies observed in upstream regions of the flames for the larger-molecular-weight fuels examined, namely *n*-heptane and toluene. A thermochemical state-space analysis was conducted, revealing potential discrepancies in the turbulent mixing and residual deficiencies in the low-temperature chemical model, representing opportunities for further investigation. More broadly, the coupled experimental and numerical investigation, united by quantitative thermochemical scalars, demonstrates a uniquely powerful approach to advance turbulent combustion models for a wide range of fuels and operating conditions.

CHAPTER 6

Tomographic Laser Absorption Imaging of Combustion Flows

The contents of this chapter have been published in the journal ***Optics Express*** *under the full title 'Tomographic laser absorption imaging of combustion species and temperature in the mid-wave infrared' [39]. Portions of this chapter's content include ongoing work under the full tile '3D tomographic laser absorption imaging of temperature, CO and CO_2 in laminar flames using masked Tikhonov regularization'.*

6.1 Background

Chapter 4 demonstrated that classical LAT has addressed some of the line-of-sight limitations of LAS by applying tomographic reconstruction techniques, but usually at the expense of slow measurement sampling by mechanical translation of the beam (Figure 6.1a) or optical arrangement complexity that scales with the multiplicity in requisite projections, or lines of sight (Figure 6.1b). The complexity of multi-projection fast-LAT has generally constrained practical application of the technique to the near-infrared where robust and inexpensive fiber optics and lasers are available, but detectable combustion species are few (e.g. H_2O) at the pathlength scales of most flames ($\sim$cm). Conventional LAT methods are also constrained in spatial resolution by beam size ($\sim$mm), and less suitable for small-diameter flows in practical combustion applications.

In the current work, an alternative approach, laser absorption imaging (LAI), is proposed that is practical for mid-infrared optical equipment (i.e. access to combustion intermediates)

and will enhance spatial resolution over traditional LAT by imaging flow-fields that are backlit with tunable mid-wave infrared laser radiation. The LAI method involves a single beam expansion and replacement of the detector with a high-speed camera, as compared schematically in Figure 6.1 to the moving line-of-sight approach and multi-projection laser absorption tomography technique. For LAI, spatial resolution is not determined by beam size, but by pixel size, and temporal resolution is constrained by the camera frame rate. Using recently developed high-speed IR cameras, it is possible that high speed and high spatial resolution sensing can be achieved via LAI with a straightforward optical arrangement. In the first half of this chapter, we present the first application of LAI in an axisymmetric Bunsen flame to measure 2D CO, CO_2 and C_2H_6 concentrations and temperature with a spatial resolution of 0.05 mm. In the second half of this chapter, LAI is extended to non-axisymmetric flows and 3D tomographic imaging of CO concentrations and temperature are presented for flow-fields involved a spatial convolution of two small-scale (<cm) laminar Bunsen-style flames.

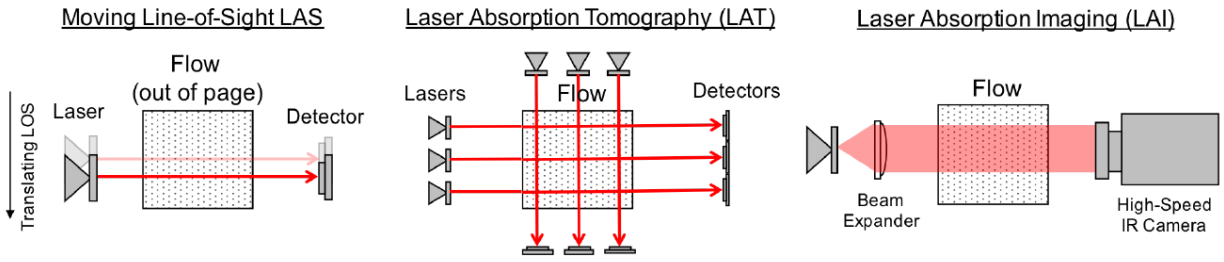

Figure 6.1: Spatially-resolved laser absorption measurement techniques: (a) translating line-of-sight, (b) multi-line-of-sight tomography, (c) laser absorption imaging

6.2 LAI for Axisymmetric Flows

6.2.1 Introduction

Tomographic absorption spectroscopy (TAS) has become an important optical approach to study high-temperature gas dynamics and reactive flows, including turbulent and laminar flames [3]. Laser absorption provides for a relatively straightforward, quantitative relationship to gas properties. In addition, calibration-free absorption techniques that exploit rapid laser tunability enable application to harsh combustion flows that often convolute other imaging techniques [2]. Advancements in TAS over the past decade, including several novel optical arrangements, have yielded significant improvement in spatial and temporal resolution. These advancements have mostly been confined to the near-infrared wavelength domain, where a multiplicity in laser beams and detectors comes at moderate cost and complexity, but the accessible combustion species are few (e.g. H_2O) at the pathlength scales ($\sim$cm) of most flames [55, 67, 92, 94, 132, 133]. By contrast, the mid-wave infrared provides for sensitive absorption spectroscopy of numerous gas species including fuels, intermediates, and products of combustion at their fundamental vibrational frequencies/wavelengths. However, optical methods for tomographic absorption spectroscopy in the mid-infrared have remained relatively rudimentary (e.g. mechanically translating line-of-sight) [32, 40, 91, 93, 134], limiting spatial and temporal data collection rates and utility in combustion studies. In this paper, we describe a novel tomographic laser absorption imaging method using mid-wave infrared optics and a high-speed camera that significantly enhances spatio-temporal data bandwidth (i.e. mapping a 2D flow-field in seconds vs. minutes or hours) and enables quantitative analysis of several combustion species and temperature in small-diameter flames utilized for fundamental combustion investigations.

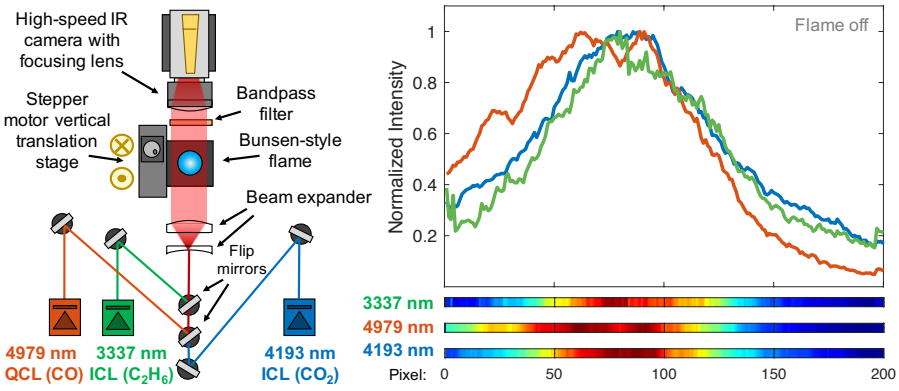

Figure 6.2: *(Left)* Arrangement of lasers, mirrors, Bunsen-style flame, and IR camera. *(Right)* Normalized beam profiles measured by IR camera for 200-by-2 pixel regions of interest.

6.2.2 Method

6.2.2.1 Optical setup

The optical arrangement for tomographic laser absorption imaging (LAI) involves one or more high-speed infrared cameras that image a flow-field backlit with tunable mid-wave infrared laser radiation. The simplest configuration, suitable for tomography of axisymmetric flows, includes a single laser and camera, shown in Fig. 6.2. The laser beam is expanded with a concave lens, similar to the fan beam method [55, 92, 133], and recollimated with a convex lens to pass through the flow of interest (at a size large enough to capture the entire width or half-width of the absorbing medium) and spectrally filtered to isolate the laser radiation. The enlarged beam ($d \approx 20$ mm) is then focused onto a 2D focal plane array comprising many detector pixels that effectively represent unique optical lines of sight from the collimated source sampled simultaneously. In this work, we use a high-speed IR camera (Telops TS-IR-MW) with a 640-by-512 pixel CCD array and mercury-cadmium-telluride (MCT) photodetector. The maximum frame rate of the camera is 107 kHz, which requires a significant reduction in the number of active pixels and integration time. For the experiments reported here, the frame size is set to 200-by-2 pixels, capturing a transverse slice of an axisymmetric flow, and the frame rate is 40 kHz with an exposure time of 3 μs.

The corresponding beam intensity profiles for the different lasers used in this study are shown in the right of Fig. 6.2. Each beam exhibited some diffraction patterns as imaged, but a relatively stable near-Gaussian section could be attained.

For demonstration of the LAI method, three tunable narrow linewidth mid-infrared lasers were used to measure absorption profiles of C_2H_6, CO, and CO_2, respectively, in the radial and vertical directions to characterize the thermochemical structure of a laboratory Bunsen-style C_2H_6-air flame, pictured in Fig. 6.3. For each experiment, only one laser and bandpass filter combination is used at a time. The burner is mounted on a vertical translation stage controlled by a stepper motor with a linear translation of 5 mm/sec (5 μm per step) to provide vertical resolution. The partially premixed flame was controlled via thermal-based mass flow controllers (MKS MFC GE50A) with flow rates of 179 sccm C_2H_6 and 1391 sccm air, corresponding to a fuel-rich mixture with a fuel-air equivalence ratio of $\phi = 2.14$ and exit velocity of 2.66 m/s. The exit of the stainless steel burner is 3.7 mm in diameter, resulting in a laminar jet Reynolds number of ≈ 230. Upon leaving the burner, the premixed gases entrain and mix with ambient air, producing a stable, reproducible flame with no flashback risk.

6.2.2.2 Mid-IR laser absorption spectroscopy

A scanned-wavelength direction absorption technique is utilized to spectrally-resolve select rovibrational lines of the target species [1]. For CO_2, we utilize an interband cascade laser (ICL) with ≈ 5 mW output power near 4.19 μm to probe the R(0,58) line at 2384.189 cm^{-1}, as well as the doublet line pair R(1,105) and R(1,106) at 2384.327 cm^{-1} and 2384.331 cm^{-1}, respectively, to measure CO_2 mole fraction and vibrational temperature [89]. For CO, we use a quantum cascade laser (QCL) centered near 4.97 μm with ≈ 50 mW output to probe the P(0,31) and P(1,26) lines at 2008.53 cm^{-1} and 2006.78 cm^{-1}, to similarly recover mole fraction and temperature [95]. For C_2H_6, we use an ICL near 3.34 μm with ≈ 1 mW output power to scan over a collection of lines near 2996.9 cm^{-1} comprising the $^{R}Q_3$ branch of the ν_7 C-H stretch band [135].

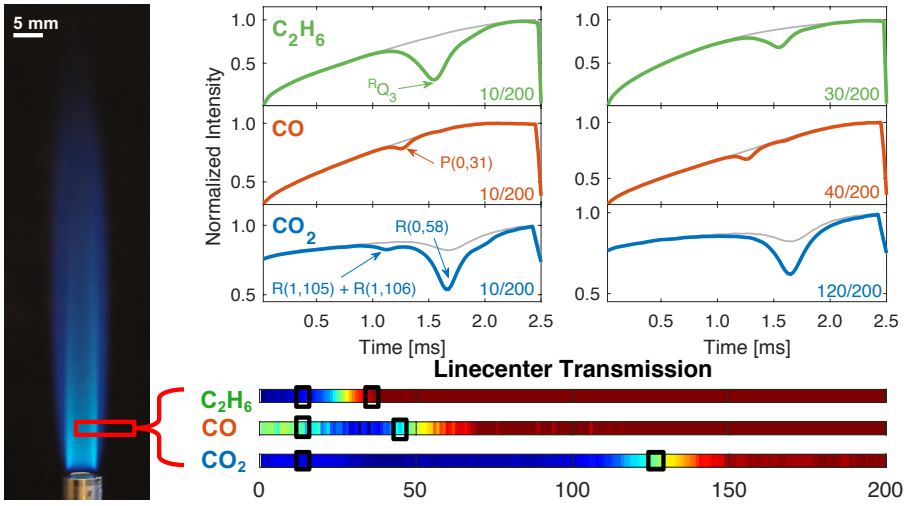

Figure 6.3: *(Left)* Example 200-by-2 pixel region of interest on flame. *(Top)* Background signals (I_0) without flame (gray) and absorbance signals (I_t) with the flame (color) for different pixels (10 laser scans averaged). *(Bottom)* Example linecenter transmission for each species.

The lasers are injection-current scanned across specified wavenumber (ν) ranges at 400 Hz, corresponding to 100 data points per laser scan period on each pixel (at the 40 kHz camera frame rate). The burner is continuously translated vertically during the data acquisition. Example intensity scans for pixels corresponding to different radial locations in the flame are shown in Fig. 6.3. For each pixel, we performed a running time-average of 10 scans during the vertical translation, resulting in an effective vertical resolution of ~0.125 mm. Stage translation involved 240,000 frames collected in 6 seconds, resulting in a 366 MB data file. The high-speed IR camera (Telops TS-IR-MW) is equipped with a 1 GB buffer memory. For each laser setup, five separate flame measurements (or vertical passes) were taken, increasing the total sample size to 50 scans per vertical interval and facilitating uncertainty analysis.

For a non-uniform gas medium axially-symmetric in r [cm], the Beer-Lambert law integrated over ν—or the projected integrated absorbance area $A_{j,proj}(r)$ [cm^{-1}]—is expressed for each line-of-sight or pixel in Eq. 6.1 [3],

$$A_{j,proj}(r) = \int_{-\infty}^{\infty} \alpha_\nu d\nu = \int_{-\infty}^{\infty} -\ln\left(\frac{I_t}{I_0}\right)_\nu d\nu = \int_0^{L(r)} K_j(r) dl \tag{6.1}$$

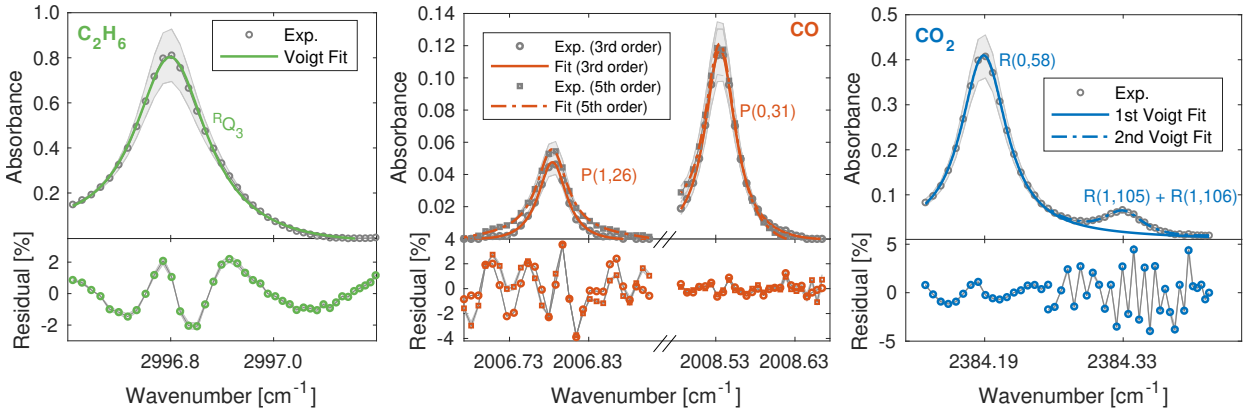

Figure 6.4: Absorbance α_ν, Voigt fits, and residuals for transitions corresponding to *(Left)* C_2H_6, *(Middle)* CO, and *(Right)* CO_2. Absorbance measurements are averaged from 10 laser scans, and shaded regions indicate uncertainty corresponding to 95% confidence intervals.

where α_ν is spectral absorbance, I_0 is incident intensity (measured or inferred without the flame), and I_t is transmitted intensity (measured with the flame). $L(r)$ [cm] is the aggregate path length at radial position r from the axis of symmetry. Individual pixel measurements of α_ν for each rovibrational transition j of interest, along with associated measurement uncertainties, are shown in Fig. 6.4. As indicated, 20 to 30 data points are sampled over the spectral domain for each transition. We attain $A_{j,proj}(r)$ by fitting a Voigt function to the measured α_ν profile for each line j [1]. Although the projected absorbance lineshapes are not expected to perfectly reflect a Voigt profile, the residuals after fitting proved sufficiently low ($\sim$2%) to justify the convenience of this approach for recovering areas.

Generally, the noise level on individual camera pixels after the moderate averaging was similar to that observed using conventional photovoltaic detectors [32], yielding similar precision, but uncertainties associated with baseline fitting were larger in some cases. For a signal-to-noise ratio (SNR) criteria of SNR $\geq$ 5, this corresponded to a typical minimum measurable and acceptable α_ν of $\sim$0.01 for all transitions j. For the interband cascade lasers, a measured baseline signal was used to capture the ambient absorption along the beam path and non-linearity in laser output. However, for the quantum cascade laser (probing CO), temporal fluctuations in intensity scan-to-scan—attributed to unsteady diffraction

internal to the camera—precluded the use of a measured empirical baseline I_0 signal, instead requiring a baseline fitting scheme on the measured I_t that added measurement uncertainty. Various polynomial fits on the non-absorbing regions of the scan were attempted. As can be seen in Fig. 6.4, the Voigt fit of the P(1,26) line is more strongly influenced by the baseline fitting choice than that of the P(0,31) line, partly owing to its lower α_ν. The mean values of a 3rd order polynomial baseline fit yielded more consistent $A_{j,proj}(r)$ and so were used for all data reported in this study while the baseline fitting variation was incorporated into the measurement uncertainty. For CO_2, we attain $A_{j,proj}(r)$ for the R(1,105) + R(1,106) doublet line by employing a sequential Voigt fitting scheme in which a fit of the R(0,58) line is subtracted from the overall measurement as shown in Fig. 6.4. Notably, ambient CO_2 was measured in the baseline I_0 signal (mostly along the ∼80 cm optical path outside of the flame). This background CO_2 absorbance varied little (∼1%) between the flame on or off condition and was determined to contribute less than ±400 ppm of error to the mole fraction results. Further details on the sequential fitting procedure and ambient CO_2 uncertainty are documented in previous work [32].

Images constructed from measured $A_{j,proj}(r)$ of selected transitions during burner translation are shown in Fig. 6.5, highlighting the spatial resolution capability of the technique. These line-of-sight measurements of $A_{j,proj}(r)$ have a horizontal pixel resolution of 50 μm/pixel, which was determined by placing a calibration card of known dimensions in the imaging plane and measuring the number of pixels that reported a blocked transmission intensity of less than 20%. It can be noted that the images demonstrate moderate streak-like discontinuities along the vertical direction, which we attribute to residual diffraction effects. These mild artefacts in the raw data generally do not propagate to the reconstructions of temperature and mole fraction due to the regularization methods employed (to be further discussed). Recalling Eq. 6.1, the thermochemical properties of interest are embedded in the radially-resolved absorption coefficient $K_j(r)$ [cm^{-2}], given by Eq. 6.2,

$$K_j(r) = PS_j(T(r))X_{\text{abs}}(r) \tag{6.2}$$

where total pressure P [atm] is assumed constant, $S_j(T(r))$ [cm^{-2}/atm] is the linestrength

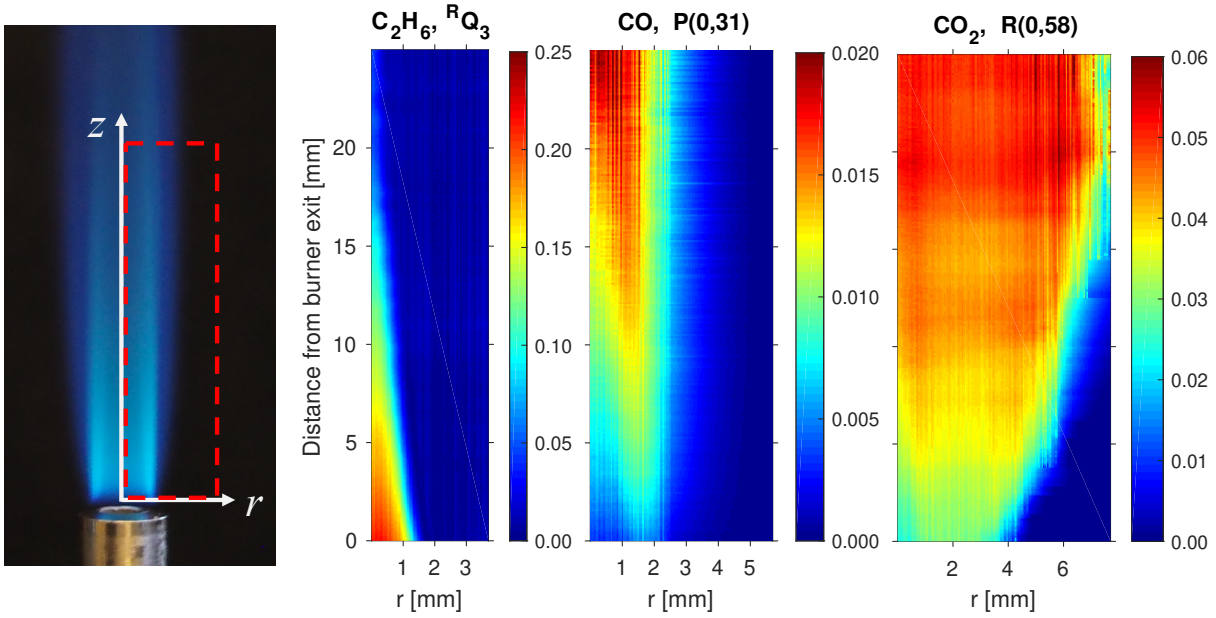

Figure 6.5: *(Far Left)* Photograph of flame with the IR-imaged region outlined. *(Right)* Projected absorbance areas $A_{j,proj}$ for selected rovibrational transitions of C_2H_6, CO, and CO_2.

of transition j at temperature $T(r)$ [K], and $X_{\text{abs}}(r)$ is the mole fraction of the absorbing species.

6.2.2.3 Tomographic reconstruction and thermometry

Assuming the flame is axisymmetric and steady, 1D classical absorption tomography can be applied to each transverse slice of the flame using a numerically integrated Abel transform method, and we can determine radial profiles of $K_j(r)$ from $A_{j,proj}(r)$ [3, 32, 40]. To do this, the flame region is divided into equally spaced annular rings and the radial absorption coefficient distribution is approximated by a quadratic function near radius r using the Abel 3-point (ATP) method [37]. The measured $A_{j,proj}(r)$ (Fig. 6.6) are smoothed and deconvoluted using Tikhonov regularized Abel inversion to address the inherent ill-conditioned nature of the projection matrix. A suitable regularization parameter is determined from the L-curve method following Daun et al. [38] to be $\lambda \approx 1$ and is used for all reconstruc-

tions. Since this process uses information from neighboring pixels, it reduces the effective tomographic resolution [3, 136].

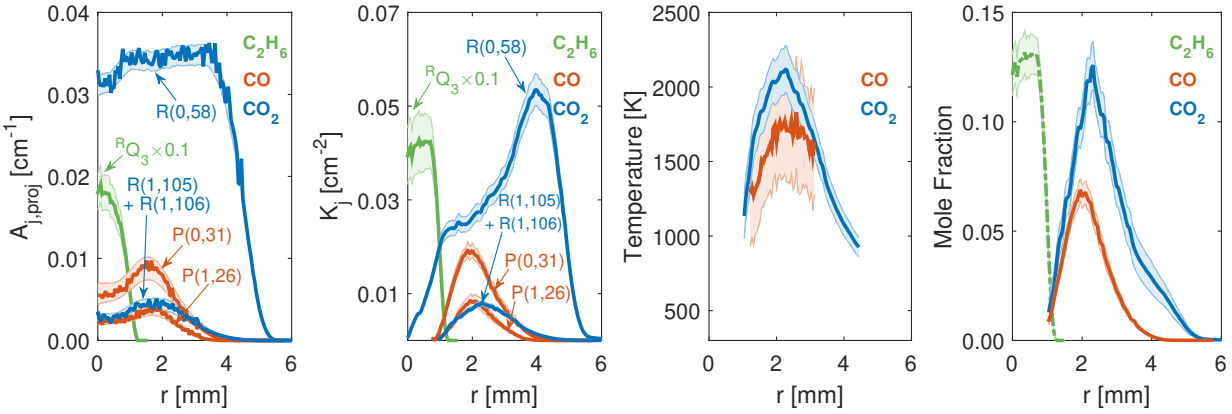

Figure 6.6: Data analysis for a row of pixels (z = 2.5 mm). Shaded regions indicate uncertainty. *(Far left)* Path-integrated absorbance area, $A_{j,proj}(r)$. *(Left)* Reconstructed absorption coefficients, $K_j(r)$. *(Right)* Vibrational temperatures of CO and CO_2. *(Far right)* Mole fractions of the species, where a uniform temperature of 400 K is assumed to estimate $X_{C_2H_6}$.

We scan multiple transitions j and thus can determine multiple $K_j(r)$, shown in Fig. 6.6. Then, using established two-line thermometry methods [1, 32], we infer gas temperature $T(r)$ from a ratio of line-strengths $S_j(T(r))$ (available in the HITRAN database [88] for the lines of interest), and obtain $X_{abs}(r)$ per Eq. 2. Here, we treat the integrated collection of C_2H_6 transitions as a single line j and approximate $X_{C_2H_6}$ using a constant temperature assumption based on a thermocouple measurement in the core and the pseudo line-list of spectral parameters from Harrison [135]. Although the uncertainties in temperature and mole fraction varied depending on flame location, CO and CO_2 temperatures could be typically determined within ±350 K and ±130 K, respectively, while mole fractions for each species could be typically determined within ±10% and ±6%, respectively. These uncertainties, including those shown in Fig. 6.6, are calculated using derivations available in our previous work [32].

6.2.3 Results

The radial profiles depicted in Fig. 6.6 demonstrate the ability of LAI to spatially resolve mole fraction of fuels, intermediates, and products of combustion, as well as gas temperature in an axisymmetric flame. Generally, the range of scalar values observed are consistent with that expected over the range of equivalence ratios in the partially premixed C_2H_6-air flame. Peak temperatures are in the range of 2200–2400 K ($T_{\mathrm{ad,max}} = 2370$ K). Mass flow readings correspond to an inlet $X_{C_2H_6}$ of 0.114, which agrees well with the tomographic estimate shown in Fig. 6.6. For CO and CO_2, vibrational temperature is shown in regions where the ratio of line intensities could reliably be measured (SNR >5). The aforementioned baseline uncertainty and low absorbance of the P(1,26) CO line in many regions of the flame ($\alpha_\nu \sim 0.01$–0.02) resulted in relatively large uncertainties in CO temperature relative to CO_2 temperature, and potentially a systematic bias yielding somewhat lower CO temperatures. The spatial evolution of these temperatures and species mole fractions can be inspected by assembling the transverse slices along the vertical axis, such as in Fig. 6.6, to produce two-dimensional reconstructed images of the flame.

Images of temperature and mole fraction from both CO and CO_2 measurements are shown in Fig. 6.7. For each species, mole fraction and temperature is shown for heights z that include radial measurements that extend to the ambient boundary condition (i.e. zero absorption after correcting for ambient concentrations), a requirement for performing 1D classical absorption tomography. This primarily affects CO_2, which rapidly diffuses out of the available pixel window at $z > 20$ mm. The temperature is lower in the core of the flame and generally peaks just beyond the radius of the burner, which corresponds to the interface of CO to CO_2 terminal oxidation. As the height above the burner z increases, T also increases, corresponding with an increase in CO_2 concentration seen in the mole fraction images. CO concentration is largely confined to a region between the initial oxidation of C_2H_6 and terminal oxidation to CO_2, providing a good indicator of the reaction zone. At larger z, some unsteadiness in the flame becomes more apparent with entrainment of ambient air, precluding reliable reconstruction efforts without an increase in sample size of flame

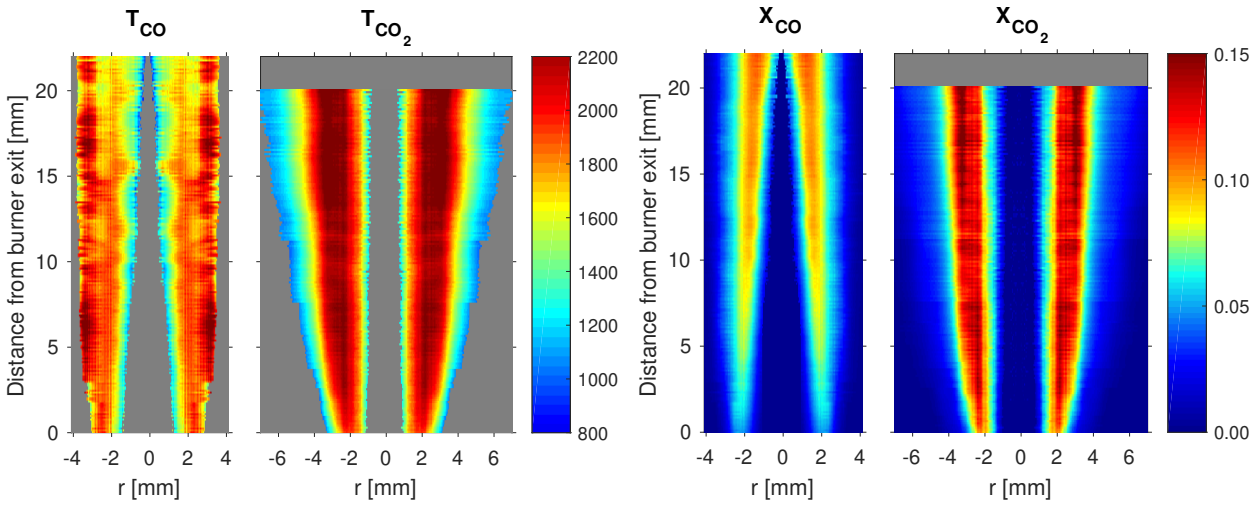

Figure 6.7: Reconstructed temperature [K] *(left)* and mole fraction *(right)* images for CO and CO_2. Images have been reflected about the axis of symmetry for reader clarity.

experiments. For the heights imaged, there is little CO_2 diffusion into the core of the flame, though CO_2 monotonically diffuses outward radially as z increases.

6.2.4 Discussion and conclusions

The aforementioned results demonstrate tomographic laser absorption imaging (LAI) as an effective technique for quantitative spatially-resolved measurements of multiple species and temperature in axisymmetric reacting flows. LAI provides a superior combination of spatial resolution and data collection bandwidth compared to previous laser absorption tomography techniques utilized in the mid-wave infrared. The effective spatial resolution for line-of-sight absorbance is $\sim$50 μm in the horizontal direction and $\sim$125 μm in the vertical direction, representing approximately an order of magnitude improvement over tomographic techniques for which laser beam size is the limiting factor in spatial resolution [32, 91, 93, 94, 134]. Utilizing the LAI setup described in this paper, 2D mapping of an axisymmetric steady flame on the centimeter scale can be completed in less than 10 seconds for a particular laser setup. Compared to tomography techniques utilizing multiple mechanical translation

stages on similarly-sized flames, this represents a ∼200-fold reduction in data collection time [32]. As such, for quasi-steady flame studies requiring many repeated measurements for statistically significant conclusions or high mass flux experiments that require large amounts of fuel, LAI provides an enabling new method to quantitatively and efficiently characterize fluid-chemistry interactions.

6.3 LAI for Non-axisymmetric Flows

6.3.1 Introduction

Tomographic absorption spectroscopy (TAS) is a powerful non-intrusive diagnostic method to spatially-resolve thermochemistry in reacting flows [3]. Recent advances in mid-wave infrared lasers have enabled TAS at the fundamental vibrational frequencies of many combustion species of interest, facilitating high-sensitivity detection [33, 91, 93] and enabling quantitative investigations of small-diameter (<1 cm) flames [32, 39, 40, 42]. Laser absorption imaging (LAI) is a complimentary method designed to capture scenes backlit with tunable laser radiation at very high spatial resolution using high-speed infrared cameras to yield spatio-temporally rich datasets [39, 42, 137]. A representative LAI optical setup is shown in Fig. 6.8. The technique has been successfully coupled with 1D tomography for quantitative imaging of axisymmetric flow-field thermochemistry at sub-100 μm spatial resolution [39, 42].

Tomographic imaging of *non-axisymmetric* flows poses more difficulties—multiple projection angles are needed to estimate the flow-field scalars, and the inversion problem is usually underdetermined [3, 59]. In recent years, research efforts to perform absorption tomography in these combustion flows have yielded several approaches to the inversion problem, including both linear [35, 55, 92, 94, 133, 138] and non-linear [67, 69, 139] methods utilizing several novel optical arrangements with many lines of sight. However, these methods are mostly done in a 2D manner, measuring a cross section of the flow field or stacking 2D cross sections to form the so-called 2.5D or qusi-3D measurements [94]. As sensing methods become more data-rich—LAI readily yields thousands of simultaneously-sampled lines of sight

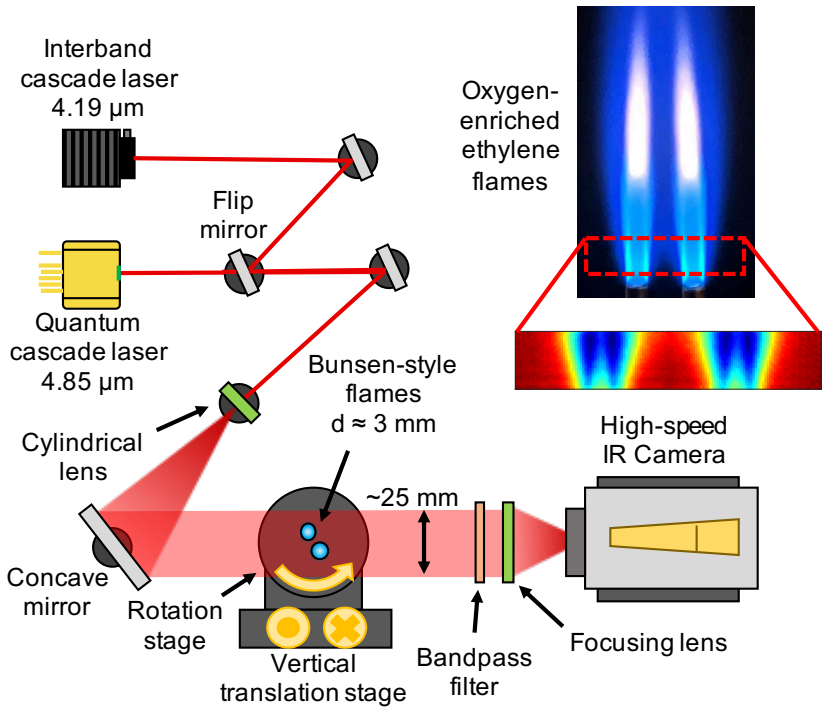

Figure 6.8: Optical setup for this work, showing alignment with QCL and ICL. Inset flame shows transmission near the P(0,20) line of CO.

in the form of 2D images [137]—tomographic reconstruction techniques with 3D capability are needed for resolving the 3D nature of reacting flows.

In this study, we extend LAI to 3D non-axisymmetric flows using linear tomography and demonstrate—to the authors' knowledge—the first application of a 3D masked Tikhonov regularization method to experimental absorption imaging, obtaining quantitative species and temperature fields in a doublet laminar flame configuration. We first present the development of the physical optical setup for multi-projection linear tomography, and then describe both the 2D and the 3D masked Tikhonov regularization method for linear tomography as applied to flame imaging. Resulting images of CO and CO_2 mole fraction and temperature are compared between the two reconstruction approaches with various numbers of projection measurements. The paper concludes with a demonstration of the utility of 3D masked Tikhonov regularization in better resolving the spatial gradients in the flow field as compared to standard Abel inversion results of a single flame.

6.3.2 Methods

6.3.2.1 Experimental Setup

The experimental configuration for this study is adapted from previous demonstrations of LAI [39, 137], and utilizes a high-speed infrared camera (Telops FAST-M3K) to image a flowfield backlit with tunable laser radiation in the mid-wave infrared, as shown in Fig. 6.8. A distributed feedback (DFB) quantum cascade laser (QCL) near 4.85 μm is used to spectrally scan across the P(0,20) and P(1,14) rovibrational transitions of CO [134]. An interband cascade laser (ICL) near 4.19 μm is similarly used to scan across the R(0,58) line and R(1,105) + R(1,106) doublet lines of CO_2 [89]. The beam is horizontally expanded with a cylindrical lens and re-collimated with a concave mirror, then pitched through the flowfield comprising two Bunsen-style flames, each with flame brushes approximately 3 mm in diameter. The beams are spectrally isolated with bandpass filters (4860 $\pm$ 96 nm (CO) and 4210 $\pm$ 120 nm (CO_2)), and a plano-convex lens focuses the expanded beam onto the detector array of the camera. The beam is captured in the camera detector subwindow of size 128$\times$24 with a frame rate of 40 kHz and integration time of 5 μs. Both lasers are injection-current tuned using a sawtooth waveform at 400 Hz, resulting in 100 points per scan for subsequent spectral fitting. For each projection angle measurement (Section 6.3.2.2), data is collected and averaged over 1 second (400-scan average), an interval over which the flames are assumed steady. Spatial resolution was evaluated by imaging a wire mesh with known dimensions backlit with laser radiation [42], and was determined to be approximately 70 μm per pixel in the horizontal direction.

For 3D tomographic LAI, we utilize the tunable lasers to measure absorption profiles of CO and CO_2 in quasi-steady partially-premixed Bunsen-style flames. The dual flame assembly is mounted on a rotation stage and vertical translation stage to capture of multiple projection angles and heights for the tomographic reconstruction, as shown in Fig. 6.9. Two different fuels in oxygen-enriched air are utilized to assess differences amongst multiple flow conditions: ethane (C_2H_6) and ethylene (C_2H_4). The reactant flows are controlled by mass

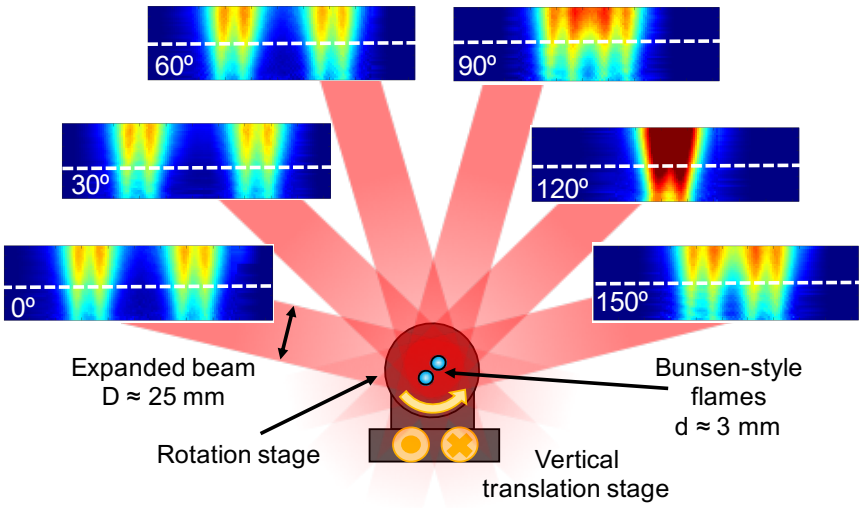

Figure 6.9: Representation of the CO P(0,20) $A_{j,\mathrm{proj}}$ images relative to the rotation angle of the Bunsen-style flames.

flow controllers (MKS MFC GE50A) with overall flow rates of 128 sccm C_2H_4/C_2H_6, 79 sccm N_2, and 101 sccm O_2, corresponding to an equivalence ratio of $\phi = 4.43 \pm 0.07$ for C_2H_6, and $\phi = 3.80 \pm 0.07$ for C_2H_4. After the tubing is split to the two burners, one flow is measured with a rotameter to ensure equal flow through each burner. The exit velocity of each flow is 0.41 m/s and the jet exits of the stainless steel burners are 1.6 mm in diameter, providing a laminar jet Reynolds number of ∼44.

6.3.2.2 Laser absorption tomography

The linear tomographic reconstruction process in two dimensions is described by Fig. 6.11. The equations of LAT are thoroughly detailed in the literature [3, 35, 67, 92, 94, 133, 138, 140], but we provide a brief overview here for context and nomenclature. For a non-uniform gas medium, the Beer-Lambert law integrated over wavenumber ν [cm^{-1}]—or the projected absorbance area $A_{j,\mathrm{proj}}$ [cm^{-1}]—can be expressed for each line-of-sight with pathlength L [cm]

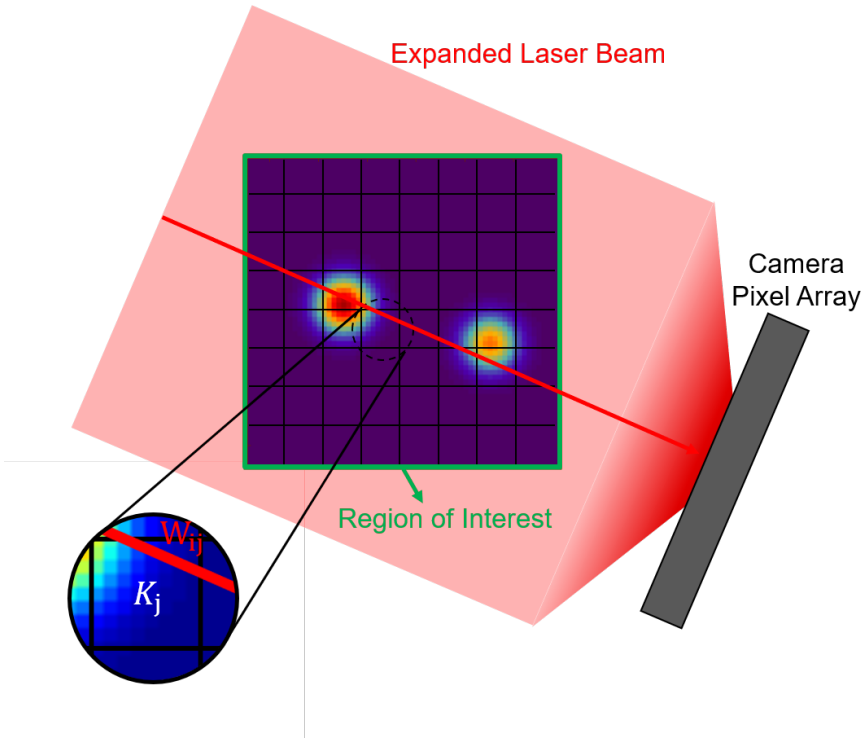

Figure 6.10: Discrete formulation of the tomographic LAI problem.

and related to thermodynamic gas properties in Eq. 6.3 [2],

$$\begin{aligned} A_{j,\text{proj}} &= \int_{-\infty}^{\infty} \alpha(\nu) d\nu = \int_{-\infty}^{\infty} -\ln\left(\frac{I_t}{I_0}\right)_{\nu} d\nu \\ &= \int_0^L K_j dl = \int_0^L P S_j(T) X_{\text{abs}} dl \end{aligned} \tag{6.3}$$

where $\alpha(\nu)$ is spectral absorbance, I_0 is incident intensity, and I_t is transmitted intensity. L [cm] is the aggregate path length along the line-of-sight. The thermochemical properties of interest are embedded in the spatially-resolved absorption coefficient K_j [cm^{-2}], where total pressure P [atm] is assumed 1 atm, $S_j(T)$ [cm^{-2}/atm] is the linestrength of transition j at temperature T [K], and X_{abs} is the mole fraction.

6.3.2.3 2D Tikhonov Regularization

For 2D tomographic LAI, Eq. 6.3 applies to *each* camera pixel, resulting in 2D images for $A_{j,\text{proj}}$; given multiple projection angles, each horizontal row of pixels can be treated inde-

pendently for subsequent reconstruction, as shown in Fig. 6.11. In this study, the forward projection process is modeled as a linear parallel-beam tomography problem and is formulated in a discrete format as shown in Fig. 6.10, where the flow field is discretized into a 100×100 rectangular grid probed by 128 parallel lines of sight from 6 projection angles. Writing Eq. 6.3 for all 6×128 lines of sight yields a system of linear equations:

$$\mathbf{W}_{2\mathrm{D}}\mathbf{K_j} = \mathbf{A_{j,proj}} \tag{6.4}$$

where $\mathbf{A_{j,proj}}$ and $\mathbf{K_j}$ represent the projection sinogram and 2D field of the absorption coefficients, respectively, both in vector form. $\mathbf{W}_{2\mathrm{D}}$ is the 2D projection weight matrix, where $W_{2\mathrm{D}_{ij}}$ represents the absorption length for the ith beam passing through the jth pixel. Due to limited-angle measurements, matrix $\mathbf{W}_{2\mathrm{D}}$ is rank-deficient (and inherently ill-posed), which is typically addressed with Tikhonov regularization [3, 35, 59]. In this approach, the rank-deficient matrix equation is augmented by a second set of equations, $\lambda\mathbf{L} = 0$, where λ is the regularization parameter and $\mathbf{L}$ is the discrete Laplacian matrix that is used to enforce the smoothness condition:

$$L_{i,j} = \begin{cases} 1 & i = j \\ -1/n_i & i \text{ neibors } j \\ 0 & \text{otherwise} \end{cases} \tag{6.5}$$

To obtain spatially-resolved thermochemical profiles for a horizontal plane—such as that marked by dashed lines in Fig. 6.9—we use 2D Tikhonov regularization and determine the distribution of K_j by finding a least-squares solution to the combined set of equations:

$$\mathbf{K}_{\mathbf{j},\lambda} = \arg\min \left|\left| \begin{bmatrix} \mathbf{W}_{2\mathrm{D}} \\ \lambda\mathbf{L} \end{bmatrix} \mathbf{K_j} - \begin{bmatrix} \mathbf{A_{j,proj}} \\ 0 \end{bmatrix} \right|\right| \tag{6.6}$$

Examples of these reconstructions are shown in Fig. 6.11. Noteworthy in the resulting reconstructions of K_j are streaks associated with the limited number of projection angles used [59]. The influence of projection angle number on the results is detailed in Section 6.3.3. Spatially-resolved temperature is obtained from the ratios of K_j using established two-line thermometry techniques [1]. Once temperature is known, mole fraction can be directly

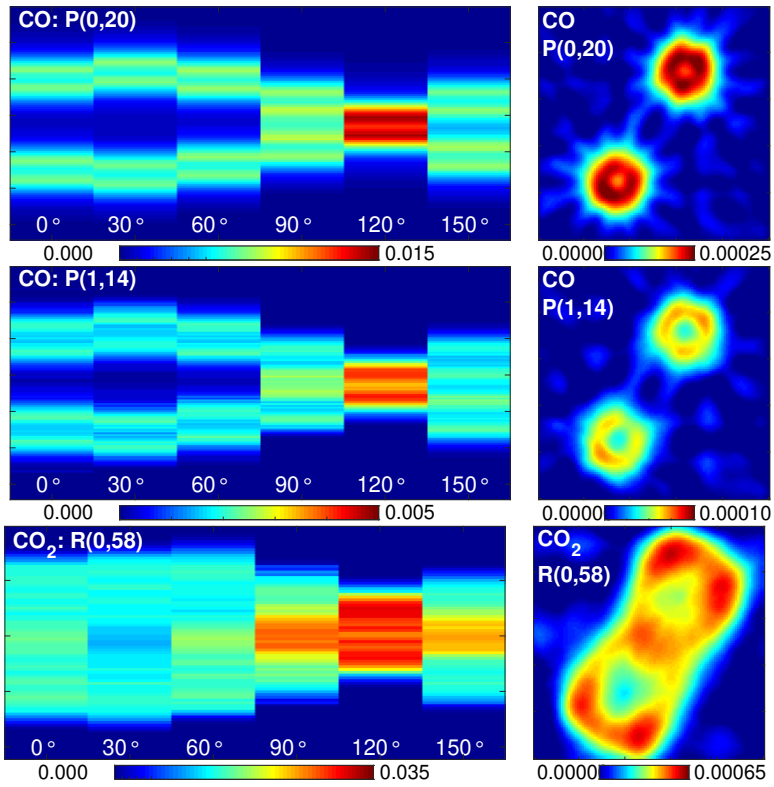

Figure 6.11: Representative linear tomography results for various horizontal planes from different flames. *Left:* $A_{j,\mathrm{proj}}$ sinograms of the spectral lines using the six projection angles shown in Fig. 6.9. *Right:* Reconstructed K_j for the same lines.

calculated from measured K_j of either transition through Eq. 6.3, and some representative results are shown in Fig. 6.12. The procedure can be repeated for every horizontal plane recorded in the flow. For the rich flames in this study, CO_2 diffuses rapidly out of view of the camera, precluding accurate tomographic reconstruction in higher planes. Rather than sacrifice spatial resolution by zooming out to capture more of the CO_2, we capture the region closest to the burner exits for a limited number of heights, and focus our analysis on CO, a strong indicator of the flames' reaction zones.

6.3.2.4 3D Tikhonov Regularization

For 3D Tikhonov regularization, the flow field is treated as a 3-dimensional space instead of independent planes as in the aforementioned 2D tomography. In this case, the flow field is

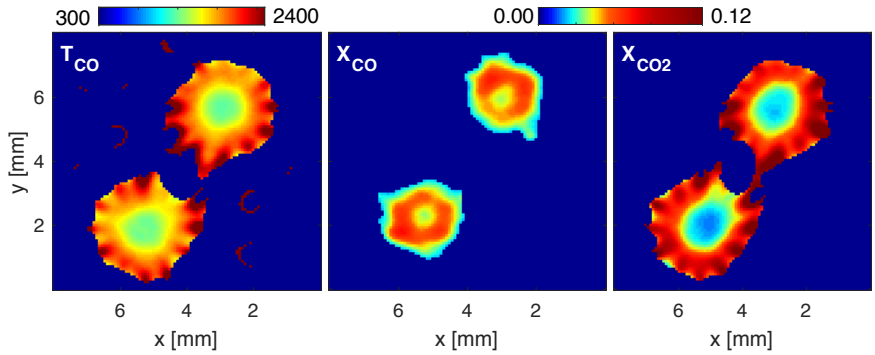

Figure 6.12: Results of linear tomographic reconstruction for temperature, CO, and CO_2 from various flames investigated in this study.

discretized into a $100 \times 100 \times 36$ cubic voxels probed by 128×36 parallel lines of sight from 6 projection angles. Similar, the 3D field of K_j can be found by a least-squares solution to the combined set of equations:

$$\mathbf{K_{j,\lambda}} = \arg\min \left|\left| \begin{bmatrix} \mathbf{W}_{3D} \\ \lambda \mathbf{L} \end{bmatrix} \mathbf{K_j} - \begin{bmatrix} \mathbf{A_{j,proj}} \\ 0 \end{bmatrix} \right|\right| \tag{6.7}$$

In the 3D case, $\mathbf{A_{j,proj}}$ contains all $6 \times 128 \times 36$ projection measurements and $\mathbf{K_j}$ represent 3D field with $100 \times 100 \times 36$ discrete absorption coefficients, respectively, both in vector form. $\mathbf{W}_{3D}$ is the 3D projection weight matrix, where $W_{3D,ij}$ represents the absorption length for the ith beam passing through the jth pixel. $\mathbf{L}$ is the discrete 3D Laplacian matrix that shares a similar form to the 2D Laplacian matrix in Eq. 6.5 except for the value of n_i. In 3D regularization, $n_i = 6$ as every voxel in the 3D space neighbors 6 other voxels while in 2D regularization $n_i = 4$ as each pixel in the 2D space is only surrounded by neighboring 4 pixels. 3D distribution of temperature and mole fraction can then be determined from the ratios K_j using two-line thermometry techniques for each voxel.

6.3.2.5 3D mask

In 3D parallel-beam tomography, the reconstruction volume is in the shape of a cuboid which is often larger than the studied flow. It is then desired to define a tighter working volume by defining a mask indicating the active voxels and the ones which are fixed during the

optimization. In this approach, 2D masks are defined by the user (by setting a threshold value) on the projected absorption area images and backprojected into a 3D mask as shown in Fig. 6.13. Absorption area data below the threshold associated with nonvalid rays, and the corresponding rows of the weight matrix $\mathbf{W}_{3D}$, are deleted from the optimization process 6.7. This process is not only useful for reducing the computing cost. but also helps to confined the artifacts in the reconstructed volumes as demonstrated in a previous work on background-oriented schlieren (BOS) measurements [141]. Reconstruction results with the masked 3D Tikhonov regularization are shown in Fig. 6.14 in comparison with the unmasked results.

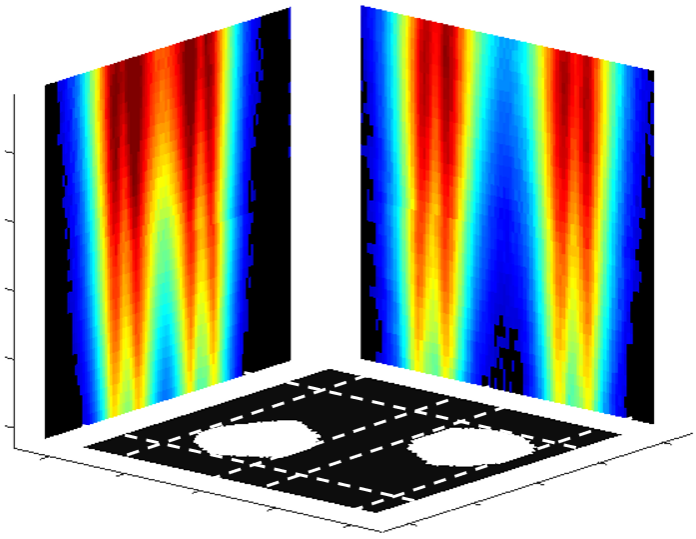

Figure 6.13: Schematic showing the masked region in one plane of the reconstruction volume and 2 orthogonal projection measurements. The white dash lines indicates the back-projection path from the 2 projection measurements. The black region shows the masked region after accounting for all 6 projections.

6.3.3 Results

6.3.3.1 3D tomographic laser absorption imaging

3D tomographic imaging of CO mole fraction and temperature in a C_2H_4 flame are shown in Fig. 6.14 using the 3 methods discussed in section 6.3.2.2. Firstly, 2D Tikhonov regularization is used to reconstructed 2D fields of temperature and mole fraction corresponding to different rows of pixels and then assembled into 3D images as shown on the left of Fig. 6.14. 3D Tikhonov regularization is also applied to reconstruct the whole 3D fields of temperature and mole fraction spontaneously as shown in the middle of Fig. 6.14. Lastly, a masked 3D Tikhonov regularization based on a threshold absorption area value of 0.002 cm^{-1} is applied to further constrain the reconstruction volume for 3D Tikhonov regularization with results shown on the right of Fig. 6.14. Neither the temperature nor the mole fraction are resolved in regions with very low absorbance. These regions are not plotted for clarity. Specific x-z, y-z, and x-y planes have been highlighted to display internal flame structure.

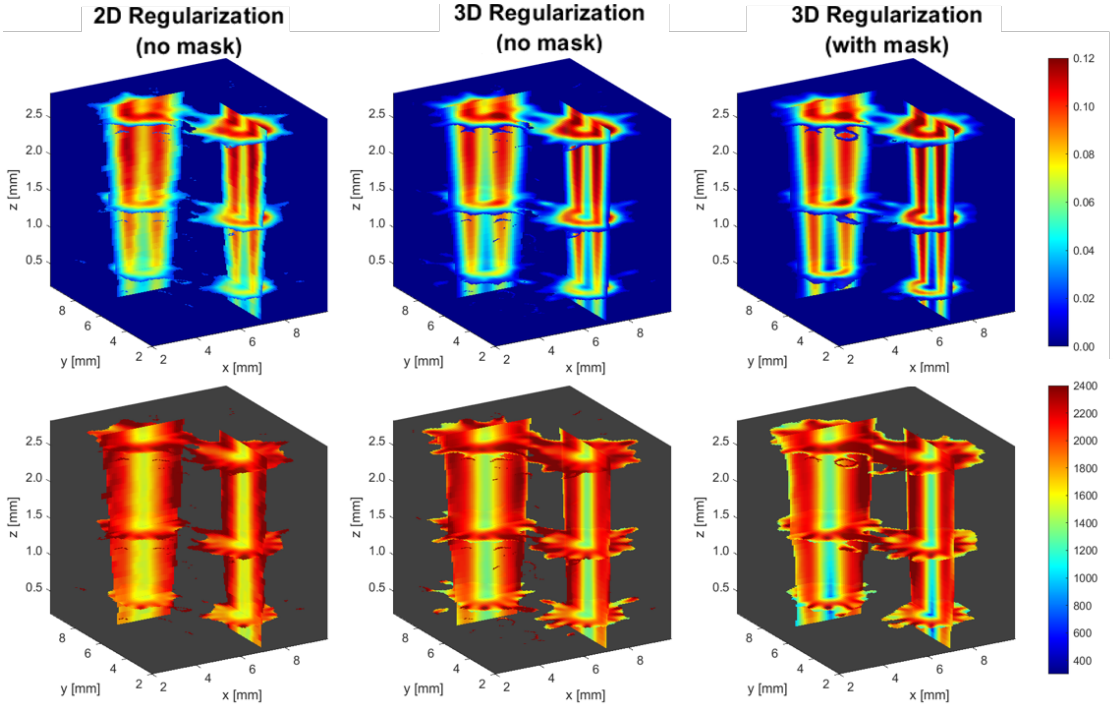

Figure 6.14: Three-dimensional tomographic reconstructions of CO mole fraction *(top)* and temperature *(bottom)* generated from 2D regularization (no mask) *(left)*, 3D regularization (no mask) and 3D regularization (with mask) *(right)*.

6.3.3.2 Influence of number of projection angles

In many applications of tomography in reacting flows, increasing the number of projection angles generally improves the resolution of voids and peaks in both temperature and mole fraction fields while also reducing the number of streak-like artifacts generated [44, 59]. In this section, the effect of number of projection angles is studied based on 2D Tikhonov regularization. As a benchmark, an Abel inversion was applied to a projection measurement of an isolated single flame to reconstruct the radial temperature and mole fraction profiles assuming steady, axi-symmetric conditions. These reference profiles were expanded to two dimensions and compared to those generated by linear tomography using both six and eleven projection angles in Fig. 6.15. Eleven projection angles were found to reduce the differences between the linear tomographic reconstruction result and the reference reconstruction as well

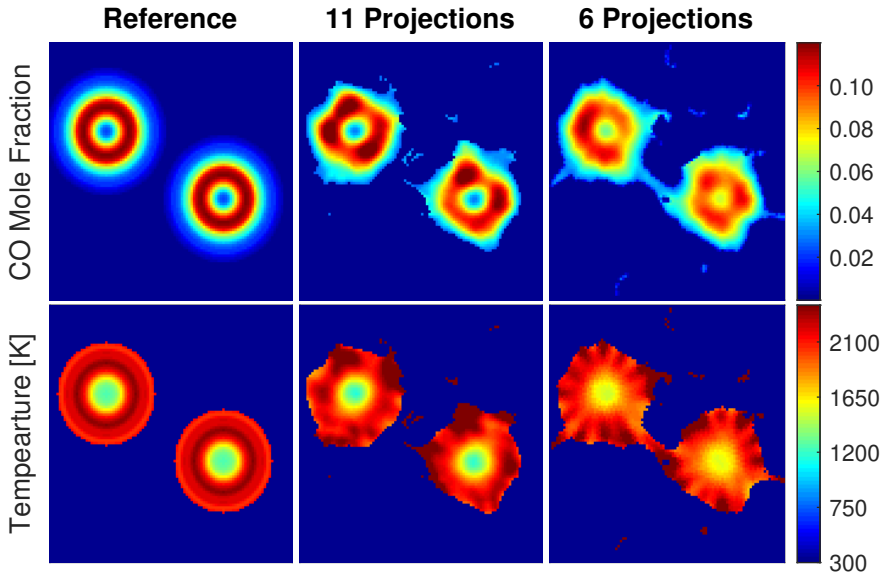

Figure 6.15: Comparison of reconstruction accuracy for mole fraction *(top row)* and temperature *(bottom row)* of the $z = 2.72$ mm horizontal plane of an C_2H_4 flame with 1D Abel inversion as a reference *(left)*.

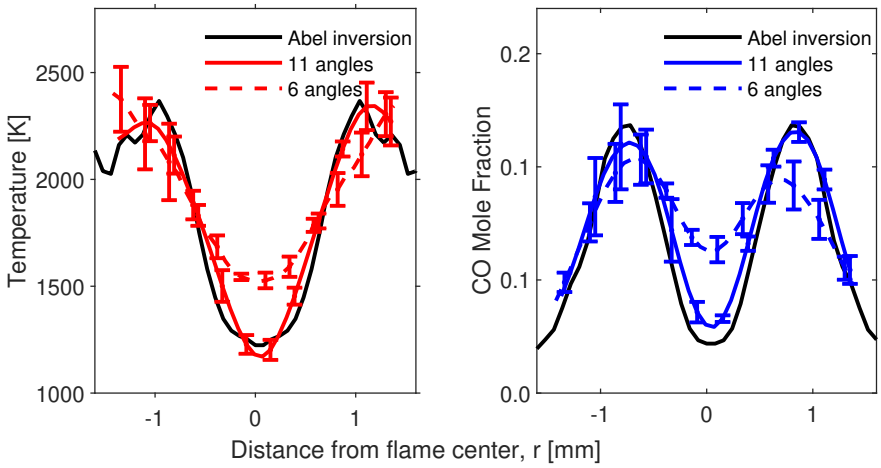

Figure 6.16: One-dimensional radial profiles of temperature *(left)* and CO mole fraction *(right)* generated from different number of projection angles compared to reference profiles generated from the Abel transform.

as better resolve high spatial gradients (including depth of the inner core void) within the flame compared to the result using six projection angles. In both cases, however, the relatively limited number of projection angles caused asymmetry and artifacts in the generated

2D cross-section images.

6.3.3.3 Influence of reconstruction methods

In this section, the 3 methods discussed in section 6.3.2.2 will be further examined by looking at specific 2D and 1D slices. The introduction of 3D regularization not only promotes the smoothness in the vertical direction as shown in the middle of Fig. 6.14, but also improves the resolution of voids and peaks in both temperature and mole fraction as compared to the Abel inverted results in Fig. 6.18. Moreover, by introducing the 3D mask, the artifacts are confined within a smaller spatial region compared to the unmasked regularization methods (2D and 3D) as shown in Fig. 6.14 and Fig. 6.17. As a result, the spatial gradient is further improved —illustrated in Fig. 6.14 and Fig. 6.17 and in more detail in Fig. 6.18—is that the 3D masked Tikhonov regularization using only 6 projection angles resolves the temperature gradient close the the benchmark Abel inversion results.

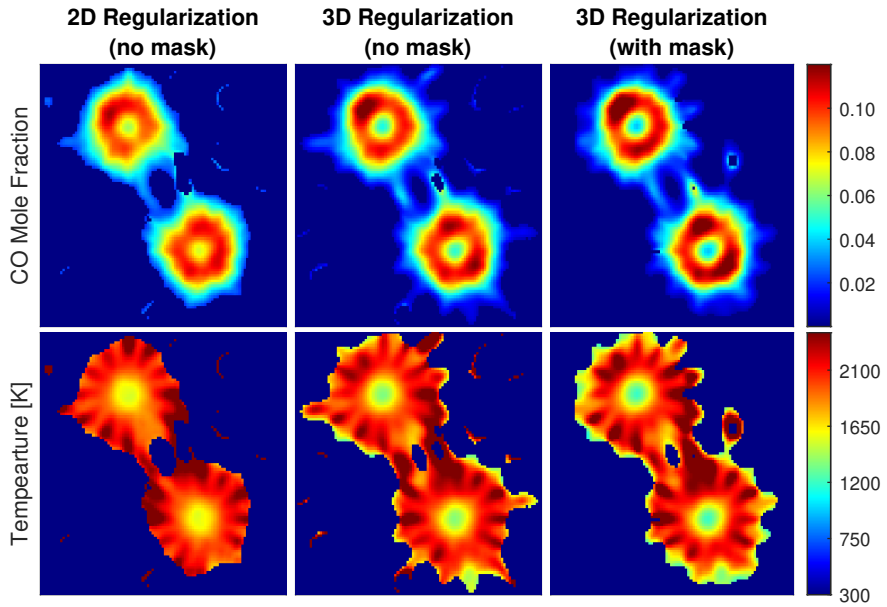

Figure 6.17: Two-dimensional tomographic reconstructions of CO mole fraction *(top)* and temperature *(bottom)* generated from 2D regularization (no mask) *(left)*, 3D regularization (no mask) and 3D regularization (with mask) *(right)*.

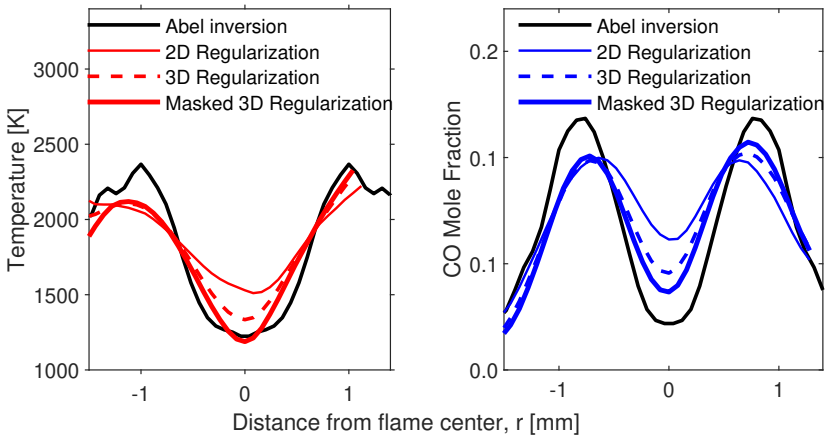

Figure 6.18: One-dimensional radial profiles of temperature *(left)* and CO mole fraction *(right)* generated from 3 linear tomography methods compared to reference profiles generated from the Abel transform.

6.3.4 Conclusions and future work

This work demonstrates the first expansion of the laser absorption imaging (LAI) method to three dimensions, applied to a small-scale dual-flame burner. Simultaneous 2D line-of-sight image capture of the convoluted flow-field across multiple projection angles facilitates 3D reconstruction of mole fraction and temperature fields of the two flames. Reconstructions based on an aggregate 50,688 lines of sight were first performed using linear tomographic methods, highlighting 3D capability of LAI while illuminating challenges associated with the limited-angle tomography. 2D Tikhonov regularization is first applied to form 3D images of temperature and mole fraction by stacking independent cross-section images. Increasing the number of projection has been shown to better resolve the gradient in the flames. 3D Tikhonov regularization has also been applied to enforce connection between vertical planes and promote smoothness in both the horizontal and vertical directions. Finally, a 3D mask is imposed on the flow field volume to further constrain the reconstruction. The introduction of the 3D mask further improve the results in resolving spatial gradients and reducing streak-like artifacts. Based on a benchmark using Abel inversion, the 3D masked Tikhonov regularization using 6 projection angles shows a similar performs to the 2D Tikhonov regularization

using 11 angles. The use of the 3D masked Tikhonov regularization may reduce the number of high-speed IR cameras required and increases the practicality of utilizing time-resolved 3D tomographic LAI for investigations of unsteady, convoluted flame structures.

CHAPTER 7

Laser Absorption Imaging Assisted by Deep Learning: Current and Future Research Directions

The contents of this chapter have been published in the journal ***Optics Letters*** *under the full title 'Deep neural network inversion for 3D laser absorption imaging of methane in reacting flows' [62].*

7.1 Current Research: Deep Neural Network Inversion

7.1.1 Introduction

Mid-infrared laser absorption imaging of methane in flames is performed with a learning-based approach to the limited view-angle inversion problem. A deep neural network is trained with a spectral absorbance model and Radon transform based on superimposed Gaussian field distributions. Prediction capability of the neural network is compared to linear tomography methods at varying number of view angles for simulated fields representative of a flame pair. Experimental 3D imaging is demonstrated on a methane-oxygen laminar flame doublet (<cm) backlit with tunable radiation from an interband cascade laser near 3.16 μm. Spectrally-resolved data at each pixel provides for species-specific projected absorbance. 2D images were collected at 6 different projection angles on a high-speed infrared camera, yielding an aggregate of 27,648 unique lines of sight capturing the scene with a pixel resolution of approximately 70 μm. Mole fraction measurements are inferred from the predicted absorption coefficient images using an estimated temperature field, showing consistency with expected values from reactant flow rates. To the authors' knowledge, this work represents

the first 3D imaging of methane in a reacting flow.

Methane (CH_4) is an important molecule in combustion chemistry, representing the primary fuel component of natural gas and a key intermediate in the oxidation of larger hydrocarbons. Accordingly, quantitative imaging of methane in flame environments is desired to discern the competitive physics of chemical kinetics with mass and heat transport, particularly in the early pyrolysis steps. Some optical methods have shown potential for imaging methane in high-temperature reacting flows, albeit with somewhat constrained applicability. Point and line measurements of CH_4 in flames have been performed with Raman scattering techniques [79]. 2D tomographic measurements have also been conducted via near-infrared diode laser absorption in a semi-conductor process chamber [69]. Here, we present a novel mid-infrared optical method for three-dimensional imaging of methane in high-temperature flame environments.

Advances in mid-wave infrared photonics have enabled tomographic absorption spectroscopy [3] at the fundamental vibrational frequencies of many important combustion species, providing for sensitive thermochemical measurements in small-scale reacting flows using compact low-power light sources [91, 93]. Laser absorption imaging (LAI) is a complimentary optical method developed to capture scenes backlit with tunable laser radiation at very high spatial resolution using high-speed infrared cameras [39, 42, 137]. A representative optical arrangement, used in this work, is shown in Fig. 6.8. Recently, LAI has been successfully coupled with 1D tomography for quantitative imaging of axisymmetric flow-field thermochemistry at sub-100 μm spatial resolution [39, 42].

Tomographic imaging of *non-axisymmetric* flows presents more challenges—multiple projection angles are required to estimate the flow-field scalars, and the inversion problem is underdetermined [3, 59]. Limited view angles often result in a blurring effect and artifacts in the reconstructed flow-field, complicating applications to flames—thermochemical structures characterized by very thin ($\sim$1 mm) reaction zones. Laser absorption tomography efforts in combustion flows have demonstrated different approaches to the inversion problem, including both linear [35, 92, 94, 133] and non-linear [67, 69, 139] methods utilizing various

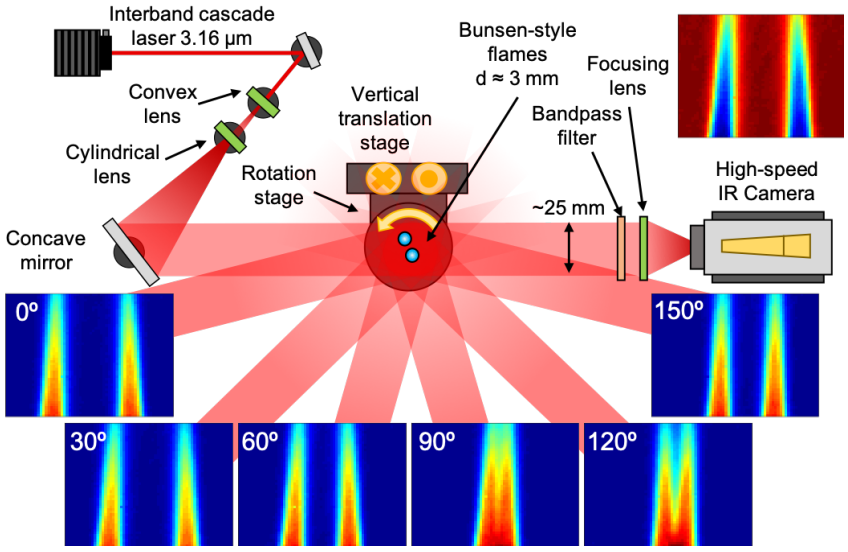

Figure 7.1: Optical setup for this work, showing ICL alignment and transmission image. Inset projected absorbance images of CH_4 shown with respective angle of the Bunsen-style flames.

optical arrangements. Increasingly complex and dense configurations of laser beams (or lines of sight) require computationally efficient image processing methods. Recently, predictive models utilizing neural networks have shown promise to more efficiently solve the inversion problem with limited information, and have been applied to both simulated flows [72] and emission measurements of real flows [19, 73, 74].

Here, we combine a deep neural network inversion with LAI to achieve high-resolution 3D imaging of methane in a non-axisymmetric high-temperature flow field. We compare the deep neural network inversion to linear tomography, assessing performance with regards to accuracy and computational cost, via both simulation and experiment.

7.1.2 Methods

With any tomographic absorption spectroscopy method, the analytical problem reduces to inverting line-of-sight integrated (or projected) absorption data [3, 59]. For a non-uniform gas medium, the Beer-Lambert law integrated over wavenumber ν [cm^{-1}]—or the projected

absorbance area $A_{j,\text{proj}}$ [cm^{-1}]—can be expressed for each line-of-sight in Eq. 6.3:

$$\begin{aligned} A_{j,\text{proj}} &= \int_{-\infty}^{\infty} \alpha(\nu) d\nu = \int_{-\infty}^{\infty} -\ln\left(\frac{I_t}{I_0}\right)_{\nu} d\nu \\ &= \int_0^L K_j dl = \int_0^L P S_j(T) X_{\text{abs}} dl \end{aligned} \tag{7.1}$$

where $\alpha(\nu)$ is spectral absorbance, I_0 is incident light intensity, and I_t is transmitted light intensity. L [cm] is the aggregate path length along the line-of-sight. Thermochemical properties of the non-uniform medium are embedded in the spatially-resolved absorption coefficient K_j [cm^{-2}], where total pressure P [atm] is assumed 1 atm, $S_j(T)$ [cm^{-2}/atm] is the linestrength of rovibrational transition j at temperature T [K], and X_{abs} is the mole fraction. For tomographic LAI, Eq. 7.1 applies to *each* camera pixel, wherein spectrally-resolved absorbance can be integrated to yield 2D images of $A_{j,\text{proj}}$, representative examples of which are depicted in the insets of Fig. 6.8 for different viewing angles. With multiple projection angles, each horizontal row of pixels in each 2D image can be treated independently for subsequent reconstruction of the flow-field scalar K_j. For the experimental setup depicted in Fig. 6.8, we target a collection of rovibrational transitions comprising the R(15) manifold of the v_3 asymmetric stretch band of methane near 3.16 μm. The linestrengths for these transitions do not vary more than 10% for temperatures between 450 and 750 K [142], enabling quantitative inference of mole fraction from K_j in the preheat zone.

In this study, we utilize a deep neural network to perform the inversion of line-of-sight integrated absorption measurements $A_{j,\text{proj}}$ to solve for K_j, and compare its reconstruction performance with linear 2D tomography methods. The training dataset consists of 2D fields of the methane absorption coefficient K_j, represented as superimposed Gaussian distributions as shown in the top of Fig. 7.6. The simulations included 5,000 variations in intensity, size, and relative locations of the Gaussians. The corresponding projected absorbance areas $A_{j,\text{proj}}$ are subsequently calculated utilizing Radon transforms to represent the measurement data at each angle with appropriate pixel density reflecting the LAI experimental setup. Gaussian noise (3%) was applied to the input, enabling the network to learn robust inversion from potentially corrupted measurements. The neural network architecture is adapted from a

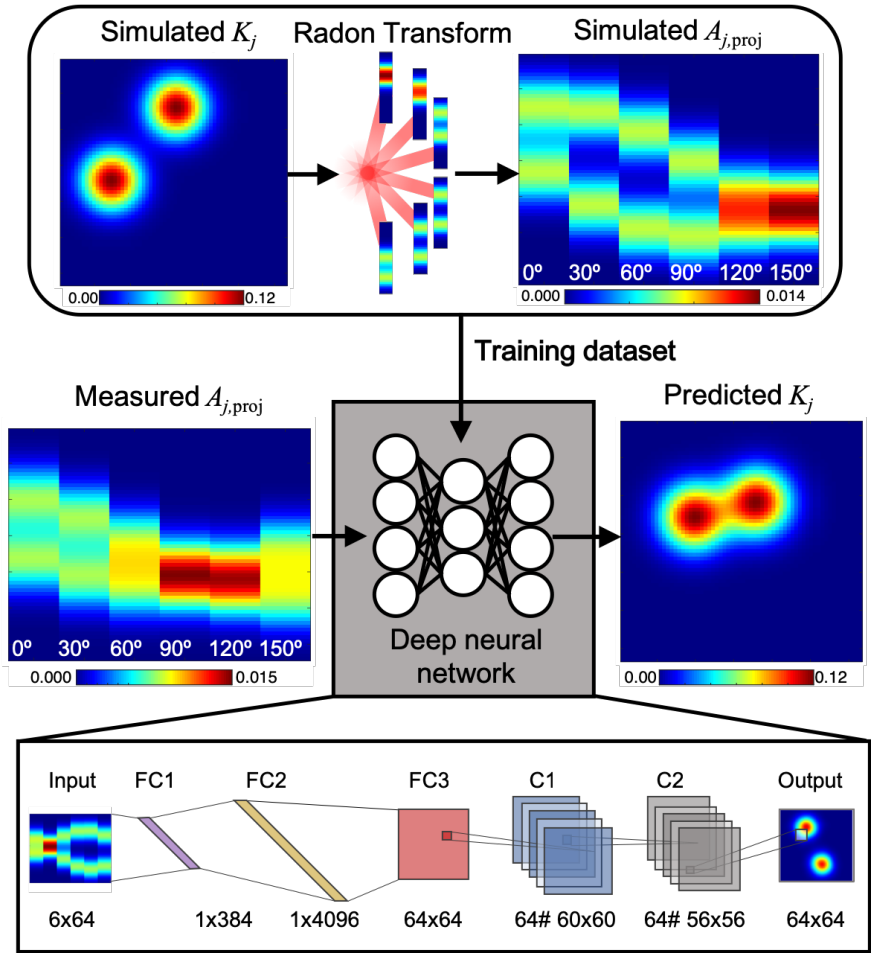

Figure 7.2: Visual representation of deep learning-assisted 2D tomography. *Top:* Forward model of absorption coefficient K_j to projected absorbance $A_{j,\mathrm{proj}}$. *Bottom:* Inversion process predicting K_j from $A_{j,\mathrm{proj}}$ measurements.

unified deep learning framework shown to efficiently reconstruct a variety of imaging fields, including magnetic resonance imaging and X-ray computed tomography [143]. As illustrated in Fig. 7.6, the input layer FC1 takes a measured sinogram of $A_{j,\mathrm{proj}}$ (6×64) of the CH_4 rovibrational transition, reshapes it into a 1×384 vector and then fully connects it to a 1×4096 dimensional hidden layer FC2 with a hyperbolic tangent activation. This hidden layer FC2 is fully connected to another hidden layer FC3 with hyperbolic tangent activation, and is reshaped to a 64×64 matrix for convolutional processing. The convolutional layers C1 and C2 convolve 64 filters of 5×5 with stride 1 followed by rectifier nonlinearities. The final

output layer deconvolves the C2 layer with 64 filters of 7×7 with stride 1, representing the reconstructed K_j field. The loss function minimized during training is an L_2 mean squared loss between the network output and the labeled K_j fields. The RMSprop algorithm is used with minibatches of size 50, learning rate 0.001, momentum 0.0, and decay 0.9. The network was trained for 100 epochs (typically 20–30 mins) on the Tensorflow deep learning framework using an 8 GB NVIDIA RTX 2080 graphics card. Via the training process, an effective inversion operator is learned to predict spatially-resolved 2D K_j. This bypasses the numerical inversion of $A_{j,\text{proj}}$ to K_j obtained through conventional tomography methods.

7.1.3 Numerical Validation

To assess the predictive accuracy of the deep learning inversion method on a flame pair, the approach is applied to reconstruct reference simulations of representative 2D K_j fields using various numbers of projection angles, as shown in Fig. 7.3. These reference 2D K_j fields and

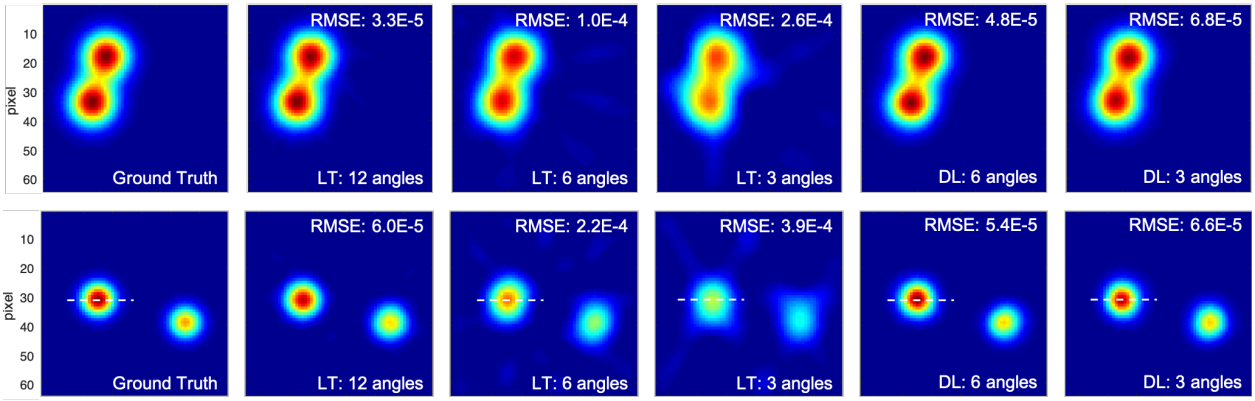

Figure 7.3: Comparison of linear tomography (LT) and deep learning (DL) reconstruction methods with two representative test cases (Ground Truth) of K_j fields. Dashed lines indicate cross-sections examined further in Fig. 7.5.

their associated $A_{j,\text{proj}}$ projections are not part of the original training set, and so serve as an independent reconstruction assessment. Tikhonov-regularized linear 2D tomography is also applied to the reference fields. The regularization parameter λ and the smoothing matrix

L are chosen according to a previous study [59], yielding a value of λ that pads the small singular values but does not overwhelm the large non-trivial singular values. An aggregate root-mean-square error (RSME) was used as a comparative metric, calculated as the square root of the averaged squared differences between a reconstructed image and its corresponding "ground truth" image.

As expected, utilizing a greater number of projection angles was shown to improve the resolution of peaks and valleys in the reconstructed K_j fields for both methods. The deep learning approach is shown to predict the steep spatial gradients with equal or greater accuracy (as measured by RMS error) than linear tomographic methods while concurrently reducing the required number of projections, even in the cases where the K_j fields overlap. Nonphysical absorption artifacts are also observed in the linear tomographic reconstructions outside of the simulated reaction zones, a common consequence of the underdetermined inversion [59]. Notably, the linear tomographic methods show increasing reconstruction error when the pixel density per flame structure is reduced, as in the smaller flames in the bottom row of Fig. 7.3. The neural network inversion appears less sensitive to the pixel density, showing a typical reduction in RMSE by a factor of $\sim$4–6 relative to corresponding linear tomographic solutions. We can observe for the experimentally-relevant test case (bottom row), the learning-based approach utilizing 3 projection angles has a RSME only 10% greater than the linear tomographic approach utilizing 12 projection angles.

7.1.4 Experimental Results

With the deep learning approach tested via simulation, the neural network inversion was utilized for measurements of the flame doublets shown in Fig. 6.8. A distributed feedback (DFB) interband cascade laser (ICL) near 3.16 μm is used to spectrally scan across the CH_4 R(15) manifold. The beam is expanded twice; first with a concave lens, and again horizontally with a cylindrical lens. The expanding beam is re-collimated with a concave mirror, then pitched through the flow-field comprising two Bunsen-style flames, each with flame brushes approximately 3 mm in diameter. The beam is spectrally isolated with a bandpass filter

(Spectrogon, 3160 ± 60 nm), and a plano-convex lens focuses the expanded beam onto the detector array of the camera. The beam is captured in the camera detector subwindow of size 64×48 with a frame rate of 40 kHz and integration time of 5 μs. The laser is injection-current tuned using a sawtooth waveform at 400 Hz, resulting in 100 points per scan for both I_0 and I_t for each pixel. The spectrally-resolved absorbance $\alpha(\nu)$ is determined using Eq. 6.3 and is subsequently fitted using the Voigt lineshape model to obtain the projected absorbance area $A_{j,\text{proj}}$. For each projection angle measurement, data are collected and averaged over 1 second (400-scan average), an interval over which the flames are assumed steady. Spatial resolution was evaluated by imaging a wire mesh with known dimensions backlit with laser radiation [42], and was determined to be approximately 70 μm per pixel in the horizontal direction.

The flame pair is mounted on a rotational stage to image the flow-field from a variety of angles, as shown in Fig. 6.8. The partially premixed flames were controlled via thermally-based mass flow controllers (MKS MFC GE50A) with combined reactant flow rates of 150 sccm CH_4 and 100 sccm O_2. This corresponds to a fuel-rich mixture with a molar fuel-air equivalence ratio of $\phi \approx 3$. After the flows are split to the two burners, one flow is measured with a rotameter to ensure equal flow through each burner. The exit velocity of each flow is 0.33 m/s and the jet exits of the stainless steel burners are 1.6 mm in diameter, providing a laminar jet Reynolds number of ∼36.

For each horizontal row of pixels in the measured 2D $A_{j,\text{proj}}$ images, the learning-based inversion operator is applied to predict the K_j field distribution for the R(15) manifold of CH_4. Assembling the predictions for each horizontal row, a 3D field of K_j is obtained, as shown in Fig. 7.4. Learning-based predictions utilizing six projection angles of 2D $A_{j,\text{proj}}$ images are shown alongside corresponding results obtained using 2D linear tomography. The images are self-consistent in reconstruction of the twin flames, exhibiting similar heights, widths, and magnitudes. However, the flames diverge in magnitude and diameter when comparing the deep learning and linear tomography results. Steeper spatial gradients of K_j are resolved within the reacting flow utilizing the learning-based approach, and this is

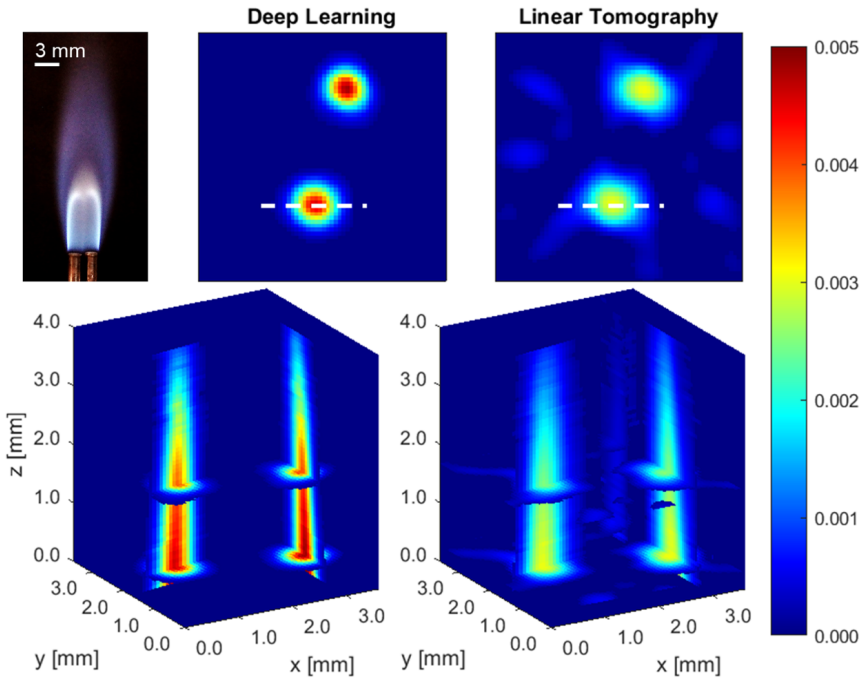

Figure 7.4: Photograph of flames and 3D K_j fields reconstructed from six projection angles using the learning-based approach described by Fig. 7.6 (left) and linear 2D tomography (right). Dashed lines indicate cross-sections examined further in Fig. 7.5.

seen more clearly in the 2D cross-sections in the top of Fig. 7.4. As in the simulations, the learning-based approach also mitigates image artifacts and angular asymmetry around the flame observed in the results of the linear tomographic method.

Reconstruction performance of both the linear tomography and neural network inversion is examined in further detail with 1D profiles shown in Fig. 7.5. The left of Fig. 7.5 compares 1D cross-sectional profiles of K_j reconstructions obtained from both linear tomography and deep learning in relation to the "ground truth" for the simulated K_j field indicated in Fig. 7.3. The uncertainty shown associated with each reconstruction is calculated by performing the reconstructions with different flow-field orientations [44]. Though a "ground truth" for the reconstructed K_j fields determined from the experimental measurements is unknown, an analogous comparison can be made for the experimental K_j fields at the base of the flames nearest the burner surface, indicated by Fig. 7.4. Given an independently

measured or estimated temperature field, Eq. 6.3 can be used to obtain a mole fraction field for CH_4. The right of Fig. 7.5 shows the resulting 1D profiles of CH_4 mole fraction assuming a uniform temperature of 450 K (based on a thermocouple measurement at burner exit). While the temperature in this plane is certainly not uniform, the CH_4 absorption line strength exhibits relative insensitivity to temperature—Error bars capture a possible temperature range between 400 K and 750 K. While the edges of the fuel distribution may be hotter, this simplified analysis provides clear indication that the mole fraction at the core of the flame ($X_{CH_4} \approx 0.59$) is more closely estimated by the neural network inversion, even with only 3 imaging angles.

Lastly, it should be noted that the learning-based approach reduces computational load considerably compared to linear tomography with Tikhonov regularization. Although the neural network requires a 20–30 min training process as mentioned, once the networks are established, the reconstructions are more computationally efficient: On an Intel(R) Core(TM) i7-9700K 3.60 GHz CPU, the neural network completed reconstructions in 0.35 s while linear

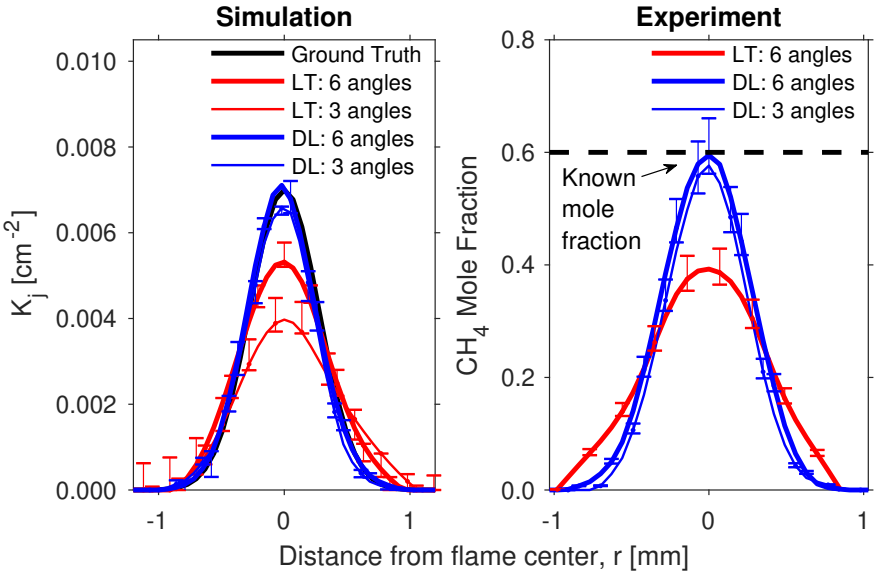

Figure 7.5: 1D profiles of simulated K_j noted in Fig. 7.3 (left) and CH_4 mole fraction calculated with experimental K_j shown in Fig. 7.4 using temperature measured at burner exit (right).

tomography took ∼40 s.

7.1.5 Conclusion

A deep learning approach to the inversion problem for absorption tomography was coupled with a high-resolution LAI configuration for 3D species imaging, and evaluated by simulation and experiment. To the authors' knowledge, the experimental effort represents the first 3D imaging of methane in a flame, attaining a spatial resolution on the order of 70 μm.

7.2 Future Research on LAI

7.2.1 Physics-Trained Deep Neural Network Inversion

The current work of this dissertation demonstrates that deep learning inversion has potentials to more accurately resolve flame structure with fewer projection angles than linear tomography. However, the perform of the deep neural network strongly depends on the draining dataset. Extension of this method to more complex flame structures may require more sophisticated simulations to generate appropriate training data. While the distribution of the fuel structures can be well-approximated by purely mathematical Gaussian distributions, turbulent flow structures and intermediate or product fields likely require more physical representations.

Here we describe a physics-trained deep neural network approach to the inversion problem, depicted in Fig. 7.6, that takes advantage of our prior knowledge of combustion physics, the experiment, spectroscopic models, and our knowledge of the forward projection process. In this approach, temperature and concentration field data are generated utilizing the results of 1D opposed-flow flame simulations in Cantera. Approximately 3500 flames are produced by varying fuel-side (C_2H_6/O_2-enriched air) and oxidizer-side (ambient air) mass flux rates, CO and CO_2 fuel-side concentration, and fuel-side equivalence ratio using a 3 mm domain. 5000 training examples and 1000 validation examples are generated by randomly choosing the 1D calculations and projecting species and temperature profiles into two axi-

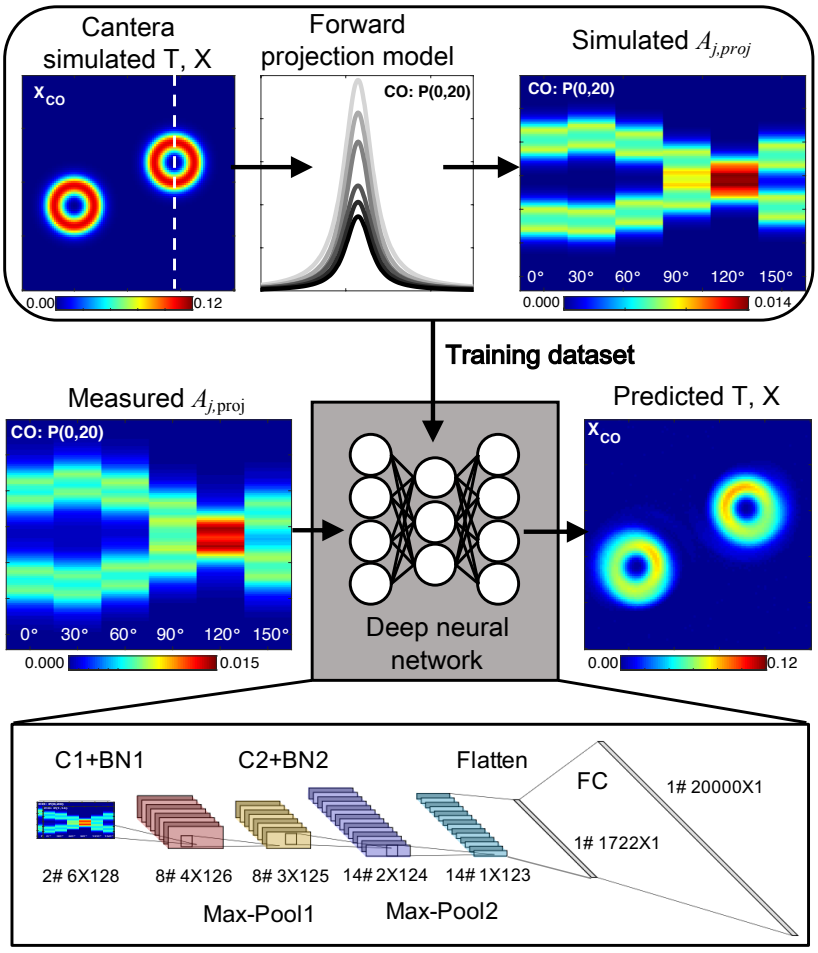

Figure 7.6: Visual representation of deep learning-assisted 2D tomography. *Top:* Training dataset development from Cantera-simulated thermochemical profiles to spectral simulations. *Bottom:* Process of predicting thermochemical profiles from measurements.

symmetric flows on a grid with estimated center locations allowing ±0.4 mm variation in both x and y, as shown in the top left of Fig. 7.6. Spectral simulations are performed in each grid cell to simulate K_j fields, after which a forward projection using Eq. 6.4 is applied to calculate path-integrated line-of-sight projections $A_{j,\text{proj}}$, depicted as sinograms in the top right of Fig. 7.6. The CANTERA-generated data are used as a labeled dataset to train the neural network. The design of the convolutional neural network (CNN) architecture used in this study is adapted from the works of others [19, 72]. As illustrated in the bottom of Fig. 7.6, the input to the neural network comprises 2 sinograms (6×128) from each CO

spectral transition. The first convolutional layer C1 convolves 8 filters of 3×3 with stride 1 followed by a rectifier nonlinearity, a batch normalization layer BN1, and a max pooling layer with filters of 2×2. The second convolutional layer C2 similarly convolves 14 filters of 2×2 with stride 1 followed by a rectifier nonlinearity, a batch normalization layer BN2, and a max pooling layer with filters of 2×2. After a flatten layer and a fully connected layer FC, an output vector of size 20000×1 is obtained, which can easily be reshaped as two 100×100 2D profiles of temperature and CO mole fraction, respectively. The loss function minimized during training was a simple mean squared loss between the network output and target normalized temperature and CO mole fraction values. The RMSprop algorithm is used with minibatches of size 50, learning rate 0.001, momentum 0.0, and decay 0.9. The network was trained for 100 epochs (typically 20–30 mins) on the Tensorflow deep learning framework using an 8 GB NVIDIA RTX 2080 graphics card.

After the training process finishes, an effective inversion operator with physical priors on combustion chemistry and flame symmetry is learned, and can be applied to new path-integrated measurements to reconstruct the temperature and concentration fields. This effectively bypasses the inversion of $A_{j,\mathrm{proj}}$ to K_j obtained through Eq. 6.6, as well as the two-line thermometry, and directly results in thermochemical profiles of the flow-field.

Representative mole fraction results of the physics-based deep learning implementation on measurements from C_2H_4 flames are shown in Fig. 7.7 using both six and three projection angles. As with the linear tomography results, high spatial gradients are resolved within the flames, and the magnitudes closely resemble those of the reference profile. Additionally, this approach mitigated image artifacts and angular asymmetry around the flame associated with limited numbers of projection angles in linear tomographic methods. A noteworthy advantage—illustrated in Fig. 7.7 and in more detail in Fig. 7.8—is that even when the number of projection angles is reduced from six to three, the 3D reconstruction still retains the majority of the CO mole fraction structure within the flames and closely predicts reference magnitudes, albeit with some inaccuracies. Fig. 7.8 compares 1D radial profiles of temperature and CO mole fraction for a single flame in the flow, obtained from both lin-

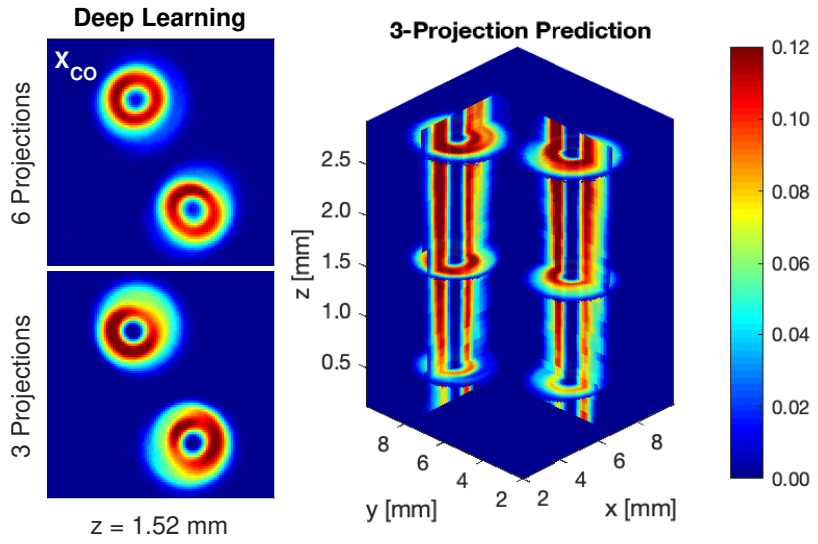

Figure 7.7: *Left:* Deep learning-assisted tomographic reconstructions of CO mole fraction using six and three projection angles. *Right:* three-dimensional results utilizing three projection angles.

ear tomography and deep learning in relation to the reference profiles discussed previously. While both methods produce generally similar temperature profiles with the same number of projections, the implementation of deep learning enables improved reconstruction of CO mole fraction profiles with six projection angles. The CNN method was also able to predict thermochemical profiles beyond the domain contrained by the analytical solution. Furthermore, it was found that a set of opposed-flow flame simulations utilizing C_2H_6 as the fuel was a generalized enough training set to be used for all flames in this study, demonstrating adaptive capability of the neural network.

Lastly, it should be noted that CNN provides a considerable computational advantage over linear tomography with Tikhonov regularization. Although CNN requires a 20–30 min training process as mentioned, once the networks are established the subsequent reconstructions are computationally efficient. When implemented on an Intel(R) Core(TM) i7-9700K 3.60 GHz CPU, CNN completed reconstructions of all pixel rows in ∼1 s while linear tomography took ∼400 s.

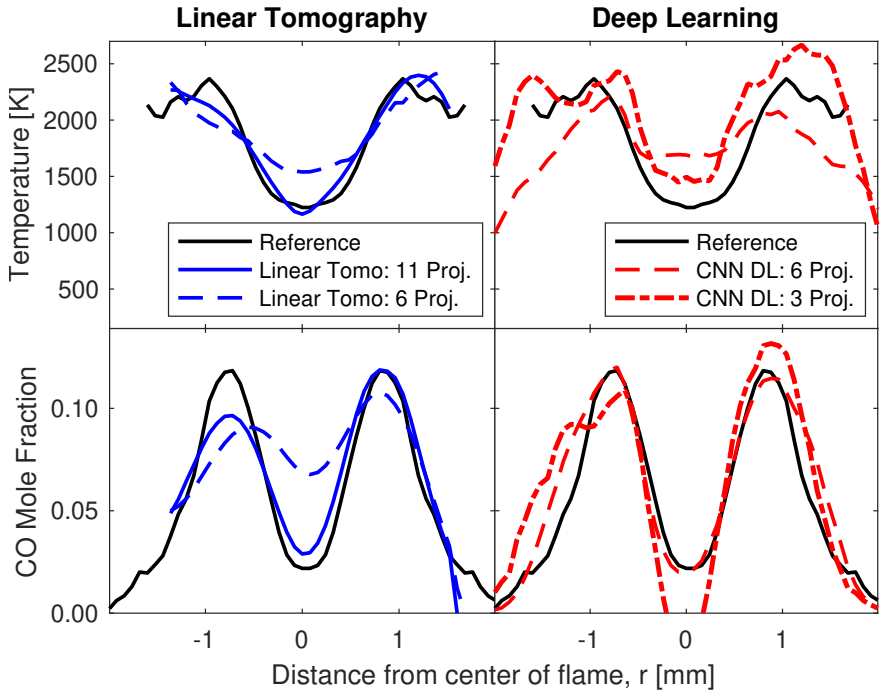

Figure 7.8: One-dimensional radial profiles of temperature *(top)* and CO mole fraction *(bottom)* generated from linear tomography *(left)* and deep learning *(right)* compared to reference profiles generated from the Abel transform.

7.2.2 Time-resolved 3D LAI

Most of the work in this dissertation for LAI has been focused on steady flows due to the number of camera available and the frame rate of the infrared cameras. However, the tomographic reconstruction methods developed in this dissertation are directly applicable for multi-camera measurements. In a recent work by the author, laser absorption imaging is expanded in temporal resolution capability to kHz measurement rates by coupling sparsely-sampled wavelength-scanning and digital image post-processing for diffraction correction [137]. This work combined with the tomographic reconstruction techniques presented in this dissertation set the foundation for future time-resolved 3D tomographic imaging research.

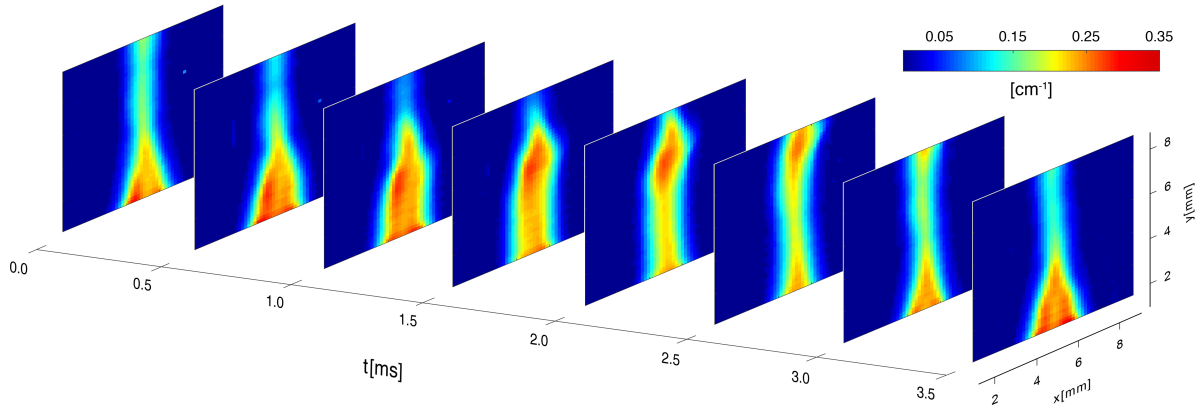

Figure 7.7: *(left to right)* Sequential images of C_2H_6 $^RQ_3$ line-of-sight absorbance areas [cm^{-1}] captured at 2 kHz.

APPENDIX A

Uncertainty Analysis

In this work, we report values of species concentration and temperature, but it is important to note the uncertainty in these values due to factors associated with the LAT measurement technique. We follow the uncertainty analysis presented in previous work [32], with added analysis in this work to account for uncertainty associated with tomographic reconstruction [38]. For Eqs. 6.3 and 5.2 as well as those in this section (unless otherwise noted), we follow the Taylor Series Method (TSM) of uncertainty propagation [144], in which the uncertainty of a variable r, Δr, is given by:

$$(\Delta r)^2 = \left(\frac{\partial r}{\partial x_1}\Delta x_1\right)^2 + \left(\frac{\partial r}{\partial x_2}\Delta x_2\right)^2 + \cdots \tag{A.1}$$

where x_i are dependent variables and Δx_i are their respective uncertainties. As indicated by Eq. 5.2, mole fraction of an absorbing species $X_{abs}(r)$ depends on linestrength $S_j(T(r))$ and reconstructed absorption coefficient $K_j(r)$. In turn, $S_j(T(r))$ depends on temperature $T(r)$, which—for the two-line thermometry techniques employed here—depends on $R(r)$, which is also dependent on $K_j(r)$. Here, discuss the propagation of uncertainty from initial intensity measurements I_t and I_0 through these equations to obtain uncertainty in $T(r)$ and $X_{abs}(r)$.

The systematic error in I_t and I_0 is assumed to be the same because the same system is used to measure both signals; thus the only uncertainty considered for each of these signals is the random uncertainty among all the scans averaged within a spatial segment dr (in this case, the distance associated with 105 direct-absorption scans). For each spatial segment, the standard deviations of both the incident background I_0 and the absorbance signals I_t are calculated, which are both used to determine the 95% confidence interval of the signals, represented by ΔI_0 and ΔI_t. To obtain the variation *specifically in absorbance*,

$\Delta\alpha_\nu$, we subtract ΔI_0 from ΔI_t and use the resulting value as a bounds on absorbance signal, $I_t \pm (\Delta I_t - \Delta I_0)$. We then calculate the resulting variation in α_ν, $\Delta\alpha_\nu$, by propagating the uncertainty in the Beer-Lambert law [1]. In turn, $\Delta A_{j,proj}(r)$ is calculated by propagating the uncertainty $\Delta\alpha_\nu$ in Eq. 6.3, generating an upper and lower bound on $A_{j,proj}(r)$. This process occurs for each spatial interval dr across the radius of the burner r.

The uncertainty in $K_j(r)$, $\Delta K_j(r)$, is determined numerically via tomographic reconstruction of the upper and lower bounds of $A_{j,proj}(r)$. Also included in $\Delta K_j(r)$ is the uncertainty associated with the location of the centerline assumed in the Abel inversion ($r = 0.0\pm0.5$ mm), which significantly effects the reconstructed mole fraction values in the core relative to the edges of the flow [38]. Applying Eq. A.1 to the ratio of the two absorption coefficients $K_j(r)$, we can calculate the uncertainty in $R(r)$, $\Delta R(r)$:

$$\left(\frac{\Delta R(r)}{R(r)}\right)^2 = \left(\frac{\Delta K_A(r)}{K_A(r)}\right)^2 + \left(\frac{\Delta K_B(r)}{K_B(r)}\right)^2 \tag{A.2}$$

In the results presented in this study, the ratio $R(r)$ is used to determine temperature $T(r)$ by correlating $R(r)$ to simulations of $R(T) = S_A(T)/S_B(T)$ created using Eq. A.5, which is shown later. An explicit expression revealing the uncertainty dependencies in temperature can be derived via the following analytical expression for temperature $T(r)$:

$$T(r) = \frac{\frac{hc}{k_B}\left(E''_B - E''_A\right)}{\ln\left(R(r)\right) + \ln\left(\frac{S_B(T_0)}{S_A(T_0)}\right) + \frac{hc}{k_B}\frac{(E''_B - E''_A)}{T_0}} \tag{A.3}$$

Here, h [J·s] is the Planck constant, c [cm/s] is the speed of light, k_B [J/K] is the Boltzmann constant, and E''_j [cm^{-1}] is the lower-state energy for the two lines A and B. Since $T(r)$ is a function of $R(r)$, there is an associated uncertainty in temperature, $\Delta T(r)$. Using Eq. A.1 on Eq. A.3, $\Delta T(r)$ is given by:

$$\frac{\Delta T(r)^2}{T(r)^2} = \frac{\left(\Delta R(r)/R(r)\right)^2}{\left(\ln\left(R(r)\right) + \ln\left(\frac{S_B(T_0)}{S_A(T_0)}\right) + \frac{hc}{k_B}\frac{(E''_B - E''_A)}{T_0}\right)^2} \tag{A.4}$$

When the mole fraction $X_{\text{abs}}(r)$ of the species approaches zero, both absorption coefficients $K_j(r)$ will also approach zero, and $R(r)$ will become highly sensitive to noise or error in either reconstruction of $K_j(r)$. This can lead to unreasonably high or low temperatures in

regions where the signal-to-noise ratio of $K_j(r)$ is low (SNR < 5), and so we do not include those regions in the plots shown. As mentioned, $S_j(T(r))$ is function of $T(r)$ [1]:

$$S_j(T) = S_j(T_0)\frac{Q(T_0)}{Q(T)}\frac{T_0}{T}\exp\left[-\frac{hcE_j''}{k_B}\left(\frac{1}{T}-\frac{1}{T_0}\right)\right]\left[1-\exp\left(-\frac{hc\nu_{0,j}}{k_BT}\right)\right]\left[1-\exp\left(-\frac{hc\nu_{0,j}}{k_BT_0}\right)\right]^{-1} \tag{A.5}$$

where it is understood that T is $T(r)$. Q is the partition function for the internal energy modes of the molecule. Therefore, $\Delta T(r)$ (from the uncertainty in $\Delta R(r)$) affects $S_j(T(r))$ that is used to calculate mole fraction. The following expression can be obtained for the uncertainty in linestrength due to uncertainty in observed temperature, $\Delta T(r)$:

$$\Delta S_{j,T}^2(T) = S_j^2(T)\Delta T^2\left(-\frac{\partial Q(T)/\partial T}{Q(T)}-\frac{1}{T}+\frac{hcE_j''}{k_BT^2}+\frac{hc\nu_{0,j}}{k_BT^2}\left(\frac{\exp\left(-hc\nu_{0,j}/k_BT\right)}{1-\exp\left(-hc\nu_{0,j}/k_BT\right)}\right)\right)^2 \tag{A.6}$$

Additionally, the HITRAN database reports inherent uncertainty in $S_j(T_0)$, which we refer to here as $\Delta S_j(T_0)$. Thus, the total uncertainty in linestrength can be calculated:

$$\Delta S_j^2(T) = \Delta S_{j,T}^2(T) + \Delta S_j^2(T_0) \tag{A.7}$$

Now, mole fraction is given by:

$$X_{\text{abs}}(r) = \frac{K_j(r)}{S_j(T(r))P} \tag{A.8}$$

Utilizing Eq. A.1, the uncertainty in mole fraction, excluding uncertainty in total pressure P, is:

$$\left(\frac{\Delta X_{abs}(r)}{X_{abs}(r)}\right)^2 = \left(\frac{\Delta K_j(r)}{K_j(r)}\right)^2 + \left(\frac{\Delta S_j(T(r))}{S_j(T(r))}\right)^2 \tag{A.9}$$

Thus, the uncertainties in $\Delta K_j(r)$ and $\Delta S_j(T(r))$ are accounted for.

APPENDIX B

Laser Absorption Imaging: Practical Issues

This appendix is intended to cover a number of practical issues with mid-infrared laser absorption imaging that are mostly omitted from the preceding chapters. As mentioned before, the current dissertation presents the first application of the high-speed infrared camera in laser absorption tomography measurements. While infrared cameras have mostly been utilized to measure emissions (incoherent light) from the scene, the application to image coherent laser beam for combustion diagnostics in the current work poses unique issues and challenges. Some of these challenges include: camera pixel saturation, diffraction induced noises, and beam collimation. A few of the issues and some practical solutions are discussed here.

B.1 Camera Parameters

Most infrared cameras are designed to highly sensitive to infrared radiations. Collimated laser beam often contains much higher power than ambient emissions and therefore laser light needs to be attenuated before imaged by the camera pixels. In addition, parameters such as integration time and frame rate should be chosen carefully. This section discusses some important camera parameters and their determination during the laser absorption measurements.

B.1.1 Integration and Transfer Time

The **exposure/integration time** represents the time during which the camera sensor accumulates charges, induced by incident photons coming from the scene. The integration time can be preset manually or can be automatically adjusted by the camera software. A higher integration time will increase the signal level but may saturate the camera pixel and smear the transient process. The **transfer time** designates the time needed by the sensor electronics to read the pixels of the sensor array.

B.1.2 Frame Rate

The **frame rate** is the frequency (rate) at which consecutive images (frames) are recorded (sampled). The attainable detector frame rate is dependent on the integration time and the transfer time (or readout time). Figure B.1 shows the relative relations between the integration time, transfer time, and frame rate.

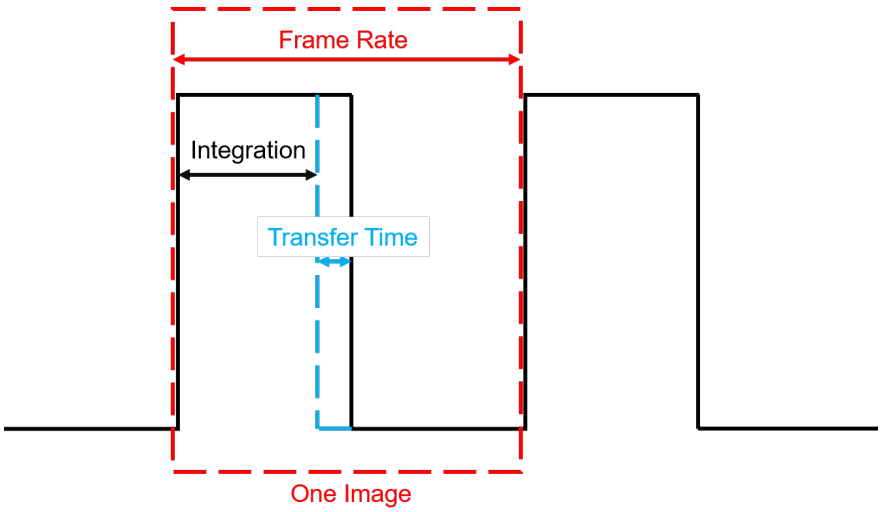

Figure B.1: Image acquisition terminology

B.1.3 Window Size

The **window size** defines the number of pixels activated during the acquisition and the aspect ratio of the image. Frame rate, window size, and exposure time are three parameters that influence each other since they must globally respect the limits of the camera data throughput capabilities. If a parameter is restricted from reaching the desired value, one or the two others must be decreased before trying to set parameters again (to lower the data throughput). Some typical values for these parameters for a Telops FAST-M3K camera is shown in B.1.

Table B.1: Selected Telops FAST-M3K image capture options

Width [px]	Height [px]	Max framerate [kHz]
64	4	95.2
64	32	44.9
64	64	28.0
128	128	10.8
320	256	3.1

B.2 Diffraction Artifacts

One main challenge associated with performing mid-IR LAI with coherent laser light is the diffraction-induced Airy-disk patterns as shown in Figure B.2. Spatial diffraction effects such as these are often caused by stray particles in the path of the beam, circular apertures cutting the enlarged beam, or other sources that are difficult to isolate in an optical system. Pronounced oscillations in signal intensity caused by the wavelength-dependent diffraction is often observed as schematically shown in the bottom of Figure B.2 [42, 137]. These oscillations, if not handled properly, will eventually lead to spatially dependent errors in the measured gas properties.

Several methods, both through optical design and digital postprocessing, haven been ap-

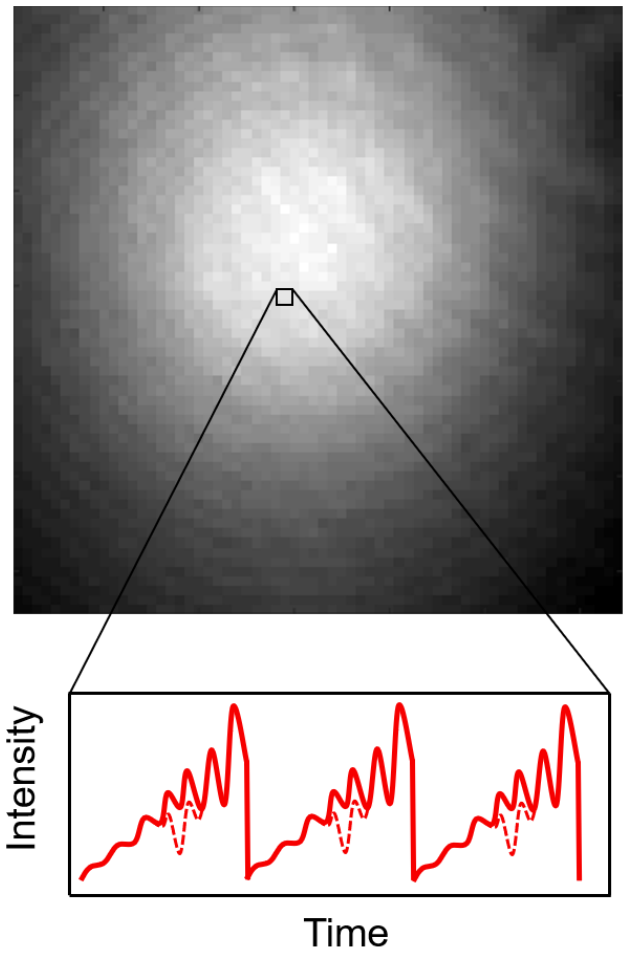

Figure B.2: *Top*: Image of coherent laser light with Airy-disks. *Bottom*: Single-pixel time-history illustrating how diffraction-induced oscillations vary in time.

plied and proven efficient in metigating diffraction-induced noises. One approach to avoiding these diffraction-induced image artifacts is to destroy the coherence in the laser light by reflecting the beam off spinning diffusers [42]. This optical solution successfully eliminated diffraction patterns at the cost of added intensity noise, that required averaging and reduced temporal resolution (∼Hz). Alternatively, the diffraction-induced image artifacts can be filtered out in the Fourier domain through digital postprocessing without sacrificing temporal resolution but at a cost of reduced spatial resolution [137]. Lastly, it is also observed that beam shaping using cylindrical optics not only produces a uniformly distributed signal intensities across the camera pixels but also helps reduce the diffraction artifacts.

B.3 Beam Collimation

In this dissertation, the line-of-sight measurements are modeled as parallel-beam tomography problem and therefore the expended laser beam should be collimated when imaged into camera pixel array to minimize modeling error. In the LAI systems, the laser beam, even though is collimated coming out the laser, can become uncollimated after beam expension. It is then important to make sure the beam is collimated during the optical alignment process. To check the beam collimation, one can image a calibration grid in the focal plane as shown in Figure B.3. If the image is not distorted when moving the mesh away from the focal plane (along the direction of the line-of-sight), the laser beam is collimated.

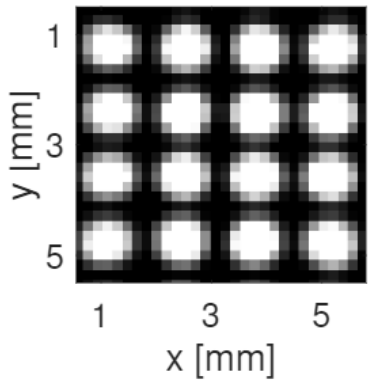

Figure B.3: Image of a calibration mesh backlit with infrared laser light.

APPENDIX C

Sample Data Processing Codes

This appendix provides some example codes used in the dissertation, including Matlab functions for generating 2D and 3D regularization matrices, 3D mask and Python codes for deep neural network inversion. For flexible tomographic reconstruction, more open source toolboxes are available, such as TomoPy, the ASTRA toolbox, and TIGRE. Prof. Per Christian Hansen from Technical University of Denmark developed a series of Matlab softwares for regularization of discrete ill-posed problems, such as AIR Tools II, IR Tools and TVReg.

C.1 Generate Laplacian differential operator for 2D grid

The goal in this section is to generate a sparse matrix for the discrete gradient operator used in Tikhonov regularization for a 2D grid:

$$\frac{\partial u}{\partial x} + \frac{\partial u}{\partial y} = f(x, y) \tag{C.1}$$

The Laplacian operator using first order standard differences results in:

$$\left(\frac{4u_{i,j} - u_{i-1,j} - u_{i+1,j} - u_{i,j-1} - u_{i,j+1}}{4h} \right) = f_{i,j} \tag{C.2}$$

where h is the grid size.

This can be wiritten in the form of $\mathbf{L}u = f$, where the matrix $\mathbf{L}$ can be generated using the following Matlab function:

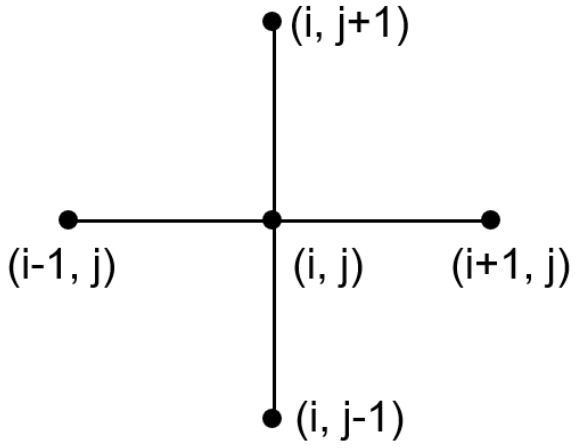

Figure C.1: 2D grid points.

```
function L2 = L2D(nx,ny)
% generate sparse matrix for 2D Laplacian matrix
% based on the code by Nasser M. Abbas
% INPUT:
%   nx : Number of internal grid point along x-axis.
%   ny : Number of internal grid point along y-axis.
%        Hence, there are N = nx*ny grid points
% OUTPUT:
%     A: the 2D discrete Laplacian operator
%
% Chuyu Wei May, 2020

ex = ones(nx,1);
Lx = spdiags([ex -2*ex ex],[-1 0 1],nx,nx);
ey = ones(ny,1);
Ly = spdiags([ey -2*ey ey],[-1 0 1],ny,ny);

Ix = speye(nx);
Iy = speye(ny);
L2  = -(kron(Iy,Lx)+kron(Ly,Ix))/4;

end
```

C.2 Generate Laplacian differential operator for 3D grid

The goal in this section is to generate a sparse matrix for the discrete gradient operator for a 3D grid:

$$\frac{\partial u}{\partial} + \frac{\partial u}{\partial y} + \frac{\partial u}{\partial z} = f(x, y, z) \tag{C.3}$$

To form a matrix operator, the equation can be rearranged as following:

$$\frac{1}{6h}\left(6U_{i,j,k} - U_{i-1,j,k} - U_{i+1,j,k} - U_{i,j-1,k} - U_{i,j+1,k} - U_{i,k,k-1} - U_{i,j,k+1}\right) = f_{i,j,k} \tag{C.4}$$

where h is the grid size.

This can be wiritten in the form of $\mathbf{L}u = f$, where the matrix $\mathbf{L}$ can be generated using the following Matlab function:

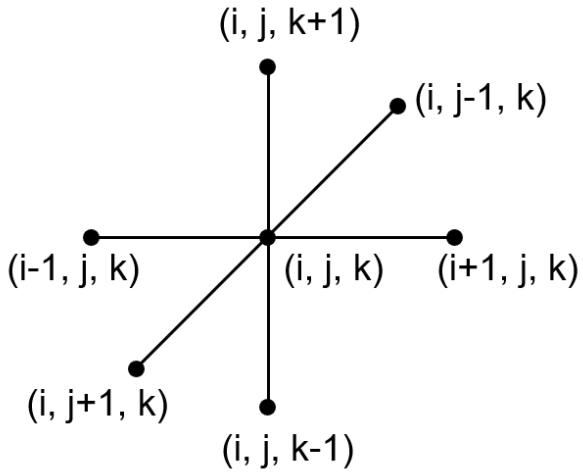

Figure C.2: 3D grid points.

```
function L3 = L3D(nx,ny,nz)
% generate 3D sparse matrix for 3D Laplacian matrix i
% based on the code by Nasser M. Abbas
% INPUT:
%   nx : Number of internal grid point along x-axis.
%   ny : Number of internal grid point along y-axis.
%   nz : Number of internal grid point along z-axis.
%        Hence, there are N = nx*ny*nz grid points
% OUTPUT:
%     A: the 3D discrete Laplacian operator
%
% Chuyu Wei May, 2020
ex = ones(nx,1);
Lx = spdiags([ex -3*ex ex],[-1 0 1],nx,nx);
ey = ones(ny,1);
Ly = spdiags([ey -3*ey ey],[-1 0 1],ny,ny);

Ix = speye(nx);
Iy = speye(ny);
L2 = kron(Iy,Lx)+kron(Ly,Ix);

N  = nx*ny*nz;
e  = ones(N,1);
L  = spdiags([e e],[-nx*ny nx*ny],N,N);
Iz = speye(nz);

L3 = - (kron(Iz,L2)+L)/6;
end
```

C.3 3D Mask

The code in this section is to imposed a 3D mask in the reconstruction volume:

```
% generate 3D mask in the reconstruction volume
%
% Chuyu Wei May, 2020
% load projection data
load('./Aproj_C2H4') % contains data Aproj

% Inputs
nx = 100;
ny = 100;
nz = 36; % grid size
theta = [0:30:150]; % view angles for projection
p = 128; % number of pixels in the projection

% get 2D weight matrix from toolbox AIRTools
W_2D = paralleltomo(nx,theta,p);
% 3D weight matrix
Iz   = speye(nz);
W_3D   = kron(Iz,A_6P_2D);



% define a threshold to mask the projection images
threshold = 0.0002;

% mask indices
idx_mask = find(Aproj<=threshold);
```

```
27
28 % find ray traces (rows in W_3D) that contributes to masked
       projections
29 W_3D_nonvalid =  W_3D(idx_mask,:);
30 % if a pixel is not constributing to the nonvalid rays, keep the
       indices
31 sum(W_3D_nonvalid);
32 idx_K = find(ans==0);
33 % indices of projections above threshold
34 idx_A = find(Aproj>threshold);
35
36 % masked(truncated weight matrix)
37 W_3D_valid = W_3D(idx_A,idx_K);
```

C.4 Deep Neural Network Inversion Training

The Python code provided in this section is used to train the deep neural network presented in [62]

```
"""
Deep learning inversion for 3D CH4 Imaging
@author: Chuyu Wei
"""
from __future__ import absolute_import, division, print_function,
    unicode_literals

# TensorFlow and tf.keras
import tensorflow as tf

from keras import models
from keras import layers
from keras import regularizers
from keras.layers import Conv2D, Conv2DTranspose
from keras.optimizers import RMSprop
from random import randrange

# Helper libraries
import numpy as np
import matplotlib.pyplot as plt
import scipy.io
from scipy.io import loadmat

config = tf.ConfigProto()
config.gpu_options.allow_growth = True
```

```
25 sess = tf.Session(config=config)
26
27 # Load matlab files
28 # Training data
29 Training_file = 'TrainingDataAreas.mat';
30 Training_data = scipy.io.loadmat(Training_file);
31
32 # Build the model
33 # Setup the layers
34 model = models.Sequential()
35 model.add(layers.Flatten(input_shape=(6,N,1) ) )
36 model.add(layers.Dense(2*6*N))
37 model.add(layers.Activation('tanh'))
38 model.add(layers.Dense(1*6*N))
39 model.add(layers.Activation('tanh'))
40 model.add(layers.Dense(N*N))
41 model.add(layers.Activation('tanh'))
42 model.add(layers.Reshape((N,N,1) ) )
43 model.add(layers.Conv2D(filters=64, kernel_size=(5,5), strides
      =(1,1), activation = 'relu') )
44 model.add(layers.Conv2D(filters=64, kernel_size=(5,5), strides
      =(1,1), activation = 'relu') )
45 model.add(layers.Conv2DTranspose(filters=1, kernel_size=(9,9),
      strides=(1,1), activation='relu', kernel_regularizer=
      regularizers.l2(0.001)))
46
47
```

```
48 model.compile(loss='mean_squared_error', optimizer='adam', metrics
       =['mean_squared_error'])
49
50 model.summary()
51
52 # Train the model
53 history = model.fit(X_train_2D, Y_train_2D, validation_split=0.3,
       epochs=100, batch_size=50, shuffle= True)
54
55 # Plot training & validation loss values
56 plt.plot(history.history['loss'])
57 plt.plot(history.history['val_loss'])
58 plt.title('Model loss')
59 plt.ylabel('Loss')
60 plt.xlabel('Epoch')
61 plt.legend(['Train', 'Test'], loc='upper left')
62 plt.show()
```

Bibliography

[1] R. K. Hanson, M. R. Spearrin, and C. S. Goldenstein, *Spectroscopy and Optical Diagnostics for Gases*. 2016.

[2] C. S. Goldenstein, R. M. Spearrin, J. B. Jeffries, and R. K. Hanson, "Infrared laser-absorption sensing for combustion gases," *Progress in Energy and Combustion Science*, vol. 60, pp. 132–176, 5 2017.

[3] W. Cai and C. F. Kaminski, "Tomographic absorption spectroscopy for the study of gas dynamics and reactive flows," *Progress in Energy and Combustion Science*, vol. 59, pp. 1–31, 3 2017.

[4] C. K. Law, *Combustion Physics*. New York: Cambridge University Press, 2006.

[5] S. R. Turns, *An Introduction to Combustion: Concepts and Applications*. New York: McGraw-Hill, 3 ed., 2012.

[6] E. D. Gonzalez-Juez, A. R. Kerstein, R. Ranjan, and S. Menon, "Advances and challenges in modeling high-speed turbulent combustion in propulsion systems," *Progress in Energy and Combustion Science*, vol. 60, pp. 26–67, 2017.

[7] S. M. Correa, "Turbulence-chemistry interactions in the intermediate regime of premixed combustion," *Combustion and Flame*, vol. 93, no. 1-2, pp. 41–60, 1993.

[8] P. J. Coelho, "Numerical simulation of the interaction between turbulence and radiation in reactive flows," *Progress in Energy and Combustion Science*, vol. 33, no. 4, pp. 311–383, 2007.

[9] V. N. Nori and J. M. Scitzman, "CH* chemiluminescence modeling for combustion diagnostics," *Proceedings of the Combustion Institute*, vol. 32 I, no. 1, pp. 895–903, 2009.

[10] J. G. Lee, K. Kim, and D. A. Santavicca, "Measurement of equivalence ratio fluctuation and its effect on heat release during unstable combustion," *Proceedings of the Combustion Institute*, vol. 28, no. 1, pp. 415–421, 2000.

[11] Y. Hardalupas and M. Orain, "Local measurements of the time-dependent heat release rate and equivalence ratio using chemiluminescent emission from a flame," *Combustion and Flame*, vol. 139, no. 3, pp. 188–207, 2004.

[12] B. D. Stojkovic, T. D. Fansler, M. C. Drake, and V. Sick, "High-speed imaging of OH* and soot temperature and concentration in a stratified-charge direct-injection gasoline engine," *Proceedings of the Combustion Institute*, vol. 30 II, no. 2, pp. 2657–2665, 2005.

[13] X. Li and L. Ma, "Capabilities and limitations of 3D flame measurements based on computed tomography of chemiluminescence," *Combustion and Flame*, vol. 162, no. 3, pp. 642–651, 2015.

[14] J. Floyd, P. Geipel, and A. M. Kempf, "Computed Tomography of Chemiluminescence (CTC): Instantaneous 3D measurements and Phantom studies of a turbulent opposed jet flame," *Combustion and Flame*, vol. 158, no. 2, pp. 376–391, 2011.

[15] J. Floyd and A. M. Kempf, "Computed Tomography of Chemiluminescence (CTC): High resolution and instantaneous 3-D measurements of a Matrix burner," *Proceedings of the Combustion Institute*, vol. 33, no. 1, pp. 751–758, 2011.

[16] X. Li and L. Ma, "Volumetric imaging of turbulent reactive flows at kHz based on computed tomography," *Optics Express*, vol. 22, no. 4, p. 4768, 2014.

[17] J. Wang, Y. Song, Z.-h. Li, A. Kempf, and A.-z. He, "Multi-directional 3D flame chemiluminescence tomography based on lens imaging," *Optics Letters*, vol. 40, no. 7, p. 1231, 2015.

[18] K. Mohri, S. Görs, J. Schöler, A. Rittler, T. Dreier, C. Schulz, and A. Kempf, "Instantaneous 3D imaging of highly turbulent flames using computed tomography of chemiluminescence," *Applied Optics*, vol. 56, no. 26, p. 7385, 2017.

[19] Y. Jin, W. Zhang, Y. Song, X. Qu, Z. Li, Y. Ji, and A. He, "Three-dimensional rapid flame chemiluminescence tomography via deep learning," *Optics Express*, vol. 27, p. 27308, 9 2019.

[20] R. K. Hanson, J. M. Seitzman, and P. H. Paul, "Planar laser-fluorescence imaging of combustion gases," *Applied Physics B Photophysics and Laser Chemistry*, vol. 50, no. 6, pp. 441–454, 1990.

[21] G. Mathews and C. Goldenstein, "Wavelength-modulated planar laser-induced fluorescence for imaging gases," *Optics Letters*, vol. 42, no. 24, pp. 5278–5281, 2017.

[22] R. Wellander, M. Richter, and M. Aldén, "Time-resolved (kHz) 3D imaging of OH PLIF in a flame," *Experiments in Fluids*, vol. 55, no. 6, 2014.

[23] Y. Wu, W. Xu, Q. Lei, and L. Ma, "Single-shot volumetric laser induced fluorescence (VLIF) measurements in turbulent flows seeded with iodine," *Optics Express*, vol. 23, no. 26, p. 33408, 2015.

[24] F. Q. Zhao and H. Hiroyasu, "The applications of laser Rayleigh scattering to combustion diagnostics," *Progress in Energy and Combustion Science*, vol. 19, no. 6, pp. 447–485, 1993.

[25] A. Masri, R. Dibble, and R. Barlow, "The structure of turbulent nonpremixed flames revealed by Raman-Rayleigh-LIF measurements," *Progress in Energy and Combustion Science*, vol. 22, pp. 307–362, 1 1996.

[26] M. J. Dunn, A. R. Masri, and R. W. Bilger, "A new piloted premixed jet burner to study strong finite-rate chemistry effects," *Combustion and Flame*, vol. 151, no. 1-2, pp. 46–60, 2007.

[27] M. J. Dunn, A. R. Masri, R. W. Bilger, R. S. Barlow, and G. H. Wang, "The compositional structure of highly turbulent piloted premixed flames issuing into a hot coflow," *Proceedings of the Combustion Institute*, vol. 32, no. 2, pp. 1779–1786, 2009.

[28] F. Fuest, R. S. Barlow, G. Magnotti, and J. A. Sutton, "Scalar dissipation rates in a turbulent partially-premixed dimethyl ether/air jet flame," *Combustion and Flame*, vol. 188, pp. 41–65, 2018.

[29] T. A. McManus and J. A. Sutton, "Quantitative 2D Temperature Imaging in Turbulent Nonpremixed Jet Flames using Filtered Rayleigh Scattering," in *55th AIAA Aerospace Sciences Meeting*, no. January, (Reston, Virginia), pp. 1–12, American Institute of Aeronautics and Astronautics, 1 2017.

[30] I. Trueba Monje and J. A. Sutton, "Filtered Rayleigh Scattering Thermometry in Premixed Flames," in *2018 AIAA Aerospace Sciences Meeting*, (Reston, Virginia), American Institute of Aeronautics and Astronautics, 2018.

[31] F. Fuest, R. S. Barlow, J. Y. Chen, and A. Dreizler, "Raman/Rayleigh scattering and CO-LIF measurements in laminar and turbulent jet flames of dimethyl ether," *Combustion and Flame*, vol. 159, no. 8, pp. 2533–2562, 2012.

[32] C. Wei, D. I. Pineda, L. Paxton, F. N. Egolfopoulos, and R. M. Spearrin, "Mid-infrared laser absorption tomography for quantitative 2D thermochemistry measurements in premixed jet flames," *Applied Physics B*, vol. 124, p. 123, 6 2018.

[33] F. A. Bendana, J. J. Castillo, C. G. Hagström, and R. M. Spearrin, "Thermochemical structure of a hybrid rocket reaction layer based on laser absorption tomography," in *AIAA Propulsion and Energy 2019 Forum*, (Reston, Virginia), American Institute of Aeronautics and Astronautics, 8 2019.

[34] L. Ma, X. Li, S. T. Sanders, A. W. Caswell, S. Roy, D. H. Plemmons, and J. R. Gord, "50-kHz-rate 2D imaging of temperature and H2O concentration at the exhaust plane of a J85 engine using hyperspectral tomography," *Optics express*, vol. 21, pp. 1152–62, 1 2013.

[35] S. J. Grauer, J. Emmert, S. T. Sanders, S. Wagner, and K. J. Daun, "Multiparameter

gas sensing with linear hyperspectral absorption tomography," *Measurement Science and Technology*, vol. 30, p. 105401, 10 2019.

[36] E. O. Åkesson and K. J. Daun, "Parameter selection methods for axisymmetric flame tomography through Tikhonov regularizaron," *Applied Optics*, vol. 47, no. 3, pp. 407–416, 2008.

[37] C. J. Dasch, "One-dimensional tomography: a comparison of Abel, onion-peeling, and filtered backprojection methods," *Applied Optics*, vol. 31, p. 1146, 3 1992.

[38] K. J. Daun, K. A. Thomson, F. Liu, and G. J. Smallwood, "Deconvolution of axisymmetric flame properties using Tikhonov regularization," *Applied Optics*, vol. 45, p. 4638, 7 2006.

[39] C. Wei, D. I. Pineda, C. S. Goldenstein, and R. M. Spearrin, "Tomographic laser absorption imaging of combustion species and temperature in the mid-wave infrared," *Optics Express*, vol. 26, p. 20944, 8 2018.

[40] X. Liu, G. Zhang, Y. Huang, Y. Wang, and F. Qi, "Two-dimensional temperature and carbon dioxide concentration profiles in atmospheric laminar diffusion flames measured by mid-infrared direct absorption spectroscopy at 4.2 μm," *Applied Physics B*, vol. 124, p. 61, 4 2018.

[41] J. Emmert, M. Baroncelli, S. v. Kley, H. Pitsch, and S. Wagner, "Axisymmetric Linear Hyperspectral Absorption Spectroscopy and Residuum-Based Parameter & Selection on a Counter Flow Burner," *Energies*, vol. 12, p. 2786, 7 2019.

[42] R. J. Tancin, R. M. Spearrin, and C. S. Goldenstein, "2D mid-infrared laser-absorption imaging for tomographic reconstruction of temperature and carbon monoxide in laminar flames," *Optics Express*, vol. 27, p. 14184, 5 2019.

[43] K.-P. Cheong, L. Ma, Z. Wang, and W. Ren, "Influence of Line Pair Selection on Flame Tomography Using Infrared Absorption Spectroscopy," *Applied Spectroscopy*, vol. 73, pp. 529–539, 5 2019.

[44] A. Guha and I. M. Schoegl, "Tomographic Imaging of Flames: Assessment of Reconstruction Error Based on Simulated Results," *Journal of Propulsion and Power*, vol. 30, pp. 350–359, 3 2014.

[45] L. Nicolaides, A. Mandelis, and M. Munidasa, "Experimental and image-inversion optimization aspects of thermal-wave diffraction tomographic microscopy," no. May, pp. 8–10, 2009.

[46] Y. Wei, G. Wang, and J. Hsieh, "Relation between the filtered backprojection algorithm and the backprojection algorithm in CT," *IEEE Signal Processing Letters*, vol. 12, no. 9, pp. 633–636, 2005.

[47] K. M. Busa, E. Bryner, J. C. Mcdaniel, C. P. Goyne, C. T. Smith, and G. S. Diskin, "Demonstration of capability of water flux measurement in a scramjet combustor using tunable diode laser absorption tomography and stereoscopic PIV," *49th AIAA Aerospace Sciences Meeting Including the New Horizons Forum and Aerospace Exposition*, no. January, pp. 1–14, 2011.

[48] K. M. Busa, E. N. Ellison, B. J. McGovern, J. C. McDaniel, G. S. Diskin, M. J. DePiro, D. P. Capriotti, and R. L. Gaffney, "Measurements on NASA Langley durable combustor rig by TDLAT: Preliminary results," *51st AIAA Aerospace Sciences Meeting including the New Horizons Forum and Aerospace Exposition 2013*, no. January, pp. 1–13, 2013.

[49] E. Bryner, K. Busa, J. McDaniel, C. Goyne, and G. Diskin, "Spatially Resolved Temperature and Water Vapor Concentration Distributions in a Flat Flame Burner by Tunable Diode Laser Absorption Tomography," no. January, 2011.

[50] E. J. Mohamad, R. A. Rahim, S. Ibrahim, S. Sulaiman, and M. S. Manaf, "Flame imaging using laser-based transmission tomography," *Sensors and Actuators, A: Physical*, vol. 127, no. 2, pp. 332–339, 2006.

[51] R. T. Baum, K. B. McGrattan, and M. R. Nyden, "An Examination of the Applicability of Computed Tomography for the Measurement of Component Concentrations in Fire-Generated Plumes," *Combustion and Flame*, vol. 113, no. 3, pp. 358–372, 1998.

[52] T. Elfving, T. Nikazad, and P. C. Hansen, "Semi-convergence and relaxation parameters for a class of sirt algorithms," *Electronic Transactions on Numerical Analysis*, vol. 37, no. 274, pp. 321–336, 2010.

[53] B. Gillet, Y. Hardalupas, C. Kavounides, and A. M. Taylor, "Infrared absorption for measurement of hydrocarbon concentration in fuel/air mixtures (MAST-B-LIQUID)," *Applied Thermal Engineering*, vol. 24, no. 11-12, pp. 1633–1653, 2004.

[54] C. Wang, A. Mbi, and M. Shepherd, "A study on breath acetone in diabetic patients using a cavity ringdown breath analyzer: Exploring correlations of breath acetone with blood glucose and glycohemoglobin A1C," *IEEE Sensors Journal*, vol. 10, no. 1, pp. 54–63, 2010.

[55] F. Wang, Q. Wu, Q. Huang, H. Zhang, J. Yan, and K. Cen, "Simultaneous measurement of 2-dimensional H2O concentration and temperature distribution in premixed methane/air flame using TDLAS-based tomography technology," *Optics Communications*, vol. 346, pp. 53–63, 2015.

[56] D. W. Choi, M. G. Jeon, G. R. Cho, T. Kamimoto, Y. Deguchi, and D. H. Doh, "Performance improvements in temperature reconstructions of 2-D tunable diode laser absorption spectroscopy (TDLAS)," *Journal of Thermal Science*, vol. 25, no. 1, pp. 84–89, 2016.

[57] H. Xia, R. Kan, Z. Xu, Y. He, J. Liu, B. Chen, C. Yang, L. Yao, M. Wei, and G. Zhang, "Two-step tomographic reconstructions of temperature and species concentration in a flame based on laser absorption measurements with a rotation platform," *Optics and Lasers in Engineering*, vol. 90, no. June 2016, pp. 10–18, 2017.

[58] L. Z. Lifang Zhang, F. W. Fei Wang, H. Z. Haidan Zhang, J. Y. Jianhua Yan, , K. Cen, and K. Cen, "Simultaneous measurement of gas distribution in a premixed flame using adaptive algebraic reconstruction technique based on the absorption spectrum," *Chinese Optics Letters*, vol. 14, no. 11, pp. 111201–111205, 2016.

[59] K. Daun, "Infrared species limited data tomography through Tikhonov reconstruction," *Journal of Quantitative Spectroscopy and Radiative Transfer*, vol. 111, pp. 105–115, 1 2010.

[60] A. Guha and I. Schoegl, "Limited view tomography of combustion zones using tunable diode laser absorption spectroscopy - Simulation of an algebraic reconstruction technique," *ASME International Mechanical Engineering Congress and Exposition, Proceedings (IMECE)*, vol. 6, no. PARTS A AND B, pp. 305–315, 2012.

[61] K. J. Daun, S. J. Grauer, and P. J. Hadwin, "Chemical species tomography of turbulent flows: Discrete ill-posed and rank deficient problems and the use of prior information," *Journal of Quantitative Spectroscopy and Radiative Transfer*, vol. 172, pp. 58–74, 2016.

[62] C. Wei, K. Schwarm, D. Pineda, and M. Spearrin, "Deep neural network inversion for 3D laser absorption imaging of methane in reacting flows," *Optics Letters*, vol. 45, no. 8, pp. 2447–2450, 2020.

[63] S. J. Grauer, P. J. Hadwin, and K. J. Daun, "Bayesian approach to the design of chemical species tomography experiments," *Applied Optics*, vol. 55, no. 21, p. 5772, 2016.

[64] S. J. Grauer, "Bayesian Methods for Gas-Phase Tomography," 2018.

[65] W. Cai, D. J. Ewing, and L. Ma, "Application of simulated annealing for multispectral tomography," *Computer Physics Communications*, vol. 179, no. 4, pp. 250–255, 2008.

[66] W. Cai, K. Li, H. Liao, H. Wang, and L. Wu, "Weather conditions conducive to Beijing severe haze more frequent under climate change," *Nature Climate Change*, 3 2017.

[67] L. Ma, W. Cai, A. W. Caswell, T. Kraetschmer, S. T. Sanders, S. Roy, and J. R. Gord, "Tomographic imaging of temperature and chemical species based on hyperspectral absorption spectroscopy," *Optics Express*, vol. 17, p. 8602, 5 2009.

[68] J. Li, Y. Du, Z. Peng, and Y. Ding, "Measurements of spectroscopic parameters of CO2 transitions for Voigt, Rautian, galatry and speed-dependent voigt profiles near 1.43μm using the WM-DAS method," *Journal of Quantitative Spectroscopy and Radiative Transfer*, vol. 224, pp. 197–205, 2019.

[69] D. Hayashi, J. Nakai, M. Minami, T. Kamimoto, and Y. Deguchi, "Simultaneous measurement of CH4 concentration and temperature distributions in a semiconductor process chamber," *Journal of Physics D: Applied Physics*, vol. 52, p. 485107, 11 2019.

[70] L. H. Ma, L. Y. Lau, and W. Ren, "Non-uniform temperature and species concentration measurements in a laminar flame using multi-band infrared absorption spectroscopy," *Applied Physics B*, vol. 123, p. 83, 3 2017.

[71] G. Wang, J. C. Ye, K. Mueller, and J. A. Fessler, "Image Reconstruction is a New Frontier of Machine Learning," *IEEE Transactions on Medical Imaging*, vol. 37, no. 6, pp. 1289–1296, 2018.

[72] J. Huang, H. Liu, J. Dai, and W. Cai, "Reconstruction for limited-data nonlinear tomographic absorption spectroscopy via deep learning," *Journal of Quantitative Spectroscopy and Radiative Transfer*, vol. 218, pp. 187–193, 10 2018.

[73] T. Ren, M. F. Modest, A. Fateev, G. Sutton, W. Zhao, and F. Rusu, "Machine learning applied to retrieval of temperature and concentration distributions from infrared emission measurements," *Applied Energy*, vol. 252, p. 113448, 10 2019.

[74] J. Huang, H. Liu, and W. Cai, "Online in situ prediction of 3-D flame evolution from its history 2-D projections via deep learning," *Journal of Fluid Mechanics*, vol. 875, p. R2, 9 2019.

[75] R. Q. Yang, "Infrared laser based on intersubband transitions in quantum wells," 1995.

[76] M. Kim, C. L. Canedy, W. W. Bewley, C. S. Kim, J. R. Lindle, J. Abell, I. Vurgaftman, and J. R. Meyer, "Interband cascade laser emitting at λ=3.75 μm in continuous wave above room temperature," *Applied Physics Letters*, vol. 92, no. 19, pp. 10–13, 2008.

[77] S. B. Pope, "Small scales, many species and the manifold challenges of turbulent combustion," *Proceedings of the Combustion Institute*, vol. 34, no. 1, pp. 1–31, 2013.

[78] V. Bergmann, W. Meier, D. Wolff, and W. Stricker, "Application of spontaneous Raman and Rayleigh scattering and 2D LIF for the characterization of a turbulent CH4/H2/N2 jet diffusion flame," *Applied Physics B: Lasers and Optics*, vol. 66, pp. 489–502, 4 1998.

[79] W. Meier, R. S. Barlow, Y. L. Chen, and J. Y. Chen, "Raman/Rayleigh/LIF measurements in a turbulent CH4/H2/N2 jet diffusion flame: Experimental techniques and turbulence-chemistry interaction," *Combustion and Flame*, vol. 123, no. 3, pp. 326–343, 2000.

[80] R. Cabra, J. Chen, R. Dibble, A. Karpetis, and R. Barlow, "Lifted methane–air jet flames in a vitiated coflow," *Combustion and Flame*, vol. 143, pp. 491–506, 12 2005.

[81] D. Veynante and L. Vervisch, "Turbulent combustion modeling," *Progress in Energy and Combustion Science*, vol. 28, no. 3, pp. 193–266, 2002.

[82] D. Han, A. Satija, J. Kim, Y. Weng, J. P. Gore, and R. P. Lucht, "Dual-pump vibrational CARS measurements of temperature and species concentrations in turbulent premixed flames with CO2 addition," *Combustion and Flame*, vol. 181, pp. 239–250, 7 2017.

[83] R. S. Barlow, G. H. Wang, P. Anselmo-Filho, M. S. Sweeney, and S. Hochgreb, "Application of Raman/Rayleigh/LIF diagnostics in turbulent stratified flames," *Proceedings of the Combustion Institute*, vol. 32 I, no. 1, pp. 945–953, 2009.

[84] M. J. Dunn, A. R. Masri, R. W. Bilger, and R. S. Barlow, "Finite rate chemistry effects in highly sheared turbulent premixed flames," *Flow, Turbulence and Combustion*, vol. 85, no. 3-4, pp. 621–648, 2010.

[85] B. R. Halls, J. R. Gord, T. R. Meyer, D. J. Thul, M. Slipchenko, and S. Roy, "20-kHz-rate three-dimensional tomographic imaging of the concentration field in a turbulent jet," *Proceedings of the Combustion Institute*, vol. 36, no. 3, pp. 4611–4618, 2017.

[86] J. Smolke, S. Lapointe, L. Paxton, G. Blanquart, F. Carbone, A. M. Fincham, and F. N. Egolfopoulos, "Experimental and numerical studies of fuel and hydrodynamic effects on piloted turbulent premixed jet flames," *Proceedings of the Combustion Institute*, vol. 36, no. 2, pp. 1877–1884, 2017.

[87] F. Carbone, J. L. Smolke, A. M. Fincham, and F. N. Egolfopoulos, "Comparative behavior of piloted turbulent premixed jet flames of C1–C8 hydrocarbons," *Combustion and Flame*, vol. 180, pp. 88–101, 6 2017.

[88] L. Rothman, I. Gordon, R. Barber, H. Dothe, R. Gamache, A. Goldman, V. Perevalov, S. Tashkun, and J. Tennyson, "HITEMP, the high-temperature molecular spectroscopic database," *Journal of Quantitative Spectroscopy and Radiative Transfer*, vol. 111, pp. 2139–2150, 10 2010.

[89] J. J. Girard, R. M. Spearrin, C. S. Goldenstein, and R. K. Hanson, "Compact optical probe for flame temperature and carbon dioxide using interband cascade laser absorption near 4.2 µm," *Combustion and Flame*, vol. 178, pp. 158–167, 2017.

[90] M. Ravichandran and F. C. Gouldin, "Retrieval of asymmetric temperature and concentration profiles from a limited number of absorption measurements," *Combustion Science and Technology*, vol. 60, no. 1-3, pp. 231–248, 1988.

[91] R. Villarreal and P. L. Varghese, "Frequency-resolved absorption tomography with tunable diode lasers," *Applied Optics*, vol. 44, no. 31, pp. 6786–6795, 2005.

[92] J. Song, Y. Hong, G. Wang, and H. Pan, "Algebraic tomographic reconstruction of two-dimensional gas temperature based on tunable diode laser absorption spectroscopy," *Applied Physics B*, vol. 112, no. 4, pp. 529–537, 2013.

[93] P. Nau, J. Koppmann, A. Lackner, K. Kohse-Höinghaus, and A. Brockhinke, "Quantum cascade laser-based MIR spectrometer for the determination of CO and CO2 concentrations and temperature in flames," *Applied Physics B: Lasers and Optics*, vol. 118, no. 3, pp. 361–368, 2015.

[94] J. Foo and P. A. Martin, "Tomographic imaging of reacting flows in 3D by laser absorption spectroscopy," *Applied Physics B*, vol. 123, p. 160, 5 2017.

[95] D. D. Lee, F. A. Bendana, S. A. Schumaker, and R. M. Spearrin, "Wavelength modulation spectroscopy near 5 μm for carbon monoxide sensing in a high-pressure kerosene-fueled liquid rocket combustor," *Applied Physics B*, vol. 124, p. 77, 5 2018.

[96] A. Savitzky and M. J. E. Golay, "Smoothing and Differentiation of Data by Simplified Least Squares Procedures.," *Analytical Chemistry*, vol. 36, pp. 1627–1639, 7 1964.

[97] D. D. Cox and P. C. Hansen, "Rank-Deficient and Discrete III-Posed Problems: Numerical Aspects of Linear Inversion," *Journal of the American Statistical Association*, vol. 94, p. 1388, 12 1999.

[98] J. F. Driscoll, "Turbulent premixed combustion: Flamelet structure and its effect on turbulent burning velocities," *Progress in Energy and Combustion Science*, vol. 34, no. 1, pp. 91–134, 2008.

[99] A. N. Lipatnikov and J. Chomiak, "Effects of premixed flames on turbulence and turbulent scalar transport," *Progress in Energy and Combustion Science*, vol. 36, no. 1, pp. 1–102, 2010.

[100] S. G. Davis and C. K. Law, "Determination of and Fuel Structure Effects on Laminar Flame Speeds of C1 to C8 Hydrocarbons," *Combustion Science and Technology*, vol. 140, no. 1-6, pp. 427–449, 1998.

[101] Z. Zhao, L. I. Juan, A. Kazakov, F. L. Dryer, and S. P. Zeppieri, "Burning velocities and a high-temperature skeletal kinetic model for n-decane," *Combustion Science and Technology*, vol. 177, no. 1, pp. 89–106, 2005.

[102] K. Kumar and C. J. Sung, "Laminar flame speeds and extinction limits of preheated n-decane/O2/N2 and n-dodecane/O2/N2 mixtures," *Combustion and Flame*, vol. 151, no. 1-2, pp. 209–224, 2007.

[103] F. Dinkelacker, A. Soika, D. Most, D. Hofmann, A. Leipertz, W. Polifke, and K. Döbbeling, "Structure of locally quenched highly turbulent lean premixed flames," *Symposium (International) on Combustion*, vol. 27, no. 1, pp. 857–865, 1998.

[104] A. Y. Poludnenko and E. S. Oran, "The interaction of high-speed turbulence with flames: Global properties and internal flame structure," *Combustion and Flame*, vol. 157, no. 5, pp. 995–1011, 2010.

[105] C. Ji, E. Dames, B. Sirjean, H. Wang, and F. N. Egolfopoulos, "An experimental and modeling study of the propagation of cyclohexane and mono-alkylated cyclohexane flames," *Proceedings of the Combustion Institute*, vol. 33, no. 1, pp. 971–978, 2011.

[106] J. Smolke, F. Carbone, F. N. Egolfopoulos, and H. Wang, "Effect of n-dodecane decomposition on its fundamental flame properties," *Combustion and Flame*, vol. 190, pp. 65–73, 2018.

[107] A. T. Holley, X. Q. You, E. Dames, H. Wang, and F. N. Egolfopoulos, "Sensitivity of propagation and extinction of large hydrocarbon flames to fuel diffusion," *Proceedings of the Combustion Institute*, vol. 32 I, no. 1, pp. 1157–1163, 2009.

[108] A. N. Lipatnikov and J. Chomiak, "Molecular transport effects on turbulent flame propagation and structure," *Progress in Energy and Combustion Science*, vol. 31, no. 1, pp. 1–73, 2005.

[109] T. M. Wabel, A. W. Skiba, J. E. Temme, and J. F. Driscoll, "Measurements to determine the regimes of premixed flames in extreme turbulence," *Proceedings of the Combustion Institute*, vol. 36, no. 2, pp. 1809–1816, 2017.

[110] L. Paxton, A. Giusti, E. Mastorakos, and F. N. Egolfopoulos, "Assessment of experimental observables for local extinction through unsteady laminar flame calculations," *Combustion and Flame*, vol. 207, pp. 196–204, 2019.

[111] L. Paxton, J. Smolke, and F. N. Egolfopoulos, "Effects of heat release and fuel type on highly turbulent premixed jet flames," *Proceedings of the Combustion Institute*, vol. 37, no. 2, pp. 2565–2572, 2019.

[112] T. A. McManus, I. T. Monje, and J. A. Sutton, "Experimental assessment of the Tenti S6 model for combustion-relevant gases and filtered Rayleigh scattering applications," *Applied Physics B: Lasers and Optics*, vol. 125, no. 1, pp. 1–23, 2019.

[113] R. Cabra, J. Chen, R. Dibble, A. Karpetis, and R. Barlow, "Lifted methane–air jet flames in a vitiated coflow," *Combustion and Flame*, vol. 143, pp. 491–506, 12 2005.

[114] R. S. Barlow, J. H. Frank, A. N. Karpetis, and J. Y. Chen, "Piloted methane/air jet flames: Transport effects and aspects of scalar structure," *Combustion and Flame*, vol. 143, no. 4, pp. 433–449, 2005.

[115] Y. Chen and M. Ihme, "Large-eddy simulation of a piloted premixed jet burner," *Combustion and Flame*, vol. 160, no. 12, pp. 2896–2910, 2013.

[116] F. Grøvdal, S. Sannan, J. Y. Chen, A. R. Kerstein, and T. Løvås, "Three-dimensional Linear Eddy Modeling of a Turbulent Lifted Hydrogen Jet Flame in a Vitiated Coflow," *Flow, Turbulence and Combustion*, vol. 101, no. 4, pp. 993–1007, 2018.

[117] R. J. Kee, J. Miller, M. D. Smooke, and J. F. Grcar, "PREMIX: a Fortran program for modeling steady laminar one-dimensional premixed flames," Tech. Rep. SAND85-8240, Sandia National Laboratories, Livermore, CA, USA, 1985.

[118] D. I. Pineda, J. L. Urban, and R. Mitchell Spearrin, "Interband cascade laser absorption of hydrogen chloride for high-temperature thermochemical analysis of fire-resistant polymer reactivity," *Applied Optics*, vol. 59, p. 2141, 3 2020.

[119] S. Gazzola, P. C. Hansen, and J. G. Nagy, "IR Tools: a MATLAB package of iterative regularization methods and large-scale test problems," *Numerical Algorithms*, vol. 81, no. 3, pp. 773–811, 2019.

[120] O. Colin, F. Ducros, D. Veynante, and T. Poinsot, "A thickened flame model for large eddy simulations of turbulent premixed combustion," *Physics of Fluids*, vol. 12, no. 7, pp. 1843–1863, 2000.

[121] A. W. Vreman, "An eddy-viscosity subgrid-scale model for turbulent shear flow: Algebraic theory and applications," *Physics of Fluids*, vol. 16, no. 10, pp. 3670–3681, 2004.

[122] Y. Khalighi, J. W. Nichols, S. K. Lele, F. Ham, and P. Moin, "Unstructured large eddy simulation for prediction of noise issued from turbulent jets in various configurations," *17th AIAA/CEAS Aeroacoustics Conference 2011 (32nd AIAA Aeroacoustics Conference)*, no. June, pp. 5–8, 2011.

[123] P. C. Ma, Y. Lv, and M. Ihme, "An entropy-stable hybrid scheme for simulations of transcritical real-fluid flows," *Journal of Computational Physics*, vol. 340, pp. 330–357, 2017.

[124] Gilbert, "On the Construction and Comparison of Difference Schemes Author (s): Gilbert Strang Source : SIAM Journal on Numerical Analysis , Vol . 5 , No . 3 (Sep ., 1968), pp . 506-517 Published by : Society for Industrial and Applied Mathematics Stable URL : h," *Society*, vol. 5, no. 3, pp. 506–517, 2013.

[125] S. Gottlieb, C. Shu, and E. Tadmor, "High order time discretization methods with the strong stability property," vol. 43, no. 1, pp. 89–112, 2001.

[126] H. Wu, P. C. Ma, and M. Ihme, "Efficient time-stepping techniques for simulating turbulent reactive flows with stiff chemistry," *Computer Physics Communications*, vol. 243, pp. 81–96, 10 2019.

[127] T. Lu and C. K. Law, "A directed relation graph method for mechanism reduction," *Proceedings of the Combustion Institute*, vol. 30, no. 1, pp. 1333–1341, 2005.

[128] D. G. Goodwin, H. K. Moffat, and R. L. Speth, "Cantera: An object-oriented software toolkit for chemical kinetics, thermodynamics, and transport processes," 2018.

[129] H. Wang, X. You, A. V. Joshi, S. G. Davis, and others, "USC Mech Version II. High-Temperature Combustion Reaction Model of H2/CO/C1-C4 Compounds," 2007.

[130] H. Wang, E. Dames, B. Sirjean, D. A. Sheen, R. Tango, A. Violi, J. Y. W. Lai, F. N. Egolfopoulos, D. F. Davidson, R. K. Hanson, C. T. Bowman, C. K. Law, W. Tsang, N. P. Cernansky, D. L. Miller, and R. P. Lindstedt, "A high-temperature chemical kinetic model of n-alkane (up to n-dodecane), cyclohexane, and methyl-, ethyl-, n-propyl and n-butyl-cyclohexane oxidation at high temperatures, JetSurF version 2.0," 2010.

[131] M. F. Campbell, S. Wang, C. S. Goldenstein, R. M. Spearrin, A. M. Tulgestke, L. T. Zaczek, D. F. Davidson, and R. K. Hanson, "Constrained reaction volume shock tube study of n -heptane oxidation: Ignition delay times and time-histories of multiple species and temperature," *Proceedings of the Combustion Institute*, vol. 35, no. 1, pp. 231–239, 2015.

[132] F. Wang, K. F. Cen, N. Li, J. B. Jeffries, Q. X. Huang, J. H. Yan, and Y. Chi, "Two-dimensional tomography for gas concentration and temperature distributions based on tunable diode laser absorption spectroscopy," *Measurement Science and Technology*, vol. 21, no. 4, 2010.

[133] C. Liu, L. Xu, J. Chen, Z. Cao, Y. Lin, and W. Cai, "Development of a fan-beam

TDLAS-based tomographic sensor for rapid imaging of temperature and gas concentration," *Optics Express*, vol. 23, no. 17, p. 22494, 2015.

[134] R. M. Spearrin, C. S. Goldenstein, I. A. Schultz, J. B. Jeffries, and R. K. Hanson, "Simultaneous sensing of temperature, CO, and CO2 in a scramjet combustor using quantum cascade laser absorption spectroscopy," *Applied Physics B*, vol. 117, pp. 689–698, 11 2014.

[135] J. J. Harrison, N. D. C. Allen, and P. F. Bernath, "Infrared absorption cross sections for ethane (C2H6) in the 3μm region," *Journal of Quantitative Spectroscopy and Radiative Transfer*, vol. 111, pp. 357–363, 2 2010.

[136] S. A. Tsekenis, N. Tait, and H. McCann, "Spatially resolved and observer-free experimental quantification of spatial resolution in tomographic images," *Review of Scientific Instruments*, vol. 86, no. 3, 2015.

[137] K. K. Schwarm, C. Wei, D. I. Pineda, and R. Mitchell Spearrin, "Time-resolved laser absorption imaging of ethane at 2 kHz in unsteady partially premixed flames," *Applied Optics*, vol. 58, p. 5656, 7 2019.

[138] M. P. Wood and K. B. Ozanyan, "Simultaneous temperature, concentration, and pressure imaging of water vapor in a turbine engine," *IEEE Sensors Journal*, vol. 15, no. 1, pp. 545–551, 2015.

[139] L. Ma and W. Cai, "Numerical investigation of hyperspectral tomography for simultaneous temperature and concentration imaging," *Applied Optics*, vol. 47, no. 21, p. 3751, 2008.

[140] K. Wang, R. Milcarek, P. Zeng, and J. Ahn, "Flame-assisted fuel cells running methane," *International Journal of Hydrogen Energy*, vol. 40, no. 13, pp. 4659–4665, 2015.

[141] F. Nicolas, V. Todoroff, A. Plyer, G. Le Besnerais, D. Donjat, F. Micheli, F. Champagnat, P. Cornic, and Y. Le Sant, "A direct approach for instantaneous 3D density

field reconstruction from background-oriented schlieren (BOS) measurements," *Experiments in Fluids*, vol. 57, no. 1, pp. 1–21, 2016.

[142] R. J. Hargreaves, I. E. Gordon, M. Rey, A. V. Nikitin, V. G. Tyuterev, R. V. Kochanov, and L. S. Rothman, "An Accurate, Extensive, and Practical Line List of Methane for the HITEMP Database," *The Astrophysical Journal Supplement Series*, vol. 247, no. 2, p. 55, 2020.

[143] B. Zhu, J. Z. Liu, S. F. Cauley, B. R. Rosen, and M. S. Rosen, "Image reconstruction by domain-transform manifold learning," *Nature*, vol. 555, no. 7697, pp. 487–492, 2018.

[144] H. W. Coleman and W. G. Steele, *Experimentation, Validation, and Uncertainty Analysis for Engineers*. Hoboken, NJ, USA: John Wiley & Sons, Inc., 3rd ed., 2009.